UNIVERSITÀ
DEGLI STUDI
FIRENZE

DOTTORATO DI RICERCA IN
International doctorate in atomic and molecular photonics

CICLO XXX

COORDINATORE Prof. Righini Roberto

Light transport in exotic complex media: from fractal resonances to ultrawhite anisotropic random network

Settore Scientifico Disciplinare FIS/03

Dottorando
Dott. Utel Francesco

Tutore
Prof. Wiersma Diederik Sybolt

Coordinatore
Prof. Righini Roberto

Anni 2014/2017

To my family

"If something is nothing it must not be something in any possible way"

— John Frusciante, *Central*

Preface

Modeling disorder is a fundamental aspect in the study of the physical optical properties of the object around us. In fact, many of the materials found in nature present from the microscopic point of view, a lack of order in the constitutive elements arrangement, feature that needs to be taken into account in the study of any kind of structural related phenomena. This is particularly true in optics, where a deep understanding on how visible radiation interacts with inhomogeneities on this length scale is fundamental to get insight in the light propagation mechanisms. In the case of ordered structures, like gratings or photonic crystals, to cite a few, coherence phenomena are dominant and interference carries to the formation of a band gap that inhibits the light propagation for specific frequencies. On the other hand, disordered systems lead in general to the opposite effect, where a sequence of scattering events from randomly distributed scattering centers causes frequency independent transport. However, optical media can not be classified only in these two categories. Disorder can occur in many different fashions, depending from both the scattering center arrangements and the shape and size of the scattering object, that influence light transports differently. For example, disorder with structural correlations generates constructive interference for specific frequencies, increasing the corresponding transport mean free path. Moreover different ratios between wavelength and particles size corresponds to different transport regimes. When particles are much smaller than the wavelength the scattering is merely isotropic, while when they are comparable, i.e. the Mie regime, the scattering cross-section increases and the single particle resonances lead as well to a non uniform spectral response.
In this work we focused on two disordered systems that, due to the exotic structural properties of the underlying geometries, exhibit unique optical properties. The first one is an ideal 2D fractal disordered system with strongly resonant scatterers, while the second one is a biological anisotropic network embedded inside the scale of a white beetle. These very different systems are also studied with two very different approaches. In the case of the fractals, a modal analysis have been performed, computing the solution of Maxwell equations in the single scattering approximation and obtaining the spatial and spectral distributions of electric field modes supported by the systems. A statistical study of the mode size has demonstrated how, on the contrary of homogeneous disordered systems and heterogeneous disordered system with lack of self-similarity, fractals exhibit coexistence of modes of every size. In the second part we investigated the striking

optical properties of the white beetle *Chyphochilus*. The back of this animal is covered by scales hosting a dense, random anisotropic network made of chitin. Despite the low refractive index and the low thickness of the system, the network displays incredibly high brightness and whiteness, feature denoting a high scattering strength reached thorough a smart arrangement of the scattering centers. In this work we investigated the structural feature behind this optical behaviour, unveiling through experimental measurements and numerical modeling the strategy behind the brightness and whiteness optimization: the anisotropic arrangement of the chitin filaments.
In **Chapter 1** the theoretical methods exploited in this work are presented, describing the formalism to tackle light transport problems both in terms of wave transport and in terms of incoherent intensity propagation. In the first part, starting from Maxwell equations, we derive an expression of the electric field resonances for an ensemble of coupled electric dipoles. In the second part, starting again from Maxwell equations, we show the procedure to retrieve the Radiative transfer equation (RTE) and the diffusion approximation (DE).
In **Chapter 2** the analysis on 2D fractal ensemble of strong resonant scattering centers is performed. A brief overview on the geometrical properties of fractal is presented and the impact of self-similarity on the optical properties of other fractal systems previously studied is shortly discussed. Then the resonances of the fractal system are computed, studying the size statistics both in term of number of scattering particles involved and in terms of effective size. We show how scale-invariant systems display coexistence of a wide range of mode size not found in other disorder configurations.
In **Chapter 3** an introduction on structural coloration in nature is presented, reviewing biological photonic structures exploited by animals to reach specific color selection. After an introduction on the white color, the optical properties of the *Chyphochilus* and another white beetle, the *Leipidiota Stigma*, are described, reporting previous light transport measurements proving that multiple scattering of light occurs inside the scales.
In **Chapter 4** the experimental study on the morphology of the chitin random network inside the *Chyphochilus* scale is performed. Evidences of anisotropic light transport are reported and a claim of optimization of brightness through anisotropy is formulated.
In **Chapter 5** we perform a modeling of the chitin random network, designing a simple algorithm to generate numerically random network of rods with tunable structural parameters. Performing FDTD simulations on systems with the same amount of material but different degree of anisotropy, we show how the rod orientation plays indeed a role in the scattering strength optimization of a beetle-like network system, confirming the hypothesis of Chapter 4.

Contents

CHAPTER 1

The study of light transport in random media: mode analysis and diffusive transport

The theoretical models suitable to describe light transport in complex random media are, like every model that describes classical light and matter interaction, based on Maxwell equation, that, depending by the investigated phenomena, become solvable through one or more approximations. Despite the same root, the theories developed and the approximation involved could lead to tackle the problem of light propagation with very different approaches. In this chapter a description of the theoretical formalism exploited in the thesis to perform a study on the scattering properties of the two types of complex systems investigated will be presented. Both systems considered belong to the vast class of disordered optical media, commonly characterized by multiple light scattering transport. The first type, studied in Chapter 2, are 2D fractal distributions, will be investigated through a coupled-dipole formalism where the electric field resonances of the systems are computed from Maxwell equations. Capturing thus the intrinsic wave nature of the transport, phase and coherent properties of light are taken into account studying the electromagnetic modes of the system. The second type of disordered media, presented in Chapter 4.3.1, is an anisotropic random network with unique optical properties. In this case it will be studied in the radiative transfer frame, i.e. neglecting the phase of the propagating light and describing the transport only in terms of intensity propagation. Before the description of the radiative transfer theory, the derivation of the radiative transfer equation from Maxwell equation is presented.

1.1 Coupled dipole formalism and mode analysis

In classical electrodynamics, the electromagnetic field generated by the presence of static electric charges is represented by the electric field vector **E** and the magnetic inductance **B**, that together with the electric displacement **D** and the magnetic field **H**

allows through Maxwell equations a description of steady-state and temporal dependent phenomena in both vacuum and dielectric or metallic objects. In the macroscopic picture, in order to describe the total field in the presence of a dielectric medium, it is necessary to consider how the charges bounded to their atoms and molecules, respond to the applied external field. The dipole moments allign inducing an electrical polarization $\mathbf{P}$ (dipole moment per unit volume) in the medium, related to the electric displacement by the relation $\mathbf{D} = \mathbf{E} + 4\pi\mathbf{P}$. Taking into account also molecules and atoms magnetic moments induced by the motion of the bounded charges, we can also define the magnetization $\mathbf{M}$ (magnetic moment per unit volume) related to the magnetic inductance by $\mathbf{B} = \mathbf{H} + 4\pi\mathbf{M}$. Inserting the above relations in Maxwell equations for a non conductive medium with no free currents or free charge densities we get

$$\boldsymbol{\nabla} \cdot \mathbf{E} = 4\pi\widetilde{\rho} \tag{1.1}$$

$$\boldsymbol{\nabla} \cdot \mathbf{B} = 0 \tag{1.2}$$

$$\boldsymbol{\nabla} \times \mathbf{E} = -\frac{1}{c}\frac{\partial \mathbf{B}}{\partial t} \tag{1.3}$$

$$\boldsymbol{\nabla} \times \mathbf{B} = \frac{1}{c}\frac{\partial \mathbf{E}}{\partial t} + \frac{4\pi}{c}\widetilde{\mathbf{j}} \tag{1.4}$$

with

$$\widetilde{\mathbf{j}} = \frac{\partial \mathbf{P}}{\partial t} + c(\boldsymbol{\nabla} \times \mathbf{M}) \quad \text{and} \quad \widetilde{\rho} = -\boldsymbol{\nabla} \cdot \mathbf{P} \tag{1.5}$$

defined respectively as the bounded current density and the bounded charge density [1]. This substitution has the scope to include in Maxwell equations the medium properties keeping them formally identical to the Maxwell equation in the vacuum ($\mathbf{D} = \mathbf{E}$ and $\mathbf{B} = \mathbf{H}$) with $\widetilde{\rho}$ and $\widetilde{\mathbf{j}}$ substituting the distributions of charge ρ and current j. The mode analysis of disorder systems carried on in this work is based on the analysis of the collective excitations of ensembles of scattering centers modeled as dipoles with the same polarizability. The coupled-dipole approximation (CDA), known also as discrete-dipole approximation (DDA) is a method largely used to describe the scattering properties of particles of arbitrary shape. Since macroscopic properties of a dielectric object are affected by the coupling of molecules and atoms to the incident electric field, the continuum medium can be approximated to an array of dipoles with a defined spatial distribution and polarizability determined by the bulk refractive index of the medium [2, 3, 4, 5, 6]. A distribution of N scattering centers can thus be modeled as a distribution of N periodic array of linear electric dipoles. Adding to an external field the mutual interaction between the dipoles, the resonance field amplitudes can be obtained solving a set of linear equations. A further approximation consists in neglecting the physical size of each scattering center, replacing it by a single point-like particle. This method known as point-scatterers approximation has been already proved to be a useful tool for the study of classical wave propagation in multiple scattering media, simplifying multiple scattering calculations still allowing the description of the related phenomena [7, 8, 9]. In the following part the field in an ensemble of N dipoles is retrieved from Maxwell equations. For the Maxwell equations (1.1)-(1.4) is possible, exactly as in the vacuum case, to introduce a vector potential $\mathbf{A}$ and a scalar potential ϕ, obtaining a

smaller number of second-order equation that identically satisfies the Maxwell equations. As the curl of a divergence is zero, (1.2) is satisfied by the condition

$$\mathbf{B} = \boldsymbol{\nabla} \times \mathbf{A} \tag{1.6}$$

that inserted in equation (1.3) leads to the relation of $\mathbf{E}$ in terms of $\mathbf{A}$ and an arbitrary vector potential ϕ

$$\mathbf{E} = -\frac{1}{c}\frac{\partial \mathbf{A}}{\partial t} - \boldsymbol{\nabla}(\phi). \tag{1.7}$$

Substituting (1.6) and (1.7) in (1.4) and (1.1) and using the identities $\boldsymbol{\nabla} \times \boldsymbol{\nabla} \times \mathbf{a} = \boldsymbol{\nabla} \cdot (\boldsymbol{\nabla} \cdot \mathbf{a}) - \nabla^2 \mathbf{a}$ and $\boldsymbol{\nabla} \cdot \boldsymbol{\nabla} \mathbf{a} = \nabla^2 \mathbf{a}$ we obtain

$$\nabla^2 \mathbf{A} - \frac{1}{c}\frac{\partial^2 \mathbf{A}}{\partial t^2} - \boldsymbol{\nabla}\left(\boldsymbol{\nabla} \cdot \mathbf{A} + \frac{1}{c}\frac{\partial \phi}{\partial t}\right) = -\frac{4\pi}{\widetilde{\mathbf{j}}} \tag{1.8}$$

$$\nabla^2 \phi - \frac{1}{c}\frac{\partial^2 \phi}{\partial t^2} - \frac{1}{c}\frac{\partial}{\partial t}(\boldsymbol{\nabla} \cdot \mathbf{A} + \frac{1}{c}\frac{\partial \phi}{\partial t}) = -4\pi\phi. \tag{1.9}$$

The following relation between $\mathbf{A}$ and ϕ,

$$\boldsymbol{\nabla} \cdot \mathbf{A} - \frac{1}{c}\phi = 0 \tag{1.10}$$

known as *Lorentz condition*, allows to simplify (1.8) and (1.9) to the couple of inhomogeneous wave equations

$$\nabla^2 \mathbf{A} - \frac{1}{c}\frac{\partial^2 \mathbf{A}}{\partial t^2} = -\frac{4\pi}{\widetilde{\mathbf{j}}} \tag{1.11}$$

$$\nabla^2 \phi - \frac{1}{c}\frac{\partial^2 \phi}{\partial t^2} = -4\pi\phi. \tag{1.12}$$

which solutions can be used in (1.6) and (1.7) to retrieve $\mathbf{E}$ and $\mathbf{B}$. One possible way to write a function for $\mathbf{A}$ and ϕ that satisfies these wave equations is to formulate these quantities in terms of *retarded potentials* [10]

$$\mathbf{A}(\mathbf{r}, t) = \frac{1}{c}\int_V \frac{\widetilde{\mathbf{j}}(\mathbf{r}', t - R/c)}{R}\,\mathrm{d}V' \quad \text{and} \quad \phi(\mathbf{r}, t) = \int_V \frac{\widetilde{\rho}(\mathbf{r}', t - R/c)}{R}\,\mathrm{d}V' \tag{1.13}$$

where $R = |\mathbf{r} - \mathbf{r}'|$ is the distance between $\mathbf{r}$ and the volume element at the point $\mathbf{r}'$. The origin of the name *retarded potentials* is due to the particular time dependence of the contribute of $\mathbf{A}$ and ϕ from each single volume element that take into account the time R/c needed for light to travel from $\mathbf{r}$ to $\mathbf{r}'$. Again, these expressions are analogous to those one would performing the same calculations from Maxwell equation in vacuum instead of (1.1)-(1.4). This fact allows to exploit (1.5) to write the retarded potentials (1.13) as a function of the electrical polarization and the magnetization:

$$\phi(\mathbf{r}, t) = \int_V \frac{\nabla' \cdot \mathbf{P}(\mathbf{r}', t - R/c)}{R}\,\mathrm{d}V' \tag{1.14}$$

$$\mathbf{A}(\mathbf{r},t) = \int_V \frac{1}{R}(\nabla' \times \mathbf{M}(\mathbf{r}', t - R/c) + \frac{1}{c}\frac{\partial r}{\partial t}\mathbf{P}(\mathbf{r}', t - R/c))\,\mathrm{d}V'\,. \tag{1.15}$$

Another method to represent the electromagnetic field in a medium consist in defining the Hertz vectors $\mathbf{\Pi_e}$ and $\mathbf{\Pi_m}$, formulated in terms of the potentials $\mathbf{A}$ and ϕ as

$$\phi = -\boldsymbol{\nabla} \cdot \mathbf{\Pi_e} \tag{1.16}$$

$$\mathbf{A} = \frac{1}{c}\frac{\partial \mathbf{\Pi_e}}{\partial t} + \boldsymbol{\nabla} \times \mathbf{\Pi_m}. \tag{1.17}$$

These expressions relate the Hertz vector to $\mathbf{P}$ and $\mathbf{M}$ by simpler expressions than (1.15) and (1.14) for $\mathbf{A}$ and ϕ. The analogy between equations (1.16)-(1.17) and (1.5), ensures the validity of (1.10), allowing to write the analogous of (1.12) and (1.11) for the Hertz potential

$$\nabla^2 \mathbf{\Pi_e} - \frac{1}{c}\frac{\partial^2 \mathbf{\Pi_e}}{\partial t^2} = -4\pi \mathbf{P} \tag{1.18}$$

$$\nabla^2 \mathbf{\Pi_m} - \frac{1}{c}\frac{\partial^2 \mathbf{\Pi_m}}{\partial t^2} = -4\pi \mathbf{M}. \tag{1.19}$$

with solutions expressed in terms of retarded potentials:

$$\mathbf{\Pi_e} = \int \frac{\mathbf{P}(\mathbf{r}', t - R/c)}{R}\,\mathrm{d}V' \quad \text{and} \quad \mathbf{\Pi_m} = \int \frac{\mathbf{M}(\mathbf{r}', t - R/c)}{R}\,\mathrm{d}V'\,. \tag{1.20}$$

Now that the expressions relating the Hertz vectors and the electric polarization and magnetization has been introduced, their relations with the fields $\mathbf{E}$ and $\mathbf{B}$ can be written explicitly. Substituting $\mathbf{A}$ as defined in (1.6) with (1.17) gives an expression for $\mathbf{B}$, while combining (1.6) and (1.7) with (1.16) provides an equation for $\mathbf{E}$[1]:

$$\mathbf{B} = \boldsymbol{\nabla} \times \left(\frac{1}{c}\frac{\partial \mathbf{\Pi_e}}{\partial t} + \boldsymbol{\nabla} \times \mathbf{\Pi_m}\right) \tag{1.21}$$

$$\mathbf{E} = \boldsymbol{\nabla} \times \left(-\frac{1}{c}\frac{\partial \mathbf{\Pi_m}}{\partial t} + \boldsymbol{\nabla} \times \mathbf{\Pi_e}\right) + (\nabla^2 \mathbf{\Pi_e} - \frac{1}{c^2}\frac{\partial^2 \mathbf{\Pi_e}}{\partial t^2}) \tag{1.22}$$

1.1.1 The field of a linear dipole ensamble

From Maxwell equation (1.1)-(1.4) for a non conductive medium, homogeneous and isotropic, with no current or density charges, an expression for the Hertz vectors and their relations with $\mathbf{E}$ and $\mathbf{B}$ have been retrieved. These relations will now be applied to the case of an electric linear dipole positioned at $\mathbf{r_0}$ oscillating along a direction defined by the unit vector $\mathbf{n}$. The electric polarization can be written as [1]

$$\mathbf{P}(\mathbf{r}, t) = p(t)\delta(\mathbf{r} - \mathbf{r_0})\hat{\mathbf{n}} \tag{1.23}$$

[1] The identity $\boldsymbol{\nabla}\boldsymbol{\nabla} \cdot a = \boldsymbol{\nabla} \times \boldsymbol{\nabla} \times \mathbf{a} + \nabla^2 a$ has been used

that according to (1.20) gives the associated vector potential

$$\mathbf{\Pi_e} = \frac{p(\mathbf{r_0}, t - R/c)}{R}\hat{\mathbf{n}}. \tag{1.24}$$

As (1.24) is a solution of the homogeneous wave equation for vacuum and $\mathbf{\Pi_m} = 0$, the electric field generated by the dipole expressed through (1.22) takes the form

$$\mathbf{E} = \boldsymbol{\nabla} \times \boldsymbol{\nabla} \times \mathbf{\Pi_e}, \tag{1.25}$$

that according to the first equation of (1.20) can be written as

$$\mathbf{E} = \boldsymbol{\nabla} \times \boldsymbol{\nabla} \times \int \frac{\mathbf{P}(\mathbf{r}', t - R/c)}{R}\, \mathrm{d}\mathbf{r}' \tag{1.26}$$

1.1.2 Scattering by N-dipole system: eigenvalues problem

In this section a derivation of the modes supported by an open system of electric dipoles is presented following the procedure in [11]. Let us consider a monochromatic field incident on N dipoles distributed in the x-y plane of the form $\mathbf{E}_0(\mathbf{r}, t) = E_0(x, y)e^{-i\omega t}\hat{e}_z$, polarized along z, the direction perpendicular to the dipoles plane. As a consequence, the polarizability of the medium takes the form $\mathbf{P}(\mathbf{r}, t) = P(x, y)e^{-i\omega t}\hat{e}_z$. This particular choice of the polarization direction permits to perform the calculation in the scalar approximation. As the system is a collection of point-like dipoles the polarizability of the whole medium is

$$P(x, y) = \sum_{a=1}^{N} p_a \delta_2(x - x_a, y - y_a), \tag{1.27}$$

where p_i and $(x_a,\, y_a)$ represent respectively the polarizability and the position of the a-th dipole. The electric field of the polarized medium can be expressed as the sum of the free field solution of Maxwell equation in vacuum with wavenumber $k_0 = \omega_0/c$, and the field radiated by the medium. Exploiting the Maxwell equation in integral form (1.26), it can be written as

$$\mathbf{E}(\mathbf{r}, t) = \mathbf{E}_0(\mathbf{r})e^{-i\omega_0 t} + \boldsymbol{\nabla} \times \boldsymbol{\nabla} \times \int d\mathbf{r}'\mathbf{P}(\mathbf{r}')\frac{e^{-i\omega_0 t}e^{i\frac{\omega_0|\mathbf{r}-\mathbf{r}'|}{c}}}{|\mathbf{r} - \mathbf{r}'|}, \tag{1.28}$$

obtaining the steady-state equation

$$\mathbf{E}(\mathbf{r}) = \mathbf{E}_0(\mathbf{r}) + \boldsymbol{\nabla} \times \boldsymbol{\nabla} \times \int d\mathbf{r}'\mathbf{P}(\mathbf{r}')\frac{e^{ik_0|\mathbf{r}-\mathbf{r}'|}}{|\mathbf{r} - \mathbf{r}'|}. \tag{1.29}$$

As both the incident field and the medium are polarized along the z direction, the second term of the equation (1.29), the electric field radiated from the a-th dipole, considering the expressions (1.27) becomes

$$\mathbf{E}(\boldsymbol{\rho}) = \hat{e}_z k_0^2 p_a g_{(2)}(\boldsymbol{\rho} - \boldsymbol{\rho}_a) \tag{1.30}$$

where for the sake of clarity the coordinates in the dipoles plane have been written as $\boldsymbol{\rho}$=(x_a, y_a). The term $g_{(2)}$ in the equation represents the 2D Green function

$$g_{(2)}(\boldsymbol{\rho}-\boldsymbol{\rho}_a)=\int_{-\infty}^{\infty}dz\ \frac{e^{ik_0|\mathbf{r}-\mathbf{r}_a|}}{|\mathbf{r}-\mathbf{r}_a|}=2K_0(-ik_0|\boldsymbol{\rho}-\boldsymbol{\rho}_a|)=i\pi H_0^{(1)}(k_0|\boldsymbol{\rho}-\boldsymbol{\rho}_a|)\ \ (1.31)$$

that can be written in terms of the modified Bessel function of the second kind K_0 or the Hankle function of the first kind H_0.[2] In order to perform reliable mode analysis in the frame of the point-like approximation, it is necessarily to provide a proper expression of the coupling between each single dipole and the electric field, that means to choose the proper scattering cross section. A realistic and self-consistent description is possible assuming that the average energy is conserved in the scattering process [12, 13]. Therefore, if we isolate a single dipole, then the time-averaged field energy flux integrated over a closed surface Σ surrounding it should vanish for an arbitrary incident wave, namely,

$$\int_{\Sigma}d\mathbf{s}\ \mathbf{S}(\mathbf{r})=\frac{c}{4\pi}\frac{1}{2}Re\int_{\Sigma}d\mathbf{s}\{\mathbf{E}(\mathbf{r})\times\mathbf{H}^*(\mathbf{r})\}. \tag{1.32}$$

with $\mathbf{s}$ unit vector normal to the surface. Integrating this equation (1.32), after calculations [11], one get the following coupling expression

$$\pi k_0^2|\mathbf{p}_a|=Im\{\mathbf{p}*_a\mathbf{E}'(\boldsymbol{\rho}_a)\} \tag{1.33}$$

where $\mathbf{E}'(\rho_a)$ is the field of the wave incident on the a-th dipole

$$E'_a(\boldsymbol{\rho}_a)=E_0(\boldsymbol{\rho}_a)+\sum_{a\neq b}E_b(\boldsymbol{\rho}_a) \tag{1.34}$$

Assuming that the dipole moment p_a is a linear function of the electric field $\mathbf{E}'(\boldsymbol{\rho_a})$ equation (1.33) becomes

$$i\pi k_0^2|\mathbf{p_a}|=\frac{e^{i\phi_a}-1}{2}\mathbf{E}'(\boldsymbol{\rho_a}). \tag{1.35}$$

where ϕ_a, is some arbitrary real number. Thus, to provide energy conservation, the dipole moment must be coupled to the electric field of the incident wave by a complex "polarizability" $(e^{i\phi_a}-1)/2$ which phase of the a-th scatterer shows frequency dependence $\phi_a=\phi_a(k)$. This fact is not specific for the considered two-dimensional case; it remains valid also in three dimensions, as it will be shown for the sake of completeness in 1.1.3. Inserting (1.35) into (1.30), using (1.34), and introducing the following convenient notation for the 2D Green function

$$\pi G_{a,b}=(1-\delta_{a,b})\ g_{(2)}(\boldsymbol{\rho}-\boldsymbol{\rho_a})=(1-\delta_{a,b})i\pi H_0^{(1)}(k_0|\boldsymbol{\rho}-\boldsymbol{\rho_a}|), \tag{1.36}$$

[2]The Hankle function of the first kind is also known an Bessel function of the third kind

one obtains a linear system of N equations which solutions are the stationary electric field distributions at the position of any a-th dipole

$$E'_a(\boldsymbol{\rho}_a) = E_0(\rho_a) + \frac{1}{2i}\sum_{b=1}^{N} G_{a,b}(e^{i\phi_b} - 1)E'_b(\boldsymbol{\rho}_b) \tag{1.37}$$

with a in the range 1,...,N. The modes of the system are the solutions of equation (1.37) without source, thus, once assumed that the scattering properties are the same for all dipoles (this means $\phi_b = \phi$), the modes are the solutions of the following eigenvalue problem

$$\sum_{b=1}^{N} G_{a,b}\ E'_b(\boldsymbol{\rho}_b) = \frac{2i}{(e^{i\phi} - 1)}\ E'_a(\boldsymbol{\rho}_a). \tag{1.38}$$

To conclude, starting from Maxwell equations in a medium and studying the field generated by N dipoles with the same resonant frequency and same dipole moment, the modes supported by the systems are eigenvectors of the $N \times N$ Green matrix.

1.1.3 Eigenvalue problem in the 3D case

The same eigenvalue problem can be formulated starting from the general concept of single scattering in 3D space and requiring the validity of the optical theorem [14]. Considering a single scattering particle with refractive index $n(\mathbf{r})$ and volume V in an host medium with refractive index n, assuming again a non-magnetic systems without charges and currents, it is possible to perform the time derivative of Maxwell equation (1.3) to retrieve the following expression[3]:

$$-\frac{n(\mathbf{r})}{c^2}\frac{\partial^2 \mathbf{E}}{\partial t^2} + \nabla^2\mathbf{E} - \boldsymbol{\nabla}(\boldsymbol{\nabla}\cdot\mathbf{E}) = 0 \tag{1.39}$$

that in the case of a time-harmonic dependence of the field become

$$\nabla^2\mathbf{E}(\mathbf{r}) + k^2\mathbf{E} = F(\mathbf{r})\mathbf{E}(\mathbf{r}) + \boldsymbol{\nabla}(\boldsymbol{\nabla}\cdot\mathbf{E}(\mathbf{r})) \tag{1.40}$$

where $k = n_0\omega/c$ and $F(\mathbf{r}) = k^2(n(\mathbf{r})^2/n_0^2 - 1)$ usually called *scattering potential*, vanishing for $\mathbf{r}$ outside V. The equation represent the scattering problem for vector wave, taking into account the change in polarization due to the presence of the source term $\boldsymbol{\nabla}(\boldsymbol{\nabla}\cdot\mathbf{E}(\mathbf{r}))$, which couple the Cartesian components of $\mathbf{E}$. In the scalar approximation, i.e. ignoring polarization effect and approximating the field to scalar waves, the coupling term is neglected and (1.40) become

$$\nabla^2 E(\mathbf{r}) + k^2 E = F(\mathbf{r})E(\mathbf{r}) \tag{1.41}$$

[3]The identity $\boldsymbol{\nabla}\boldsymbol{\nabla}\cdot a = \boldsymbol{\nabla}\times\boldsymbol{\nabla}\times\mathbf{a} + \nabla^2 a$ has been used

which solution can be written as the combination of an incident and a scattered field $E(\mathbf{r}) = E_0(\mathbf{r}) + E_{sca}(\mathbf{r})$, with $E_0(\mathbf{r})$ incident field and

$$E_{sca}(\mathbf{r}) = \int_V F(\mathbf{r}')E(\mathbf{r}')G(\mathbf{r},\mathbf{r}')\,\mathrm{d}\mathbf{r}\prime \tag{1.42}$$

with $G(\mathbf{r},\mathbf{r}') = \exp(ik|\mathbf{r}-\mathbf{r}'|)/4\pi|\mathbf{r}-\mathbf{r}'|$ free-space outgoing Green function. In the far-field ($r >> r'$) the Green function can be factorized in $G(\mathbf{r},\mathbf{r}') = \exp(ikr)\exp(-ik\mathbf{s}\cdot\mathbf{r}')/4\pi r$, with $\mathbf{s}$ unit vector along $\mathbf{r}$. Considering an incident plane wave $E_0(\mathbf{r}) = E_0\exp(ik\mathbf{s}_0\cdot\mathbf{r})$ propagating along the direction of the unit vector $\mathbf{s}_0$, the expression for the scattered field become

$$E_{sca}(\mathbf{r}) = E_0 f(\mathbf{s},\mathbf{s}_0)\frac{e^{ikr}}{r} \tag{1.43}$$

where the $f(\mathbf{s},\mathbf{s}_0)$ is the *scattering amplitude* defined as

$$f(\mathbf{s},\mathbf{s}_0) = \frac{1}{4\pi}\int_V F(\mathbf{r}')\frac{E(\mathbf{r}')}{E_0}e^{-ik\mathbf{s}\cdot\mathbf{r}'}\,\mathrm{d}\mathbf{r}' \tag{1.44}$$

defined respect to the incident direction $\mathbf{s_0}$. To further simplify calculations let's assume that the scattering particle is spherically symmetric and placed at $\mathbf{r}$=0. The far-field wave function can be written as

$$E(\mathbf{r}) \simeq e^{ikr} + f(k)\frac{e^{ikr}}{r}, \tag{1.45}$$

with $f(k)$ scattering amplitude depending only by the wavenumber due to the particle symmetry. As it has been done before, the size of the particle is neglected, requiring the conservation of energy as the only criteria to find an expression for the particle polarizability. Assuming the scattering as elastic, the optical theorem[4] holds

$$|f(k)|^2 = \frac{1}{k}Im\{f(k)\}. \tag{1.46}$$

This requirement allows to determine the scattering amplitude of the process

$$f(k) = \frac{e^{i2\delta(k)}-1}{2ik} \tag{1.47}$$

The total electric field scattered by the N-particle system is again the sum of the incident field $E_0(\mathbf{r})$ and the field scattered by each particles

$$E(\mathbf{r}) = E_0(\mathbf{r}) + \sum_{j=1}^{N} f_j(k)\frac{e^{ik|\mathbf{r}-\mathbf{r_j}|}}{|\mathbf{r}-\mathbf{r_j}|}. \tag{1.48}$$

Assuming, like it have been done for the 2D case, that all the particle exhibit the same scattering properties, i.e. the same scattering amplitude, the field acting on the a-th

[4] Derivation of the optical theorem can be found in subsection 1.2.2.

dipole can be written as

$$E(\mathbf{r_a}) = E_0(\mathbf{r_a}) + \frac{e^{i2\delta(k)} - 1}{2i} \sum_{a \neq b} \frac{e^{ik|\mathbf{r_a} - \mathbf{r_b}|}}{|\mathbf{r_a} - \mathbf{r_b}|} E(\mathbf{r_b}). \tag{1.49}$$

that leads, requiring $E_0(\mathbf{r_a}) = 0$ to obtain the system modes, to the analogous eigenvalue problem

$$\sum_{b=1}^{N} G_{a,b}^{3D} E(\mathbf{r_b}) = \frac{2i}{e^{i2\delta(k)} - 1} E(\mathbf{r_a}). \tag{1.50}$$

where $G_{a,b}^{3D} = e^{ik|\mathbf{r_a} - \mathbf{r_b}|}/|\mathbf{r_a} - \mathbf{r_b}|$ is the 3D Green function term. The physical meaning of the eigenvalues and the mode features for different type of systems are deeply examine in Chapter 2.

1.2 From Maxwell Equation to Radiative Transfer Theory

In the previous section, the electrodynamics problem of modes arising from interference effect between waves scattered by dipoles have been addressed using Maxwell equation. The resulting expression (1.49) can be thought in the frame of multiple scattering theory as the Born expansion, truncated to the first order (single scattering approximation), in a system of general shaped particles. This means that, from an infinite series where each n-th order term represents the electric field contribute n times scattered by particles, only the first order, i.e. the single scattering between every couple of particles, is considered. Taking into account also higher order terms allows to solve exactly light transport problem for every type of system, determining analytically all the effect of multiple scattering, diffraction and interference. However, multiple scattering theory is not the most common formalism used for disorder media description. For more than 100 years disorder media light propagation have been tackled with a simple and intuitive heuristic theory, the radiative transfer equation (RTE). This is a phenomenological expression of the transport problem that lacks of a rigorous mathematical formulation but able to account for all the physical effects involved in light propagation. Despite apparently unrelated to the laws of classical electrodinamics, the striking success of the theory proved RTE to be valid in many different fields providing useful models for many practical problems [15]. Shortly after the formulation in the sixties, a first rigorous mathematical relation between RTE and classical electrodynamics have been established in 1975 by G. C. Papanicolaou and R. Burridge, that, following a perturbation procedure, derived RTE from Maxwell equations in continuous random media [16]. More recently, it has been demonstrated by Tsang [17] and Mishchenko [18, 19] that, under certain simplifying assumptions, the RTE can be derived from Maxwell equations also in discrete multiple scattering media. In the following part the procedure to retrieve the RTE from Maxwell equations is presented. The derivation is based on references [18, 20]. From RTE, a further widely used approximation suitable to simplify calculations and to successfully interpret light transport in random media is described: the diffusion approximation. Making proper assumptions, the RTE becomes a diffusion equation (DE), i.e the intensity propagation is described as a diffusion process. That is the theory

employed to study the exotic disordered network in chapter 4.

1.2.1 Poynting theorem and energy conservation

RTE is based on the condition of energy conservation, requiring a balance of the quantity of energy

$$I(\mathbf{r}, t, s)\,\mathrm{d}t\,\mathrm{d}S\cos\theta\,\mathrm{d}\Omega \tag{1.51}$$

radiated per unit of time $\mathrm{d}t$ into a solid angle $\mathrm{d}\Omega$ pointed by a unit vector s forming an angle θ with the normal of a small area $\mathrm{d}S$. The quantity $I(r, t, s)$ [$\mathrm{Wm^{-2}sr^{-1}}$] is called *specific intensity* and represents the main concept underlying the description of light transport in disordered media. The concept of an angular-dependent flow of energy expressed by $I(\mathbf{r}, t, \mathbf{s})$ has no direct counterpart in electromagnetic theory, where the Poynting vector field assumes a single value (and therefore a unique direction) in each point in space. The connection with Maxwell equations can be established [18, 20] considering a volume-averaged definition of the continuous Poynting vector field [15]. To explain this idea, we now consider an isotropic medium with permeability μ and dielectric permittivity ϵ. Maxwell equations can be expressed as

$$\boldsymbol{\nabla}\cdot\mathbf{E} = \frac{\rho}{\epsilon_0} \tag{1.52}$$

$$\boldsymbol{\nabla}\cdot\mathbf{B} = 0 \tag{1.53}$$

$$\boldsymbol{\nabla}\times\mathbf{E} = -\frac{\partial\mathbf{B}}{\partial t} \tag{1.54}$$

$$\boldsymbol{\nabla}\times\mathbf{B} = \epsilon\mu\frac{\partial\mathbf{E}}{\partial t} + \mu\mathbf{j}. \tag{1.55}$$

By multiplying (1.54) and (1.55) by $\mathbf{B}$ and $\mathbf{E}$ respectively, and taking their difference, we can rewrite

$$\frac{1}{\mu}\boldsymbol{\nabla}\cdot(\mathbf{E}\times\mathbf{B}) = \frac{1}{\mu}\left(\epsilon\mu\mathbf{E}\cdot\frac{\partial\mathbf{E}}{\partial t} + \mathbf{B}\frac{\partial\mathbf{B}}{\partial t}\right) - \mathbf{E}\cdot\mathbf{j} \tag{1.56}$$

where the vector identity $\boldsymbol{\nabla}\cdot(\mathbf{a}\times\mathbf{b}) = \mathbf{b}\cdot(\boldsymbol{\nabla}\times\mathbf{a}) - \mathbf{a}\cdot(\boldsymbol{\nabla}\times\mathbf{b})$ have been used. In (1.56) one can recognize both the partial time derivative of the total electromagnetic energy

$$W(\mathbf{r}, t) = \frac{1}{2\mu}\left(\frac{1}{c^2}\mathbf{E}\cdot\mathbf{E} + \mathbf{B}\cdot\mathbf{B}\right) \tag{1.57}$$

and the divergence of the energy flux density

$$\mathbf{S} = \frac{1}{\mu}\mathbf{E}\times\mathbf{B}, \tag{1.58}$$

that makes (1.56) a continuity relation bounding the electromagnetic energy and its flux. The term $\mathbf{E}\cdot\mathbf{j}$ represent the Joule heating, that is the dissipation of energy due to absorption by charges. Energy dissipation in an isotropic medium is defined by Ohm's

law as $\mathbf{j} = \omega\epsilon''\mathbf{E}$, where ω is the frequency of the electromagnetic wave and ϵ'' is the imaginary part of the permittivity $\epsilon = \epsilon'(\mathbf{r}) + i\epsilon''(\mathbf{r})$. Joule heating can therefore be formulated in terms of the absorbed energy per unit volume

$$\frac{\mathrm{d}P_{abs}}{\mathrm{d}V} = \mathbf{E}\cdot\mathbf{j} = \omega\epsilon''\mathbf{E}^2, \tag{1.59}$$

that gives the Poynting theorem

$$\frac{\partial W}{\partial t} + \frac{\mathrm{d}P_{abs}}{\mathrm{d}V} + \boldsymbol{\nabla}\cdot\mathbf{S} = 0 \tag{1.60}$$

valid for time-harmonic electromagnetic field with $\mathbf{E}$ and $\mathbf{B}$ mutually orthogonal. However, as the period of an electromagnetic wave in the optical frequency range is several orders of magnitude smaller than any experimental time measurement, we are rather interested in time-averaged quantities. Expressing $\mathbf{E}(\mathbf{r},t)$ and $\mathbf{B}(\mathbf{r},t)$ as plane wave solutions of Maxwell equations

$$\mathbf{E}(\mathbf{r},t) = E_0\hat{e}e^{i\mathbf{k}\cdot\mathbf{r}}e^{-i\omega t} \tag{1.61}$$

$$\mathbf{B}(\mathbf{r},t) = \sqrt{\epsilon\mu}E_0\hat{b}e^{i\mathbf{k}\cdot\mathbf{r}}e^{-i\omega t} \tag{1.62}$$

the time-averaged Poyinting vector is

$$\langle\mathbf{S}\rangle \backsimeq \frac{1}{T}\int_0^T \frac{1}{\mu}\left[\mathbf{E}(\mathbf{r},t)\times\mathbf{B}(\mathbf{r},t)\right]\mathrm{d}t = \frac{E_0}{2}\sqrt{\frac{\epsilon}{\mu}}\mathbf{s} \tag{1.63}$$

with $\mathbf{s}$ unit vector in the direction perpendicular to both $\mathbf{E}$ and $\mathbf{B}$. This means that the validity of the time-averaged expression for the Poynting vector that we derived is limited to the far-field, where the electromagnetic fields propagate as a plane wave directed towards $\mathbf{s}$. Keeping in mind this assumption, we can analogously derive time-averaged expressions for the energy density and the absorbed power

$$\langle W\rangle = \frac{\epsilon_0}{2}|\mathbf{E}_0|^2 = \sqrt{\epsilon\mu}\,\langle\mathbf{S}\rangle\cdot\mathbf{s} \tag{1.64}$$

$$\left\langle\frac{\mathrm{d}P_{abs}}{\mathrm{d}V}\right\rangle = \frac{1}{2}\omega\epsilon''|\mathbf{E}_0|^2 = \sqrt{\frac{\mu}{\epsilon}}\omega\epsilon''\,\langle\mathbf{S}\rangle\cdot\mathbf{s}. \tag{1.65}$$

Using the time-averaged formulas (1.63), (1.64) and (1.65) and writing the speed of light in the medium as $v = 1/\sqrt{\epsilon\mu}$ one gets

$$\frac{1}{v}\frac{\partial\,\langle\mathbf{S}(\mathbf{r})\rangle\cdot\mathbf{s}}{\partial t} + \left\langle\frac{\mathrm{d}P_{abs}}{\mathrm{d}V}\right\rangle + \boldsymbol{\nabla}\cdot\langle\mathbf{S}(\mathbf{r})\rangle = 0 \tag{1.66}$$

which is the time-averaged expression of (1.60) and represents the conservation of energy flux along the direction of the Poynting vector $\mathbf{s}$. Of course, energy conservation must keep its validity along any arbitrary direction $\mathbf{s_j}$, and we can rewrite

$$\frac{1}{v}\frac{\partial\,\langle\mathbf{S}(\mathbf{r})\rangle\cdot\mathbf{s_j}}{\partial t} + \left\langle\frac{\mathrm{d}P_{abs}}{\mathrm{d}V}\right\rangle(\mathbf{s}\cdot\mathbf{s}_j) + \mathbf{s}_j\cdot\boldsymbol{\nabla}(\langle\mathbf{S}(\mathbf{r})\rangle\cdot\mathbf{s}_j) = 0 \tag{1.67}$$

where the following relation has been used

$$\boldsymbol{\nabla} \cdot (\langle \mathbf{S}(\mathbf{r}) \rangle \cdot \mathbf{s}_j) \cdot \mathbf{s}_j = \boldsymbol{\nabla} (\langle \mathbf{S}(\mathbf{r}) \rangle \cdot \mathbf{s}_j). \tag{1.68}$$

Equation (1.67) expresses that energy conservation is rotational invariant, i.e. that power is conserved irrespective of the angle between the detector and the power flux. The total power measured experimentally by a detector of area A placed at $\mathbf{r}$ with surface normal $\mathbf{n}$ can be therefore expressed as $P(\mathbf{r}) = \int_A \langle \mathbf{S}(\mathbf{r}') \rangle \cdot \mathbf{n} \, \mathrm{d}S'$. Finally, in the case of a non-absorbing medium ($\mathrm{d}P_{abs}/\mathrm{d}V{=}0$) under continuous illumination ($\partial \langle W(\mathbf{r}, t) \rangle / \partial t{=}0$) which contains no sources, the conservation of energy simply states $\boldsymbol{\nabla} \cdot \langle \mathbf{S} \rangle$ or, alternatively, that the averaged total flux of energy $\int_\Sigma \langle \mathbf{S} \rangle \cdot \mathbf{n} \, \mathrm{d}S$ through any closed surface Σ is zero.

1.2.2 Single scattering optical parameters

In section 1.1.3, a description of the single particle scattering has been introduced, defining one of the quantities that relates incident field and spherical wave scattered by the particle. It is possible to define now the components of the time-averaged Poynting vector $\langle \mathbf{S}_{sca} \rangle$ associated with the incident and scattered fields

$$\langle \mathbf{S}_{inc} \rangle = \frac{|\mathbf{E}_0|^2 \epsilon v}{2} \mathbf{s}_0 \tag{1.69}$$

$$\langle \mathbf{S}_{sca} \rangle = \frac{|\mathbf{E}_0|^2 \epsilon v}{2} \frac{|f(\mathbf{s}, \mathbf{s}_0)|^2}{r^2} \mathbf{s}. \tag{1.70}$$

Using (1.43), several common quantities which refer directly to the properties of the particle can be defined, eventually used to investigate collective scattering properties from more than one particle, and therefore exploited in the study of light propagation in a disorder medium. Considering the amount of energy lost due to absorption in the interaction of the incident light with the particle, an expression for $\langle P_{abs} \rangle$ can be formulated

$$\langle P_{abs} \rangle = \int_V \left\langle \frac{\mathrm{d}P_{abs}}{\mathrm{d}V} \right\rangle \mathrm{d}V = \frac{\omega}{2} \int_V \epsilon'(\mathbf{r}) |\mathbf{E}(\mathbf{r})|^2 \, \mathrm{d}V \tag{1.71}$$

representing the amount of energy lost per unit of time due to absorption. Normalizing this power by the energy rate impinging on the particle, we obtain the absorption cross-section

$$\sigma_a = \frac{\langle P_{abs} \rangle}{\langle \mathbf{S}_{inc} \rangle} = \frac{k}{2 E_0^2 \epsilon} \int_V \epsilon'(\mathbf{r}) |\mathbf{E}(\mathbf{r})|^2 \, \mathrm{d}V \tag{1.72}$$

which depends solely on the material properties of the particle and its geometry. A scattering cross-section is similarly obtained as

$$\sigma_{sca} = \frac{\langle P_{sca} \rangle}{\langle \mathbf{S}_{inc} \rangle} = \int_V \frac{\boldsymbol{\nabla} \cdot \mathbf{S}_{sca}}{\langle \mathbf{S}_{inc} \rangle} \, \mathrm{d}V = \int_S \frac{\mathbf{S}_{sca} \cdot \mathbf{n}}{\langle \mathbf{S}_{inc} \rangle} \, \mathrm{d}S \tag{1.73}$$

that using (1.70) and (1.69) lead to

$$\sigma_{sca} = \int_S |f(\mathbf{s}, \mathbf{s}_0)|^2 \frac{\mathrm{d}S}{r^2} = \int_{4\pi} |f(\mathbf{s}, \mathbf{s}_0)|^2 \, \mathrm{d}\Omega \tag{1.74}$$

where $\mathrm{d}S\,/r^2$ have been substituted with the solid angle $\mathrm{d}\Omega$ assuming that the center of integration is positioned at the center of the particle. The sum of the absorption and scattering cross-sections is usually indicated as the total or extinction cross-section

$$\sigma_{tot} = \sigma_{sca} + \sigma_{abs} \tag{1.75}$$

which is a particularly relevant microscopic quantity since it depends only on the incident direction of propagation and can be measured experimentally in the far-field. This quantity provides important information on the microscopic properties of a scattering particle through the optical theorem, already mentioned in section 1.1.3, that can be formulated in terms of σ_{tot} as

$$\sigma_{tot} = \frac{4\pi}{k} Im(f(\mathbf{s}, \mathbf{s}_0)) = \frac{4\pi}{k^2} |f(\mathbf{s}, \mathbf{s}_0)|^2. \tag{1.76}$$

Another parameter is now introduced, the *phase function*,[5] direct expression of the square modulus of the scattering amplitude

$$p(\mathbf{s}, \mathbf{s}_0) = \frac{1}{\sigma_{tot}} |f(\mathbf{s}, \mathbf{s}_0)|^2. \tag{1.77}$$

The phase function can be interpreted statistically as the probability distribution for incident light on the particle from direction $\mathbf{s}_0$ to be scattered in direction $\mathbf{s}$, that through (1.73) lead to a definition of another quantity, the *albedo*

$$a = \frac{\sigma_{sca}}{\sigma_{tot}} = \int_S p(\mathbf{s}, \mathbf{s}_0) \, \mathrm{d}\Omega \,, \tag{1.78}$$

expressing the absorption of the particle (its value is 1 for non-absorbing particles). The phase function is actually a complex function, that can be solved analytically only for simple shapes of the scatterer. Anyway it is possible to retrieve, in the case of large ensemble of scatterers randomly oriented, an approximated form called Henyey-Greenstein phase function [21]

$$p_{HG}(\mathbf{s}, \mathbf{s}_0) = \frac{a}{4\pi} \frac{1 - g^2}{(1 + g^2 - 2g\mathbf{s} \cdot \mathbf{s}_0)^{3/2}}, \tag{1.79}$$

where g is the *scattering anisotropy factor* ($g \in$[-1,1]), related to the phase function by

$$g = \langle \mathbf{s} \cdot \mathbf{s}_0 \rangle = \langle \cos\theta \rangle = \frac{\int_{4\pi} p(\mathbf{s}, \mathbf{s}_0) \mathbf{s} \cdot \mathbf{s}_0 \, \mathrm{d}\Omega}{\int_{4\pi} p(\mathbf{s}, \mathbf{s}_0) \, \mathrm{d}\Omega}, \tag{1.80}$$

[5] The name phase function is actually misleading, it is not related to the wave phase.

a general parameter expressing the scattering directionality from completely forward ($g = 1$) to completely backwards ($g = -1$), with g=0 representing the isotropic scattering case.

1.2.3 Multiple scattering optical parameters

The introduced optical properties of the single particles will be exploited to formulate the energy density flow $\langle \mathbf{S} \rangle$ for a random ensemble of particles. The field scattered by a system of N particles is the sum of the contributes of the field scattered by every particle, as expressed in (1.48), where each contribute is a function of the scattering amplitude (1.44). Computing the intensity $|\mathbf{E}(\mathbf{r})|^2$ of the total field, sum of the incident field and the field scattered by all the particles $\mathbf{E}(\mathbf{r}) = \mathbf{E}_{inc}(\mathbf{r}) + \mathbf{E}_{sca}(\mathbf{r})$, and writing the results in terms of energy density flow, the following relation is obtained

$$\langle \mathbf{S}(\mathbf{r}) \rangle = \langle \mathbf{S}_{inc}(\mathbf{r}) \rangle + \sum_{i=1}^{N} \langle \mathbf{S}_{sca}(\mathbf{r}) \rangle_i + \sum_{i,j=1 \; i \neq j}^{N} \langle \mathbf{S}_{sca}(\mathbf{r}) \rangle_{i,j} + ... \tag{1.81}$$

where $\langle \mathbf{S}_{sca}(\mathbf{r}) \rangle_i$ is the contribution due to particle i, $\langle \mathbf{S}_{sca}(\mathbf{r}) \rangle_{i,j}$ results from the interference from particle i and j, and all higher order terms have not been written explicitly, as the series contains as many terms as there are combinations between N particles. Assuming that the wavelength of light is much smaller than the typical distances involved in the problem, it is possible to simplify the problem neglecting the interference terms related to scattering between particles. Therefore expression (1.81) becomes

$$\langle \mathbf{S}(\mathbf{r}) \rangle = \langle \mathbf{S}_{inc}(\mathbf{r}) \rangle + \sum_{i=1}^{N} \langle \mathbf{S}_{sca}(\mathbf{r}) \rangle_i \,, \tag{1.82}$$

where the scattering components can be rewritten as

$$\langle \mathbf{S}_{sca}(\mathbf{r}) \rangle_i = \sigma_{tot} \langle \mathbf{S}_{inc}(\mathbf{r}_i) \rangle \cdot \mathbf{s} \frac{p(\mathbf{s}_i, \mathbf{s})}{|\mathbf{r} - \mathbf{r}_i|^2} \mathbf{s}_i \tag{1.83}$$

using the definitions of $\langle \mathbf{S}_{inc} \rangle$ (1.69) and of the phase function (1.77). In many practical situations we do not know the number of particles N nor their sizes or shapes. However, if we assume that they all have the same average radius R and random orientation, we can introduce few average quantities with statistical significance such as the scattering coefficient and the absorption coefficient (or their associated mean free paths)

$$\mu_s = n\sigma_{sca} = \frac{1}{l_s} \tag{1.84}$$

$$\mu_a = n\sigma_{abs} = \frac{1}{l_a}, \tag{1.85}$$

where n is the number density of particles in the element of volume. Finally, to take into account the scattering anisotropy factor g, another quantity is introduced to relate

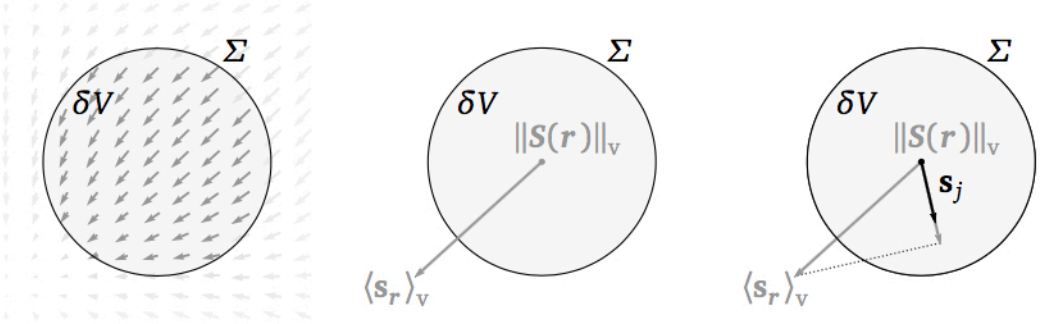

Fig. 1.1: From left to right: representation of the Poynting vector field $\langle \mathbf{S}(\mathbf{r}') \rangle$ evaluated at $r' \in \delta V$. Averaging over the differential volume δV we obtain a volume-averaged flow of energy $\|\mathbf{S}(\mathbf{r})\|_V$ pointing at an average direction $\langle \mathbf{s}(\mathbf{r}) \rangle_V$, with different projections along arbitrary directions $\mathbf{s}_j$.

the scattering coefficient of an anisotropic particle to that of an isotropic one

$$\mu_s' = \mu_s(1-g) = \frac{1}{l_t} \tag{1.86}$$

which is called the reduced scattering coefficient. Its inverse, the reduced scattering mean free path or transport mean free path l_t, represents the distance that light needs to travel before it loses every residual correlation with its original direction of propagation. This distance diverges asymptotically as $g \longrightarrow 1$, while it is equivalent to l_s for $g = 0$, consistently with the definition of isotropic scattering. As we will see in the following, this relation expresses the fact that, under the diffusive approximation, the transport of light in a medium characterized by scattering parameters μ_s and $g \neq 0$ can be mapped identically into that of a system with μ_s' and $g = 0$. This degeneracy is usually recognized as the similarity relation [22, 23]. It is important to stress the statistical nature of the parameters that we introduced to describe radiative transport. Both the scattering/absorption coefficients and our choice of a phase function are basically independent of the actual size and properties of each individual particle, and make sense only from a statistical point of view. In most applications, though, this statistical approach and the loss of wave properties that characterizes multiple scattering in the radiative transfer framework does not constitute a problem.

1.2.4 Specific intensity, average intensity and flux

In order to derive the RTE, we consider the time-averaged Poynting vector $\langle \mathbf{S} \rangle = S\mathbf{s}$, computing its average over a small volume δV [20, 15]. For each point $\mathbf{r}' \in \delta V$ the Poynting vector has a well defined value $\langle \mathbf{S}(\mathbf{r}') \rangle$ pointing along a certain direction $\mathbf{s}'$ (Figure 1.1). The resulting integral can have contributions along any direction $\mathbf{s}_j$, each one with a normalized weight

$$w_{\mathbf{r}}(\mathbf{s}_j) = \frac{1}{\delta V \|\mathbf{S}(\mathbf{r})\|_V} \int_{\delta V} S(\mathbf{r}-\mathbf{r}')\mathbf{s}' \cdot \mathbf{s}_j \, \mathrm{d}\mathbf{r}' \tag{1.87}$$

where $\|\mathbf{S}(\mathbf{r})\|_V$ is the magnitude of volume-averaged flow

$$\|\mathbf{S}(\mathbf{r})\|_V = \frac{1}{\delta V}\int_{\delta V} S(\mathbf{r}-\mathbf{r}')\mathbf{s}'\,\mathrm{d}\mathbf{r}'\,. \tag{1.88}$$

We can now express the average direction of energy flow

$$\langle \mathbf{s}(\mathbf{r})\rangle_V = \frac{1}{4\pi}\int_{4\pi} w_{\mathbf{r}}(\mathbf{s}_j)\mathbf{s}_j\,\mathrm{d}\Omega \tag{1.89}$$

and finally write the volume-averaged energy flow as

$$\langle \mathbf{S}(\mathbf{r})\rangle_V = \|\mathbf{S}(\mathbf{r})\|_V \langle \mathbf{s}(\mathbf{r})\rangle_V \tag{1.90}$$

which is the quantity that will be used to establish a connection with the concept of specific intensity. As we mentioned at the beginning of section 1.2, the specific intensity represents the amount of power per unit area that flows in a certain direction defined by a unit solid angle. In terms of the average energy flow defined in equation (1.90), we can define it as

$$I(\mathbf{r},t,\mathbf{s}) = \frac{1}{4\pi}\|\mathbf{S}(\mathbf{r})\|_V w_{\mathbf{r}}(\mathbf{s}) \tag{1.91}$$

where $w_{\mathbf{r}}(\mathbf{s})$ expresses the probability of the averaged flow to point in direction $\mathbf{s}$ as shown in equation (1.87). We must note that the specific intensity is inherently referred to a certain frequency interval: we will in general omit such dependence and consider quasi-monochromatic light.
Starting from the specific intensity, another relevant quantity that we can derive is the average intensity at a point $\mathbf{r}$, expressed as the volume average of the Poynting vector integrated over all directions,

$$U(\mathbf{r},t) = \int_{4\pi} I(\mathbf{r},t,\mathbf{s})\,\mathrm{d}\Omega = \frac{1}{4\pi}\|\mathbf{S}(\mathbf{r})\|_V \int_{4\pi} w_{\mathbf{r}}(\mathbf{s})\,\mathrm{d}\Omega = \|\mathbf{S}(\mathbf{r})\|_V \tag{1.92}$$

which is equal to the magnitude of the volume averaged energy flow. Related to this expression, a quantity that is commonly used in the radiative transfer formalism is the energy density $u(\mathbf{r},t)$. A convenient way to define it is to consider the definition of energy density (1.65) that we obtained directly from Maxwell equations and relate it to the volume averaged Poynting vector, obtaining

$$u(\mathbf{r},t) = \frac{1}{v\delta V}\int_{\delta V} |\left\langle \mathbf{S}(\mathbf{r}-\mathbf{r}')\right\rangle| = \frac{1}{v}\|\mathbf{S}(\mathbf{r})\|_V = \frac{U(\mathbf{r},t)}{v}. \tag{1.93}$$

Neither $U(\mathbf{r},t)$ nor $u(\mathbf{r},t)$ contain any information regarding the average direction of propagation, though. The main quantity that is connected to the overall flux of energy is the flux density

$$\mathbf{F}(\mathbf{r},t) = \int_{4\pi} I(\mathbf{r},t,\mathbf{s})\mathbf{s}\,\mathrm{d}\Omega = \frac{1}{4\pi}\|\mathbf{S}(\mathbf{r})\|_V \int_{4\pi} w_{\mathbf{r}}(\mathbf{s})\mathbf{s}\,\mathrm{d}\Omega = \|\mathbf{S}(\mathbf{r})\|_V \langle \mathbf{s}(\mathbf{r})\rangle_V\,. \tag{1.94}$$

which is a vector with magnitude and direction of the average flow of electromagnetic energy, already described in (1.90).

1.2.5 Derivation of RTE

Now that all the quantities necessary to retrieve the RTE from classical electrodynamics have been introduced, a connection between the Maxwell equation and the RTE will be established computing the volume average of the Poynting theorem (1.60). Using the time-average expression for the Poynting vector (1.66), valid in the far-field of the scattering system, and integrating over a small volume δV containing N particles with absorption cross-section σ_{abs} and scattering cross-section σ_{sca}, one gets

$$\int_{\delta V} (\mathbf{s}\cdot\mathbf{s}_j)\left[\frac{1}{v}\frac{\partial S(\mathbf{r}-\mathbf{r}')}{\partial t} + \left\langle \frac{\mathrm{d}P_{abs}}{\mathrm{d}V}\right\rangle + \mathbf{s}_j\cdot\nabla_{\mathbf{r}'}S(\mathbf{r}-\mathbf{r}')\right]\mathrm{d}\mathbf{r}' = 0. \tag{1.95}$$

This is the RTE expressed in terms of Poyting vector. The three terms indicates respectively: the volume-averaged change in energy density, the volume-averaged absorbed power, the volume-averaged change in energy flow. Performing several approximation and formulating this equation in term of specific intensity, the usual RTE can be written. The first term is analogue to the *dipolar approximation* in multiple scattering, therefore, separating $\langle\mathbf{S}\rangle$ in the incident $\langle\mathbf{S}_{inc}\rangle$ and scattered $\langle\mathbf{S}_{sca}\rangle$ and assuming that the volume associated to $\langle S_{inc}\rangle$ $V-\delta V$ is much larger than δV, the following condition is satisfied:

$$\int_{\delta V}\langle\mathbf{S}_{inc}\rangle\cdot\mathbf{s}_j\,\mathrm{d}V >> \int_{\delta V}\langle\mathbf{S}_{sca}\rangle\cdot\mathbf{s}_j\,\mathrm{d}V\,. \tag{1.96}$$

This consists in assuming the incident field on each particle simply given by the sum of all scattered fields excluded its own. This small size of δV justifies another assumption, that the incident field flux at any point inside such sample volume can be approximated to the volume-averaged incident flow

$$\langle\mathbf{S}_{inc}(\mathbf{r})\rangle\cdot\mathbf{s} \simeq \|\mathbf{S}_{inc}(\mathbf{r})\|_V \tag{1.97}$$

with $\mathbf{s}$ unit vector in the direction of the energy flow at $\mathbf{r}$. Applying these two approximation to the first two terms of (1.95) and requiring that the far-field approximation is valid within δV, i.e.

$$\frac{1}{v}\frac{\partial}{\partial t}\int_{\delta V}\langle\mathbf{S}\rangle\cdot\mathbf{s}_j\,\mathrm{d}V \simeq \frac{1}{v}\frac{\partial}{\partial t}\|\mathbf{S}_{inc}(\mathbf{r})\|_V w_{\mathbf{r}}(\mathbf{s}_j)\delta V, \tag{1.98}$$

$$\int_{\delta V}\left\langle\frac{\mathrm{d}P_{abs}}{\mathrm{d}V}\right\rangle\cdot(\mathbf{s}\cdot\mathbf{s}_j)\,\mathrm{d}V \simeq N\sigma_{abs}\|\mathbf{S}_{inc}(\mathbf{r})\|_V w_{\mathbf{r}}(\mathbf{s}_j), \tag{1.99}$$

it is possible to rewrite them in terms of the incident flux. Than the third term becomes

$$\int_{\delta V}(\mathbf{s}\cdot\mathbf{s}_j)\mathbf{s}_j\cdot\nabla_{\mathbf{r}'}S(\mathbf{r}-\mathbf{r}')\,\mathrm{d}\mathbf{r}' = w_{\mathbf{r}}(\mathbf{s}_j)\|\nabla_{\mathbf{r}'}\mathbf{S}_{inc}\cdot\mathbf{s}_j\|_V\delta V \tag{1.100}$$

$$+ w_{\mathbf{r}}(\mathbf{s}_j)\int_{\delta V}\mathbf{s}_j\cdot\nabla_{\mathbf{r}'}S_{sca}(\mathbf{r}-\mathbf{r}')\,\mathrm{d}\mathbf{r}' \tag{1.101}$$

where the volume average change in $\langle \mathbf{S} \rangle$ have been introduced

$$\|\nabla_{\mathbf{r}'} \mathbf{S}_{inc} \cdot \mathbf{s}_j\|_V \delta V = \frac{1}{\delta V}(\mathbf{s}_j) \int_{\delta V} \mathbf{s}_j \cdot \nabla_{\mathbf{r}'} S_{inc}(\mathbf{r} - \mathbf{r}') \, \mathrm{d}\mathbf{r}' \,. \tag{1.102}$$

It has already be pointed out at the beginning of the section that the expression (1.66) considered for the time-averaged Poynting vector in (1.95) is valid in the far-field approximation. This corresponds to assume that the far-field approximation is valid in the volume δV. Now requiring that δV is small enough to justify $\mathbf{r} \simeq \mathbf{r}'$ and $\nabla_{\mathbf{r}} \longleftrightarrow \nabla_{\mathbf{r}'}$, we can write

$$\|\nabla_{\mathbf{r}'} \mathbf{S}_{inc} \cdot \mathbf{s}_j\|_V \simeq \mathbf{s}_j \cdot \boldsymbol{\nabla} \|\mathbf{S}_{inc}\|_V, \tag{1.103}$$

that can be inserted into (1.101). Applying the Gauss theorem to the last term of (1.101), we obtain

$$\int_{\delta V} \mathbf{s}_j \cdot \nabla_{\mathbf{r}'} S_{sca}(\mathbf{r} - \mathbf{r}') \, \mathrm{d}\mathbf{r}' = \int_{\Sigma} S_{sca}^{(out)}(\mathbf{r} - \mathbf{r}') \mathbf{s}_j \cdot \mathbf{s}' \, \mathrm{d}S' \int_{\Sigma} S_{sca}^{(inc)}(\mathbf{r} - \mathbf{r}') \mathbf{s}_j \cdot \mathbf{s}' \, \mathrm{d}S' \tag{1.104}$$

where Σ is the surface enclosing δV. The outward flux represents the contribute from the scattering of the N particles inside δV and the inward flux corresponds to the contribution from the all outer volume $V - \delta V$. As the average scattering properties are homogeneous in every position, it is correct to require that the total inward and outward fluxes are equivalent at each boundary between volume elements δV. Thus we can write for each $\mathbf{r}$ on Σ and

$$\int_{\Sigma} S_{sca}^{(inc)}(\mathbf{r} - \mathbf{r}') \mathbf{s}_j \cdot \mathbf{s}' \, \mathrm{d}S' \simeq \sum_{i=1}^{N} \int_{\Sigma} (\langle \mathbf{S}_{sca}(\mathbf{r}) \rangle_i \cdot \mathbf{s}_i)) \mathbf{s}_j \cdot \mathbf{s}' \, \mathrm{d}S' \tag{1.105}$$

where the $\langle \mathbf{S}_{sca}(\mathbf{r}) \rangle_i$ is the energy flux scattered inside δV by the i-th particle, given by (1.83). Using (1.83) and the approximation (1.97) the following expression for the inward flux is obtained

$$\int_{\Sigma} S_{sca}^{(inc)}(\mathbf{r} - \mathbf{r}') \mathbf{s}_j \cdot \mathbf{s}' \, \mathrm{d}S' \simeq N \sigma_{tot} \|\mathbf{S}_{inc}(\mathbf{r})\|_V \int_{4\pi} w_{\mathbf{r}}(\mathbf{s}') p(\mathbf{s}', \mathbf{s}_j) \, \mathrm{d}\Omega \tag{1.106}$$

where, exploiting that the flux does not depend from the position of the particle in δV, $\mathrm{d}S' / |\mathbf{r} - \mathbf{r}_i|^2$ have been substituted with $\mathrm{d}\Omega$.
Now we have all the three expressions for the three terms in the volume average of the Poyting theorem for energy conservation (1.95), and normalizing by δV to remove the dependence from the arbitrary averaging volume, it can be formulated as

$$\frac{1}{v} \frac{\partial}{\partial t} \|\mathbf{S}_{inc}\|_V w_{\mathbf{r}}(\mathbf{s}_j) + \mu_a \|\mathbf{S}_{inc}\|_V w_{\mathbf{r}}(\mathbf{s}_j) + \mathbf{s}_j \cdot \|\mathbf{S}_{inc}\|_V w_{\mathbf{r}}(\mathbf{s}_j) \tag{1.107}$$

$$+ \mu_s \|\mathbf{S}_{inc}\|_V w_{\mathbf{r}}(\mathbf{s}_j) - \mu_{tot} \int_{4\pi} \|\mathbf{S}_{inc}\|_V w_{\mathbf{r}}(\mathbf{s}') p(\mathbf{s}', \mathbf{s}_j) \, \mathrm{d}\Omega' \,. \tag{1.108}$$

This is the radiative transport equation for the time-averaged incoming energy flux $\langle \mathbf{S}_{inc} \rangle$ flowing in the direction $\mathbf{s}_j$, averaged over a volume δV. It is worth to point out that μ_{tot} in the last term appears through the definition of phase function (1.77). It is the product $\mu_{tot} p(\mathbf{s}, \mathbf{s}_0)$ that yields the contribution which is solely due to scattering, i.e. the absorption term related to the phase function that appears through $\mu_{tot} = \mu_a + \mu_s$ has no direct physical meaning. Defining the specific intensity in terms of volume-averaged incident flow

$$I(\mathbf{r}, t, \mathbf{s}) = \frac{1}{4\pi} \|\mathbf{S}_{inc}\|_V w_{\mathbf{r}}(\mathbf{s}'), \tag{1.109}$$

(1.108) recovers the original form of the RTE as formulated from phenomenological arguments in terms of scattering and absorption coefficents [24, 25]

$$\frac{1}{v} \frac{\partial I(\mathbf{r}, t, \mathbf{s})}{\partial t} = -\mathbf{s} \cdot \boldsymbol{\nabla} I(\mathbf{r}, t, \mathbf{s}) + (\mu_s + \mu_a) I(\mathbf{r}, t, \mathbf{s}) + \mu_{tot} \int_{4\pi} I(\mathbf{r}, t, \mathbf{s}') p(\mathbf{s}, \mathbf{s}') \, \mathrm{d}\Omega' \,. \tag{1.110}$$

The RTE in this form represents in a clear way the energy balance for the flow of energy, where the variation of the specific intensity at the position $\mathbf{r}$ at time t along the direction of $\mathbf{s}$ is given by the energy flowing through its boundaries $\mathbf{s} \cdot \boldsymbol{\nabla} I(\mathbf{r}, t, \mathbf{s})$, the losses due to scattering and absorption $(\mu_s + \mu_a) I(\mathbf{r}, t, \mathbf{s})$ and the gain due to scattering from any direction $\mathbf{s}'$ into $\mathbf{s}$, $\mu_{tot} \int_{4\pi} I(\mathbf{r}, t, \mathbf{s}') p(\mathbf{s}, \mathbf{s}') \, \mathrm{d}\Omega'$. Depending on the problem, a gain term $Q(\mathbf{r}, t, \mathbf{s})$ can be added to the second member of the equation to describe the amount of energy introduced in the along $\mathbf{s}$ by an eventual source in the system. A fundamental property of the RTE is the invariance under specific transformations. One of the most relevant is the scale invariance of the solution for a system with $\mu_{tot} = \mu_s + \mu_a$ and phase function $p(\mathbf{s}, \mathbf{s}_0)$:

$$\widetilde{I}(\widetilde{\mathbf{r}}, \widetilde{t}, \mathbf{s}) = \left(\frac{\widetilde{\mu}_{tot}}{\mu_{tot}} \right)^3 I(\mathbf{r}, t, \mathbf{s}) \tag{1.111}$$

with $\widetilde{I}$ solution for a system with extinction coefficient $\widetilde{\mu}_{tot}$, $\widetilde{\mathbf{r}} = \mathbf{r} \mu_{tot} / \widetilde{\mu}_{tot}$ and $\widetilde{t} = t \mu_{tot} / \widetilde{\mu}_{tot}$. This property allows to retrieve easily from a specific geometry result the one for any other rescaled geometry, provided the conservation of the albedo $a = \mu_s / \mu_{tot}$ and $p(\mathbf{s}, \mathbf{s}_0)$ [26]. Another property is the relation between the solutions of RTE with and without absorption, namely

$$I(\mathbf{r}, t, \mathbf{s}) = I(\mathbf{r}, t, \mathbf{s} | \mu_a = 0) e^{-u_a v t}, \tag{1.112}$$

useful to determine numerical solution RTE, since it allows to calculate only one solution per each (μ_s, g) pair, and then apply any μ_a dependence a posteriori [27]. It is now necessary to illustrate the RTE range of applicability, recalling all the approximations performed in the derivation. In order to describe the field scattered by the single particles as an outgoing spherical wave, the far-field approximation have been used, requiring $\mathbf{E}$ and $\mathbf{B}$ mutually orthogonal. Moreover all the derivation have been performed considering additive intensities for the calculation of $\langle \mathbf{S} \rangle$ and neglecting the 2-nd and higher order terms in (1.81), i.e. neglecting the interference effects. Considering the independent

scattering regime, valid in the case of diluite systems, it has been possible to sum incoherently the cross-sections σ_{abs} and σ_{sca}. Secondly, it has been assumed that the sampling volume δV is enough large to contain a statistically representative amount of scatterers, but yet so small to contribute negligibly to the scattered flow from the rest of the sample volume. This approximation has been used also to substitute the Poynting vector within δV with its volume-averaged value. Last, the scalar approximation, used to simplify the calculations and neglect the term $\boldsymbol{\nabla}(\boldsymbol{\nabla} \cdot \mathbf{E})$, coupling the diffent values of the polarization along the cartesian coordinates, in the wave equation (1.40) used to determine the scattering amplitude (1.47) for the single scattering process (subsection 1.2.2). It is important to mention the fact that polarization can be taken into account to formulate the vector RTE, proved to play a non-trivial role in the transport properties analysis [28].
Despite these approximations, it has been observed that the range of applicability of the RTE goes well beyond the one dictated by the assumptions done in its derivation, giving surprisingly reliable results in many physical configurations. Relevant examples lays in the study of systems with thickness comparable to the wavelength [29] or with high density of scatterers. In the latter where the far field and the independent scattering approximations break down, mapping the dependent scattering problem into an independent regime, where effective parameters are chosen according to the spatial correlation in the system introduced by the high degree of packing of the particles [30, 31].

Monte Carlo method for RTE

RTE is an integro-differential equation extremely difficult to solve. Seeking for analytical solutions, a common analytical method is to employ the so-called P_N approximation, consisting in calculating a spherical harmonics expansion of the specific intensity $I(\mathbf{r}, t, \mathbf{s})$ and truncating it at the N-th order. As it will be show in the next section (1.3), truncating this expansion at the first order is possible to approximate the RTE to a diffusion equation. Instead of using an analityical approach, another common procedure to obtain solutions of the RTE consists in using the Monte Carlo method [32, 33, 34]. This is a numerical method to solve physical and mathematical problems based on stochastic processes, that allows to retrieve exact solutions of the RTE for light propagation problems. The method is implemented mapping the multiple scattering inside the medium in a random walk of fictious particles. It is important to point out that this approach is a convenient and simple way to obtain solutions of the transport problems but the particles undergoing the random walk should not be interpreted in the physical picture. The basic idea is to generate a large number of "walkers" undergoing a multiple sequence of scattering events. Both the length and the direction of each step between two different scattering events is sampled numerically from the proper probability distributions, taking into account the degree of anisotropy of the single scattering set throught the parameter g defined in (1.80) and the mean free path of the system defined throught the scattering coefficient in (1.84). Assuming that the radiance is proportional to the particle spatial density, in the limit of an infinite number of generated trajectories, the Monte Carlo method represents an exact solution to the RTE. In this thesis, it has been used to prove that diffusion theory is still valid with

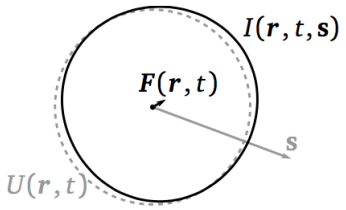

Fig. 1.2: Illustration of the P_1 approximation.

a sufficient approximation in relatively optically thin systems, as reported in Chapter 4.3.1.

1.3 From Radiative Transfer theory to diffusion equation

It has been already pointed out that an analytical solutions of the RTE can be obtained using the P_N approximation. When the transport phenomenon is dominated by multiple scattering, approximating the spherical harmonics expansion of the specific intensity to the first order, i.e. P_1 approximation, it is possible to retrieve from the RTE a diffusive equation (DE) [15, 35]. This method, better known as diffusive approximation, emerges as a widely and successfully used model to yield a variety of simple solutions for both steady-state and time-dependent excitation [27, 36]. Let us consider homogeneous disorder medium with a finite scattering mean free path l_s. The derivation starts writing the P_N expansion of the specific intensity and considering only the P_0 and P_1 term.

$$I(\mathbf{r}, t, \mathbf{s}) \approx \frac{1}{4\pi} U(\mathbf{r}, t) + \frac{3}{4\pi} \mathbf{F}(\mathbf{r}, t) \cdot \mathbf{s}, \tag{1.113}$$

with $U(\mathbf{r}, t)$ average intensity and $\mathbf{F}(\mathbf{r}, t)$ flux density, already defined in (1.92) and (1.94) respectively. The assumption (1.113) is a good approximation for the specific intensity if the contribution of higher-order spherical harmonics is negligible, which is usually verified when the diffused light, after a high number of scattering events, is scattered almost uniformly in every direction, but not exactly isotropically, as otherwise $F(\mathbf{r}, t)$=0. This is a small, but fundamental contribution to have effective transport. Slightly "unbalancing" the transport along a privileged direction $\mathbf{s}$, corresponds to the case $U(\mathbf{r}, t) \gg 3/(4\pi) F(\mathbf{r}, t)\dot{s}$, depicted in Figure 1.2. Inserting (1.113) in the RTE in (1.110), multiplying by $\mathbf{s}$ and integrating over the solid angles, it is possible to obtain after some manipulations the following expression

$$\left(\frac{1}{v} \frac{\partial}{\partial t} + \left(\mu_a + \mu_s' \right) \right) \mathbf{F}(\mathbf{r}, t) + \frac{\boldsymbol{\nabla} U(\mathbf{r}, t)}{3} = 0. \tag{1.114}$$

A second equation can be obtained integrating the RTE with a source term over the solid angle

$$\frac{1}{v}\frac{\partial}{\partial t}\int_{\Omega} I(\mathbf{r},t,\mathbf{s})\,\mathrm{d}\Omega + \nabla\int_{\Omega}\mathbf{s}\cdot I(\mathbf{r},t,\mathbf{s})\,\mathrm{d}\Omega + \mu_{tot}\int_{\Omega} I(\mathbf{r},t,\mathbf{s})\,\mathrm{d}\Omega \tag{1.115}$$

$$-\mu_{tot}\int_{\Omega',\Omega} I(\mathbf{r},t,\mathbf{s}')p(\mathbf{s},\mathbf{s}')\,\mathrm{d}\Omega'\,\mathrm{d}\Omega = \int_{\Omega} q(\mathbf{r},t,\mathbf{s})\,\mathrm{d}\Omega\,. \tag{1.116}$$

where the source energy density is

$$Q(\mathbf{r},t) = \int_{\Omega} q(\mathbf{r},t,\mathbf{s})\,\mathrm{d}\Omega\,. \tag{1.117}$$

The fourth term of (1.116), representing the energy gain due to the scattering from any direction $\mathbf{s}'$ into $\mathbf{s}$, can be expressed in terms of average intensity $U(\mathbf{r},t)$:

$$\mu_{tot}\int_{\Omega',\Omega} I(\mathbf{r},t,\mathbf{s}')p(\mathbf{s},\mathbf{s}')\,\mathrm{d}\Omega'\,\mathrm{d}\Omega = \mu_{tot}U(\mathbf{r},t)\int_{\Omega'} p(\mathbf{s},\mathbf{s}')\,\mathrm{d}\Omega' = \mu_s U(\mathbf{r},t). \tag{1.118}$$

Exploiting this identity, using the normalization of the phase function (1.78) and the definition for the average intensity (1.92) and flux density (1.94), we can write

$$\frac{1}{v}\frac{\partial}{\partial t}U(\mathbf{r},t) + \nabla\mathbf{F}(\mathbf{r},t) + \mu_{tot}U(\mathbf{r},t) - \mu_{tot}U(\mathbf{r},t) = Q(\mathbf{r},t) \tag{1.119}$$

$$\rightarrow \frac{1}{v}\frac{\partial}{\partial t}U(\mathbf{r},t) + \nabla\mathbf{F}(\mathbf{r},t) + \mu_a U(\mathbf{r},t) = Q(\mathbf{r},t) \tag{1.120}$$

At this stage a second assumption is introduced, consisting of neglecting the time variation of the diffused flux $F(\mathbf{r},t)$ over a time range l_s'/v, assuming that it is much smaller than the vector itself

$$\frac{1}{\mu_s' v}\left|\frac{\partial\mathbf{F}(\mathbf{r},t)}{\partial t}\right| \ll |\mathbf{F}(\mathbf{r},t)|. \tag{1.121}$$

Neglecting the absorption[6] in the medium we can use (1.121) to rewrite (1.114) and (1.120) as

$$\mathbf{F}(\mathbf{r},t) = -\frac{1}{v}D\nabla U(\mathbf{r},t) \tag{1.122}$$

$$\frac{1}{v}\frac{\partial}{\partial t}U(\mathbf{r},t) + \nabla\mathbf{F}(\mathbf{r},t) = Q(\mathbf{r},t) \tag{1.123}$$

where D is the diffusion coefficient defined as

$$D = \frac{v}{3\mu_s'}, \tag{1.124}$$

[6] Neglecting absorption does not lead to a lack of generality. Exploting the RTE property (1.112), it is possible to decouple the absorption from the average intensity to derive the DE in the case of a non-absorbing medium. Absoption term can than be added at a later stage [27, 37].

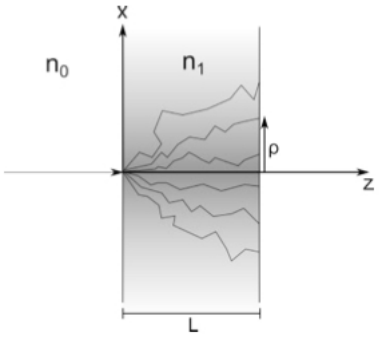

Fig. 1.3: Geometry of the slab configuration. The slab is infinite in the x and y directions. The geometry has a cylindrical symmetry around the z-axis, where ρ represents the radial coordinate. Grey lines represent schematically light propagation inside the slab.

independent of absorption. This allows to treat a posteriori the dependence on absorption in accordance with the RTE without the additional approximations intrinsic to the diffusion framework. The diffusion equation for the homogeneous medium can be now computed inserting (1.122) into (1.123), obtaining

$$\frac{1}{v}\left(\frac{\partial}{\partial t} - D\nabla^2\right) U(\mathbf{r},t) = Q(\mathbf{r},t). \tag{1.125}$$

The solution in the case of an unbounded medium with a point source is an expanding Gaussian profile

$$U(\mathbf{r},t) = \frac{vE_0}{(4\pi Dt)^{3/2}} \exp\left(\frac{r^2}{4Dt}\right), \tag{1.126}$$

that can be extended to the case of an homogeneous absorbing medium simply through (1.112), obtaining

$$U(\mathbf{r},t) = \frac{vE_0}{(4\pi Dt)^{3/2}} \exp\left(\frac{r^2}{4Dt} - \mu_a vt\right). \tag{1.127}$$

1.3.1 DE solution with slab boundary condition

The expression (1.126) represents a solution of the DE in an infinite size medium. In many problems where the light source is in proximity of the system surface or when the bulk approximation is not valid, it is necessary to define boundary conditions considering the presence of an interface, without violating the assumption done to retrieve the DE. The method described now, considers the derivation of proper solutions for slab geometry systems, useful for the interpretation of diffusive transport analysis of the systems studied in this work in chapters 5 and 4. The slab geometry presents infinite size along a plane, chosen as the x-y plane, and a finite size along its perpendicular direction,

thus along the z axis (Figure 1.3). The source is considered as a point source inside the slab. Assuming no refractive index mismatch between the interior of the system and the outer space, there should be no light entering the medium from outside, condition expressed by

$$I(\mathbf{r}, t, \mathbf{s}) = 0 \tag{1.128}$$

where $\mathbf{r}$ is indicates the position on the slab surface Σ and $\mathbf{s}$ the inward unit vector. However this boundary condition violates the assumption of the DE derivation, as P_1 requires a non isotropic angular distribution of the specific intensity (Figure 1.2). It is thus necessary to set proper boundary condition through further assumptions. The simplest approximation is called *zero boundary condition* (ZBC), that requires a vanishing inward flux

$$\mathbf{F}_-(\mathbf{r}, \mathbf{q}) = \int_{\mathbf{s}\cdot\mathbf{q}>0} I(\mathbf{r}, t, \mathbf{s})(\mathbf{s}\cdot\mathbf{q})\,\mathrm{d}\Omega = 0. \tag{1.129}$$

with $\mathbf{r}$ describing a position on the Σ surface and $\mathbf{q}$ unit vector normal to Σ. However this approximation is valid only for high optical thickness OT (ratio of the thickness L and the scattering mean free path l_s), where the average intensity close to the slab surface is several order of magnitude smaller than the one in proximity of the source. Anyway, as the ZBC allows to formulate the problem in a simple mathematical way, several studies have been performed to extend its validity also to optically thin systems (low OT), leading to define another type of boundary condition, where the physical thickness of the sample is substituted by a fictitious value: the *extrapolated bounday condition* (EBC) [38, 39, 40]. Considering a slab of size L, with interfaces at $z = 0$ and $z = L$, it is possible to define the extrapolated length z_e through the condition

$$\left[U \mp z_e \frac{\partial U}{\partial z}\right]_{z=0,L} = 0 \tag{1.130}$$

that consists in the assumption that the average intensity vanishes at a distance z_e from the slab interfaces along the direction perpendicular to them (see Figure 1.4). Mapping the system of thickness L in another with thickness $L_e = L + 2z_e$, expression (1.129) is satisfied and, together with (1.130), can be used to obtain

$$z_e = \frac{2D}{v} = \frac{2}{3} l_s, \tag{1.131}$$

that shows how the extrapolation length is related to the scattering mean free path.
So far no refractive index constant have been taken into account, assuming no mismatch on the slab surfaces. Considering a different refractive index between the sample and the environment, it is necessary to consider internal reflection at the interfaces that needs to be modeled in the transport description. This can be done adapting the boundary condition and adding the contribute of the inwards flux due to internal reflection [41]:

$$\int_{\mathbf{s}\cdot\mathbf{q}>0} I(\mathbf{r}, t, \mathbf{s})(\mathbf{s}\cdot\mathbf{q})\,\mathrm{d}\Omega = \int_{\mathbf{s}\cdot\mathbf{q}<0} R(\mathbf{s}) I(\mathbf{r}, t, \mathbf{s})|\mathbf{s}\cdot\mathbf{q}|\,\mathrm{d}\Omega \tag{1.132}$$

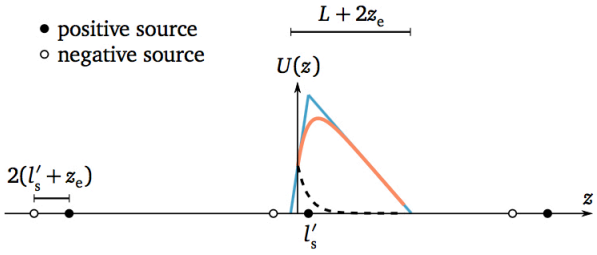

Fig. 1.4: Extrapolated boundary condition for a slab geometry with virtual point sources: the average intensity vanishes at a distance z_e from the slab interfaces.

with $\mathbf{r}$ on the interface Σ and $R(\mathbf{s})$ Fresnel coefficient for unpolarized light

$$R(\mathbf{s}) = \frac{1}{2}\left[\left(\frac{n\cos\theta_i - \cos\theta_t}{n\cos\theta_i + \cos\theta_t}\right)^2 + \left(\frac{\cos\theta_i - n\cos\theta_t}{\cos\theta_i + n\cos\theta_t}\right)^2\right]. \tag{1.133}$$

In (1.133), n rappresents the ratio between the slab refractive index and the one of the environment, θ_i is the angle between the incident radiation direction and the unit vector $\mathbf{q}$ perpendicular to the interface Σ ($\cos\theta_i = -\mathbf{s}\cdot\mathbf{q}$), and θ_t is the refraction angle. Applying the P_1 approximation (1.113), the following condition valid for $\mathbf{r} \in \Sigma$ can be retrieved

$$U(\mathbf{r}, t) + \frac{A}{2\pi}\mathbf{F}(\mathbf{r}, t)\cdot\mathbf{q} = 0, \tag{1.134}$$

where the coefficient A is defined as

$$A = \frac{1 + 3\int_0^{2\pi} R(\sigma_i)\cos^2\theta_i \sin\theta_i \,\mathrm{d}\theta_i}{1 + 2\int_0^{2\pi} R(\sigma_i)\cos_i^{\theta}\sin\theta_i \,\mathrm{d}\theta_i}. \tag{1.135}$$

and, eventually, a new value for the extrapolation length is obtained [38, 39]. Although the analytical expression of A is rather complex, it has been shown [27] that it can be approximated by the polynomial

$$\begin{aligned} A = {} & 504.332889 - 2641.00214n + 5923.699064n^2 - 7376.355814n^3 \\ & + 5507.53041n^4 - 2463.357945n^5 + 610.956547n^6 - 64.8047n^7, \end{aligned} \tag{1.136}$$

where $1< n <1.6$.

1.3.2 Steady state and time resolved solutions of DE in a slab

The boundary conditions described in the previous section will now be used to derive the solution of the DE for the slab geometry, sketched in Figure 1.3. A pencil beam propagating along the z-axis, mathematically described in the derivation as a Dirac δ function in space and time, impinges on the slab surface in $z = 0$. In agreement with the assumption on the source terms applied in the DE derivation, we consider that after

a distance l_t inside the medium, light is completely randomised and isotropic. Therefore the computation are performed assuming an isotropic point source at a depth $z = l_t$. In this way a systematic error at small optical thickness is introduced, but, like it has been demonstrated, it becomes negligble in optically thick systems [42]. The extrapolated boundary conditions cannot be satisfied with only one point source, but considering an infinite number of alternating positive and negative sources (equivalent to the one inside the medium) in an infinite diffusing medium (Figure 1.4). The sources are placed in:

$$z_{+,m} = 2m(L + 2z_e) + l_t \tag{1.137}$$
$$z_{-,m} = 2m(L + 2z_e) - 2z_e - l_t \tag{1.138}$$

With $m = 0, \pm1, \pm2, \pm3, ...$ The average diffuse intensity, that for the the symmetry of the slab does not depend on x and y separately, can be written as

$$U(\rho, \mathbf{z}, t) = U_+(\rho, \mathbf{z}, t) + U_-(\rho, \mathbf{z}, t) \tag{1.139}$$

where ρ is the radial distance from the z-axis and $U_+(\rho, \mathbf{z}, t)$ and $U_-(\rho, \mathbf{z}, t)$ are the average density contributes from the positive and negative sources respectively. The diffusion equation can be solved obtaining:

$$U_+(\rho, \mathbf{z}, t) = \frac{1}{4\pi} \frac{v \exp\left(-\mu_a v t - \dfrac{\rho^2}{4Dt}\right)}{(4\pi Dt)^{3/2}} \sum_{m=-\infty}^{+\infty} \exp\left(-\frac{(z - z_{+,m})^2}{4Dt}\right) \tag{1.140}$$

$$U_-(\rho, \mathbf{z}, t) = -\frac{1}{4\pi} \frac{v \exp\left(-\mu_a v t - \dfrac{\rho^2}{4Dt}\right)}{(4\pi Dt)^{3/2}} \sum_{m=-\infty}^{+\infty} \exp\left(-\frac{(z - z_{-,m})^2}{4Dt}\right) \tag{1.141}$$

The transmission T is calculated by the diffuse flux on the exit surface ($z = L$):

$$T(\rho, t) = -\mathbf{q} \cdot \mathbf{F}(z = L, \rho, t) = -4\pi D \frac{\partial}{\partial z} U(z = L, \rho, t), \tag{1.142}$$

from which we obtain

$$T(\rho, t) = \frac{v \exp\left(-\mu_a v t - \dfrac{\rho^2}{4Dt}\right)}{2\,(4\pi Dt)^{3/2}\, t^{5/2}} \sum_{m=-\infty}^{+\infty} \left[z_{1,m} \exp\left(\frac{-z_{1,m}^2}{4Dt}\right) - z_{2,m} \exp\left(\frac{-z_{2,m}^2}{4Dt}\right) \right] \tag{1.143}$$

with

$$\begin{aligned} z_{1,m} &= L(1 - 2m) - 4mz_e - l_t \\ z_{2,m} &= L(1 - 2m) - (4m - 2)z_e + l_t \end{aligned} \tag{1.144}$$

$T(\rho, t)$ represents the probability, per unit area and time, that a walker exits from the surface in $z = L$ at a time t and at a distance ρ from the z-axis (Figure 1.5). The series in (1.143) is an infinite series that for many applications need to be truncated

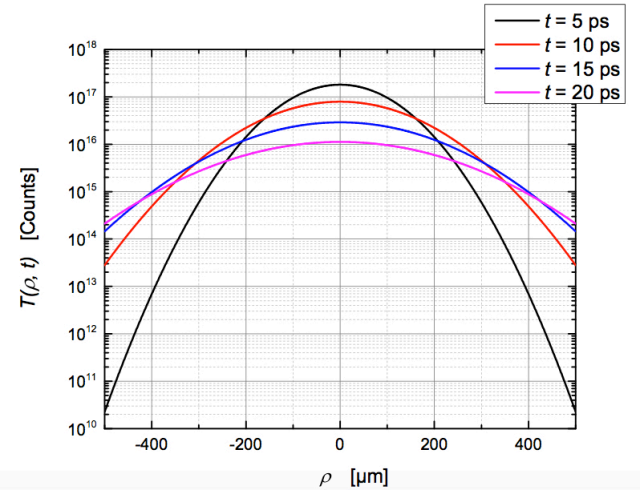

Fig. 1.5: Rappresentation of the light intenisty transmitted through a non-absorbing ($\mu_a = 0$) slab $T(\rho, t)$ as a function of the distance from the z-axis at different values of t. The slab thickness considered is $L = 200\ \mu m$ For smaller t, the light transmitted correspond to a lower number of scattering events and thus the light less deflected from the direction z-axis. At higher t the light trapped for a larger time interval inside the sample which undergone to a higher number of scattering events display a non negligble intensity also at larger ρ.

at a finite value of m. Since each virtual source is associated to a specific m index, an increase of m corresponds to an increase of the distance from the system boundary of the corresponding source. The contribution of sources associated to high index values is thus expected to be significant only for large values of ρ and or t. Considering a non-absorbing ($\mu_a = 0$) slab with $\mu_s' = 0.5\ mm$, $n = 1.4$ and $L = 40\ mm$, it has been show that truncating the series at m=10 is possible to obtain values of $T(\rho, t)$ with a truncation error within 0.1%, in a range of three orders of magnitude from the maximum value [27]. The error decreases when μ_a, L or μ_s' is increased. Integrating (1.143) over the outward surface we obtain the time resolved total transmission through the slab:

$$T(t) = \frac{\exp\left(-\mu_a v t\right)}{2\left(4\pi D t\right)^{1/2} t^{3/2}} \sum_{m=-\infty}^{+\infty} \left[z_{1,m} \exp\left(\frac{-z_{1,m}^2}{4Dt}\right) - z_{2,m} \exp\left(\frac{-z_{2,m}^2}{4Dt}\right) \right], \quad (1.145)$$

which behaviour is illustrated in the left graph of Figure (1.6). It is evident from the graph how the function exhibit, after a peak of ballistic light at small t, an exponential decay related to a specific transport quantity, the *Heisenberg time*

$$\tau = \frac{(L + 2z_e)^2}{\pi^2 D}, \quad (1.146)$$

representing the average lifetime of the diffusive process throught the slab. Again, it worths to stress the fact that, despite the absorption is taked into account, also at this stage of the derivation we could have derived $T(\rho, t)$ and $T(t)$ without absorption, reintroducing it at the end of the calculations exploting (1.112). The meaning of (1.146)

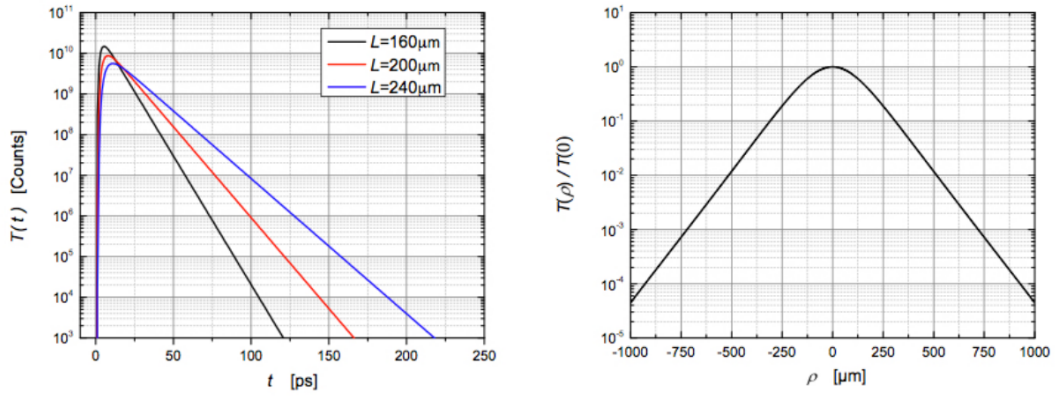

Fig. 1.6: On the left: Time-resolved transmission profile in diffusion approximation (1.145) for varying thickness. Increasing the thickness and keeping constant the l_t of the system, the optical thickness increase, and the light is trapped more efficiency inside the slab, statement justify by the fact that the larger is the thickness the more are the photons exiting the slab at larger t.

is clearer considering another method for the derivation of $T(t)$, consisting in computing the eigenmodes expansion of the diffusion equation [43]. This method leads to an expression equivalent to (1.145), but particularly suitable for understanding the long time asymptotic behaviour of the transmission[7]:

$$T(t) = -\frac{-2D\pi}{(L+2z_e)^2} \times \sum_{m=-\infty}^{+\infty} m \left[\sin\left(m\pi \frac{L+2z_e+l_t}{L+2z_e} \right) - \sin\left(m\pi \frac{L-l_t}{L+2z_e} \right) \right] \exp\left(-\frac{m^2\pi^2 Dt}{(L+2z_e)^2} \right) \tag{1.147}$$

For large times ($t \gg \frac{(L+2z_e)^2}{\pi^2 D}$) only the first term significantly contributes to the sum, and the transmission decays as a single exponential $\exp(-t/\tau)$. The spatially resolved transmission is computed integrating (1.143) over the variable t:

$$T(\rho) = \frac{1}{4\pi} \sum_{m=-\infty}^{+\infty} \left[z_{1,m}(\rho^2 + z_{1,m}^2)^{-3/2} \left(1 + \sqrt{\frac{\mu_a v(\rho^2 + z_{1,m}^2)}{D}} \right) \exp\left(\sqrt{\frac{\mu_a v(\rho^2 + z_{1,m}^2)}{D}} \right) \right. \tag{1.148}$$
$$\left. z_{2,m}(\rho^2 + z_{2,m}^2)^{-3/2} \left(1 + \sqrt{\frac{\mu_a v(\rho^2 + z_{2,m}^2)}{D}} \right) \exp\left(\sqrt{\frac{\mu_a v(\rho^2 + z_{2,m}^2)}{D}} \right) \right.$$

[7] In this expression the absorption term is neglected.

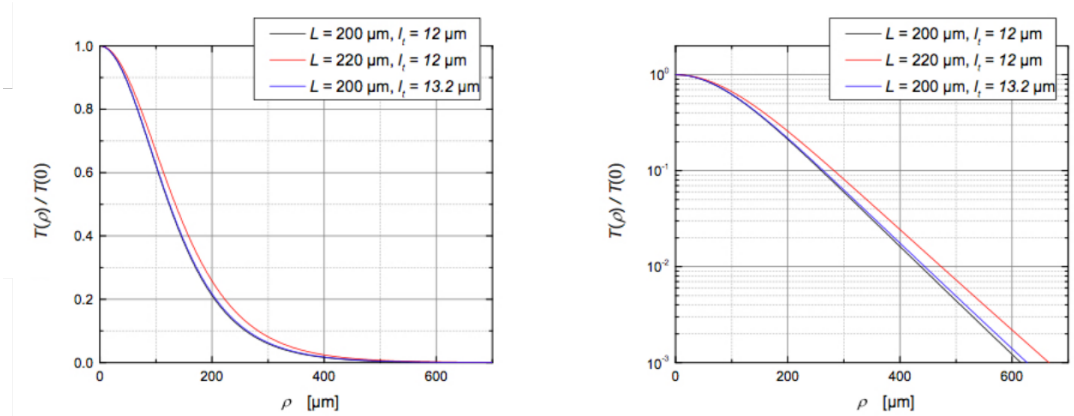

Fig. 1.7: Steady-state transmission profile in diffusion approximation (1.148) for varying thickness and transport mean free path of the 10% of the initial values. On the left, linear scale representetion. On the right, logarithmic scale representation.

that for $\mu_a = 0$, that is the case of the system studied with DE in this work, becomes

$$T(\rho) = \frac{1}{4\pi} \sum_{m=-\infty}^{+\infty} \left[z_{1,m} (\rho^2 + z_{1,m}^2)^{-3/2} - z_{2,m} (\rho^2 + z_{2,m}^2)^{-3/2} \right]. \tag{1.149}$$

The steady-state transmission profile (1.149) is represented in Figure 1.7 varying thickness and transport mean free path in both linear and logarithmic scale. A change in the 10% of the thickness strongly affects the profile, at every value of ρ. On the other hand, despite it is not observable in linear scale, also a variation of the 10% of l_t influence the function behavior. The trend can be appreciated in the logarithmic plot, in less than two order of magnitude from the maximum intensity. This means that a proper transmission measurement of the diffused profile with a continuum source, providing enough dynamic range of the detector to reveal also intensities two order of magnitude smaller than the maximum detected, gives information about the microscopic scattering quantities of the system. In the end, a well known expression for the total transmission is presented, derived integrating (1.147):

$$T = \frac{l_t + z_e}{L + 2z_e} \tag{1.150}$$

This is the *Ohm's law* for light, that expresses the total transmission through the slab in the stationary regime. In the case of optically thick systems, in the limit of $L \gg l_t$, the total transmission T scales linearly with the inverse of the thickness, $T \propto 1/L$.

1.3.3 DE in anisotropic media

In structurally anisotropic media, the transport properties are dependent by direction [44, 45, 46]. Therefore for a proper description of the diffusion process, the diffusion coefficient must be expressed as a tensor quantity [47, 48, 49, 50, 51]. Before introducing

a simple model to describe anisotropic transport, some considerations about the single scatterer asymmetry and the anisotropy of the system as a whole are required. A single scattering event by a spherical symmetric scatterer, in the Mie regime, is itself anisotropic, as the scattering cross section is commonly strongly peaked in the forward direction. Anyway, the single scattering process depends only on the relative angle between incident and scattered waves, meaning that there is no previledged direction, i.e. the collective scattering properties are in principles not anisotropic. A condition in which anisotropic transport can occur in an isotropic particles system is when the scatterers show direction dependent spatial correlations (in other words when the average distance between scatterers is different along different directions). this is not the scatterer shape that determines anisotropic transport but their distribution. In fact, a system with anisotropic shaped scatterers, like cylinders, where the scattering cross section depends on the relative orientation of the particle with respect to the direction of the incident wave, can exhibit isotropic transport, occurring if the particles are randomly oriented. However, when the collection of anisotropic scatterers exhibits a certain orientation order (for example nematic liquid crystals [52, 53, 54]), i.e when the particles are statistically aligned, the diffusion of light becomes anisotropic (Figure 1.11). The most common approach to anisotropic diffusion is replacing the diffusion constant $D = vl_t/3$ with a diffusion tensor $\mathbf{D}$. From this starting point many solutions for the diffusion equation have been proposed; here we present the solutions proposed by Kienle et al. [55]. We consider the same slab geometry analysed for the isotropic case (see subsection 1.3.2, Figure 1.3), infinite in the xy-plane and with a finite thickness L along the z-axis. We assume that in the sample coordinate system both the diffusion tensor and the corresponding transport mean free path tensor are diagonalized:

$$\mathbf{D} = \begin{vmatrix} D_x & 0 & 0 \\ 0 & D_y & 0 \\ 0 & 0 & D_z \end{vmatrix} \tag{1.151}$$

$$\mathbf{l}_t = \begin{vmatrix} l_{t,x} & 0 & 0 \\ 0 & l_{t,y} & 0 \\ 0 & 0 & l_{t,z} \end{vmatrix} \tag{1.152}$$

Therefore the isotropic diffusion equation (1.125) is replaced considering the diffusion tensor:

$$\frac{1}{v}\left(\frac{\partial}{\partial t} - \nabla \cdot \mathbf{D}\nabla\right) U(\mathbf{r}, t) = Q(\mathbf{r}, t). \tag{1.153}$$

The time and spatially resolved solution for the transmission through the slab, considering an isotropic point source $\delta(x)\delta(y)\delta(z - l_{t,z})\delta(t)$, is given by:

$$T(x, y, t) = \frac{1}{2\,(4\pi t)^{3/2}\, t^{5/2}} \frac{1}{\sqrt{D'_x D'_y D'_z}} \exp\left(-\frac{x^2}{4D'_x vt} - \frac{y^2}{4D'_y vt}\right) \times$$
$$\sum_{m=-\infty}^{\infty} \left[(L - z_{1,m}) \exp\left(-\frac{(L - z_{1,m})^2}{4D'_z vt}\right) - (L - z_{2,m}) \exp\left(-\frac{(L - z_{2,m})^2}{4D'_z vt}\right)\right] \tag{1.154}$$

where $z_{1,m} = 2mt + 4mz_e + l_{t,z}$, $z_{2,m} = 2mt + (4m-2)z_e - l_{t,z}$, $z_e = (2/3)Al_{t,z}$, and we assume a direct relationship between the diffusion tensor and the transport mean free path, $D_i = D'_i v = 1/3\ l_{t,i}\ v$. The stationary spatially resolved transmission is obtained integrating (1.154) over t:

$$T(x,y) = \frac{1}{4\pi\sqrt{D'_x D'_y D'_z}} \times \sum_{n=-\infty}^{\infty} \left((t - z_{1,m}) \left(\frac{x^2}{D'_x} + \frac{y^2}{D'_y} + \frac{(t-z_{1,m})^2}{D'_z} \right)^{3/2} - (t - z_{2,m}) \left(\frac{x^2}{D'_x} + \frac{y^2}{D'_y} + \frac{(t-z_{2,m})^2}{D'_z} \right)^{3/2} \right) \tag{1.155}$$

Integrating (1.155) over x and y, we obtain the time resolved total transmission, which is equivalent to (1.145) provided that D is substituted by the $\mathbf{D}$ tensor components, and the photon lifetime is given by:

$$\tau = \frac{(L + 2z_e)^2}{\pi^2 D_z}. \tag{1.156}$$

In this respect it is important to note that in the slab geometry the time resolved total transmission depends on the transport properties along the z-axis, and the effect of the anisotropy modifies the transport properties on the plane orthogonal to z. This is quite intuitive thinking that the unique leaky channel is along z. Similarly, the static total transmission, depending only on $l_{t,z}$, is obtained:

$$T = \frac{l_{t,z} + z_e}{(L + 2z_e)}. \tag{1.157}$$

To conlude, it worth to mention how anisotropic diffusion theory in describing anisotropic light transport represents a very actively debated topic both from the theoretical and the experimental point of view [56, 57, 58, 59]. In particular the author of [58] has recently pointed out that the relationship between the diffusion tensor elements and the underlying transport mean free paths should be corrected by some unknown factor with respect to the usual, isotropic simple formula. Therefore, to date, an accurate quantitative study of the microscopic transport properties inside anisotropic systems should be possible only through inverse Monte Carlo simulations. Nevertheless, in the context of the theoretical and experimental work on anisotropic systems presented in the thesis (see Chapter 4.3.1 and 5.3.3), the corrections described in [58] would hardly affect the results obtained.

References

[1] E. W. M- Born. *Principles of Optics: Electromagnetic Theory of Propagation, Interference and Diffraction of Light*. 1970.

[2] E. M. Purcell and C. R. Pennypacker. "Scattering and absorption of light by nonspherical dielectric grains". In: *Astrophys Journal* 186 (1973), pp. 705–714.

[3] B. T. Draine. "The discrete-dipole approximation and its application to interstellar graphite grains". In: *Astrophys Journal* 333 (1988), pp. 848–872.

[4] H. DeVoe. "Optical properties of molecular aggregates. I. Classical model of electronic absorption and refraction". In: *J. Chem. Phys.* 41 (1964), pp. 393–400.

[5] S. B. Singham and C. F. Bohren. "Light scattering by an arbitrary particle: a physical reformulation of the coupled-dipoles method". In: *Optics Letters* 12 (1987), pp. 10–12.

[6] B. T. Draine and P. J. Flatau. "Discrete-dipole approximation for scattering calculations". In: *J. Opt. Soc. Am. A* 11.4 (1994).

[7] A. Lagendijk and B. A. V. Tiggelen. "Resonant multiple scattering of light". In: *Physics Reports* 270 (1996), pp. 143–215.

[8] B. A. van Tiggelen, A. Lagendijk, and A. Tip. "Multiple-scattering effects for the propagation of light in 3D slabs". In: *Journal of Physics: Condensed Matter* 2.37 (1990), p. 7653.

[9] M. B. van der Mark, M. P. van Albada, and A. Lagendijk. "Resonant multiple scattering of light". In: *Phys. Rev. B* 37 (1988), p. 3755.

[10] J. Jackson. *Classical electrodynamics*. Wiley, 1999.

[11] M. Rusek and A. Orlowsky. "Analytical approach to localization of electromagnetic waves in two-dimensional random media". In: *Physical Review E* 51.4 (1995), R2763–R2766.

[12] M. Rusek, A. Orlowsky, and J. Mostowsky. "Localization of light in three-dimensional random dielectric media". In: *Physical Review E* 53.4 (1996), pp. 4122–4130.

[13] M. Rusek, A. Orlowsky, and J. Mostowsky. "Band of localized electromagnetic waves in random arrays of dielectric cylinders". In: *Physical Review E* 56.4 (1997), p. 022704.

[14] M. Rusek, J. Mostowsky, and A. Orlowsky. "Random Green matrices: From proximity resonances to Anderson localization". In: *Physical Review A* 61 (1999), p. 022704.

[15] A. Ishimaru. *Wave Propagation and Scattering in Random Media, Vol. 1*. Academic Press, New York, 1978.

[16] G. C. Papanicolaou and R. Burridge. "Transport equations for the Stokes parameters from Maxwell's equations in a random medium". In: *Journal of Mathematical Physics* 16 (1975), p. 2074.

[17] K. H. D. L. Tsang J. A. Kong. *Scattering of electromagnetic waves, Vol. 1*. John-Wiley, New York, 2000.

[18] M. I. Mishchenko. "Vector radiative transfer equation for arbitrarily shaped and arbitrarily oriented particles: a microphysical derivation from statistical electromagnetics". In: *Applied Optics* 41 (2002), pp. 7114–7134.

[19] M. I. Mishchenko. "Microphysical approach to polarized radiative transfer: Extension to the case of an external observation point". In: *Applied Optics* 42 (2003), pp. 4963–4967.

[20] J. Rippoll. "Derivation of the scalar radiative transfer equation from energy conservation of Maxwell's equations in the far field". In: *Journal of the Optical Society of America A* 28 (2011), pp. 1765–1775.

[21] L. G. Henyey and J. L. Greenstein. "Diffuse radiation in the galaxy". In: *The Astrophysical Journal* 93 (1941), pp. 70–83.

[22] H. C. V. de Hulst. *Multiple light scattering: tables, formulas, and applications*. Elsevier, 2012.

[23] R. Graaff et al. "Similarity relations for anisotropic scattering in absorbing media". In: *Optical Engineering* 32 (1993), pp. 244–252.

[24] S. Chandrasekhar. *Radiative transfer*. R. Courier Corporation, 2013.

[25] M. I. Mishchenko, L. D. Travis, and A. A. Lacis. *Multiple scattering of light by particles: radiative transfer and coherent backscattering*. Cambridge University Press, 2006.

[26] D. R. Wyman, M. S. Patterson, and B. C. Wilson. "Similarity relations for the interaction parameters in radiation transport". In: *Applied Optics* 28 (1989), pp. 5243–5249.

[27] D. Contini, F. Martelli, and G. S. Zaccanti. "Photon migration through a turbid slab described by a model based on diffusion approximation. I. Theory". In: *Applied Optics* 36 (1997), pp. 4587–4599.

[28] K. Vynck, R. Pierrat, and R. Carminati. "Multiple scattering of polarized light in disordered media exhibiting short-range structural correlations". In: *Physical Review A* 94 (2016), p. 033851.

[29] L. Roux et al. "Scattering by a slab containing randomly located cylinders: comparison between radiative transfer and electromagnetic simulation". In: *Journal of the Optical Society of America A* 18 (2001), pp. 374–384.

[30] S. Fraden and G. Maret. "Multiple light scattering from concentrated, interacting suspensions." In: *Physical Review Letters* 65 (1990), p. 512.

[31] L. Bressel and O. Reich. "Theoretical and experimental study of the diffuse transmission of light through highly concentrated absorbing and scattering materials: Part I: Monte Carlo simulations." In: *Journal of Quantitative Spectroscopy and Radiative Transfer* 146 (2014), pp. 190–198.

[32] B. Wilson and G. Adam. "A Monte Carlo model for the absorption and flux distributions of light in tissue." In: *Medical Physics* 10 (1983), pp. 824–830.

[33] L. Wang, S. Jacques, and L. Zheng. "MCML—Monte Carlo modeling of light transport in multi-layered tissues." In: *Computer Methods and Programs in Biomedicine* 47 (1995), pp. 131–146.

[34] E. Alerstam, T. Svensson, and S. Andersson-Engels. "Parallel computing with graphics processing units for high-speed Monte Carlo simulation of photon migration." In: *Journal of Biomedical Optics* 13 (2008), pp. 060504–060504.

[35] F. Martelli et al. *Light Propagation through Biological Tissue and Other Diffusive Media: Theory, Solutions and Software*. SPIE Press, Bellingham, 2010.

[36] M. S. Patterson, B. Chance, and B. Wilson. "Time resolved reflectance and transmittance for the noninvasive measurement of tissue optical properties." In: *Applied Optics* 28 (1989), pp. 2331–2336.

[37] R. Pierrat, J.-J. Greffet, and R. Carminati. "Photon diffusion coefficient in scattering and absorbing media." In: *Journal of the Optical Society of America A* 23.5 (2006), pp. 1106–1110.

[38] M. Patterson et al. "Diffusion representation of photon migration in tissue." In: *IEEE Microwave Theory and Techniques Symposium Digest, Institute of Electrical and Electronics Engineers, New York* BB-1 (1991), pp. 905–908.

[39] R. C. Haskell et al. "Boundary conditions for the diffusion equation in radiative transfer." In: *Journal of the Optical Society of America A* 11.10 (1994), pp. 2727–2741.

[40] J. J. Duderstadt and L. J. Hamilton. *Nuclear reactor analysis.* John Wiley and Sons, Inc., New York, 1976.

[41] M. Keijzer, W. M. Star, and P. R. M. Storchi. "Optical diffusion in layered media". In: *Applied Optics* 27 (1988), pp. 1820–1824.

[42] T. J. Farrell, M. S. Patterson, and B. Wilson. "A diffusion theory model of spatially resolved, steady-state diffuse reflectance for the noninvasive determination of tissue optical properties invivo." In: *Medical Physics* 19.4 (1992), pp. 879–888.

[43] T. J. Huisman. *Faster than diffusive light. Temporal behavior of superdiffusive light.* Internship Thesis, LENS - European Laboratory for Non-Linear Spectroscopy., 2011.

[44] T. Binzoni et al. "Anisotropic photon migration in human skeletal muscle." In: *Physics in Medicine and Biology* 51.5 (2006), N79.

[45] E. Simon, P. Krauter, and A. Kienle. "Time-resolved measurements of the optical properties of fibrous media using the anisotropic diffusion equation." In: *Journal of Biomedical Optics* 19.7 (2014), pp. 075006–075006.

[46] D. S. Wiersma et al. "Time-resolved experiments on light diffusion in anisotropic random media." In: *Physical Review E* 62.5 (2000), p. 6681.

[47] A. Kienle et al. "Light propagation in dentin: influence of microstructure on anisotropy." In: *Physics in Medicine and Biology* 48.2 (2003), N7.

[48] B. P. J. Bret and A. Lagendijk. "Anisotropic enhanced backscattering induced by anisotropic diffusion." In: *Physical Review E* 70.3 (2004), p. 036601.

[49] R. Sapienza et al. "Anisotropic weak localization of light." In: *Physical Review Letters* 92.3 (2004), p. 033903.

[50] P. M. Johnson, S. Faez, and A. Lagendijk. "Full characterization of anisotropic diffuse light." In: *Optics Express* 16.10 (2008), pp. 7435–7446.

[51] P. M. Johnson et al. "Anisotropic diffusion of light in a strongly scattering material". In: *Physical Review Letters* 89.24 (2002), p. 243901.

[52] D. S. Wiersma et al. "Time-resolved anisotropic multiple light scattering in nematic liquid crystals." In: *Physical Review Letters* 83.21 (1999), p. 4321.

[53] M. H. Kao et al. "Observation of light diffusion and correlation transport in nematic liquid crystals." In: *Physical Review Letters* 77.11 (1996), p. 2233.

[54] B. V. Tiggelen and H. Stark. "Nematic liquid crystals as a new challenge for radiative transfer." In: *Reviews of Modern Physics* 72.4 (2000), p. 1017.

[55] A. Kienle, F. Foschum, and A. Hohmann. "Light propagation in structural anisotropic media in the steady-state and time domains." In: *Physics in Medicine and Biology* 58.17 (2013), p. 6205.

[56] E. Alerstam, T. Svensson, and S. Andersson-Engels. "Parallel computing with graphics processing units for high-speed Monte Carlo simulation of photon migration." In: *Journal of Biomedical Optics* 13.6 (2008), pp. 060504–060504.

[57] A. Kienle. "Anisotropic light diffusion: an oxymoron?" In: *Physical Review Letters* 98.21 (2007), p. 218104.

[58] E. Alerstam. "Anisotropic diffusive transport: connecting microscopic scattering and macroscopic transport properties." In: *Physical Review E* 89.6 (2014), p. 063202.

[59] P. M. Johnson and A. Lagendijk. "Optical anisotropic diffusion: new model systems and theoretical modeling." In: *Journal of Biomedical Optics* 14.5 (2009), pp. 054036–054036.

CHAPTER 2

Optical resonances in fractal structures: coexistance of extended and localized modes

Since the pioneering work of Mandelbrot on fractal geometry, demonstrating how fractality can in many cases model a wide range of phenomena in our world, many scientists from many different fields have been fascinated by the extremely peculiar characters of fractal systems. Investigating from a theoretical and experimental point of view how the self-similarity characterizing a fractal can influence the physics and the statistics of different systems have lead to increadibly interesting results, also in the field of optics. To take further our understanding of the optical behavior of a scale-invariant system we performed a study of light propagation in 2D fractal distributed point scatterers systems, investigating the electromgnetic field resonances, approach that allowed to analyze important coherent optical phenomena in the field of random media optics. This work does not represent only a progress in our knowledge of light transport in fractals but it gives more insight also in the study of resonances in disorder media in general, so far mostly focused on uniform disorder scatterers distribution. In this chapter, after an introduction on fractality and electric field mode resonances, a study of mode size properties in fractals is presented, showing how, contrary to homogeneous disordered system, a coexistance of modes of every size occurs.

2.1 Resonances of optical random media: Homogeneous disorder Vs Fractal disorder

Wave transport description of light propagation is a fundamental approach required to understand many coherent optical phenomena occurring in disordered photonic media. A basic concept arising from this description is the concept of natural resonances of an

optical medium, i.e. the set of supported electromagnetic modes of the structure, real solutions of the wave equation for an ideal closed and non-absorbing system. However, many photonics systems exhibit losses by radiation or absorption that need to be taken into account. Open systems are non-Hermitian and the natural resonances, called Quasinormal Modes (QNM) [1, 2, 3, 4, 5], are complex valued frequencies with imaginary part related to the leakage rate. A modal approach consisting in determining the QNM of the system and reconstruct from them its optical response, it has already been applied to study coherence effect in random optical structures like Anderson localization [6, 7, 8], random lasing [9, 10, 11] and Purcell enhancement [12, 13] in disordered media cavities, phenomena where the mode size and spectral distribution strongly affect the whole system optical behaviour. The most common model of disorder employed to develop a theoretical study of resonances in random media is the statistically homogeneous disorder, characterized by a uniform probability to find a scattering center in the system spatial region. In 2D disordered systems, it is expected to find, depending on the system density and size, modes with a comparable size, either strongly localized or quasi-extended [14, 15, 16] . Here we show how the modes of a 2D random system could have a completely different size distribution, with coexistence of localized and extended modes, if the scattering centers of the system are arranged according to a fractal geometry. This result does not only reveal the extremely peculiar optical properties of fractals but it stress the impact of spatial correlations on light modes in complex systems in general. In fact coexistance of localized and extended modes has recently been demonstrated with a similar approach also for deterministic aperiodic optical structures [17, 18].
It worths to mention that studies concerning the modes size in fractal arrangements of scattering particles have been an hot-topic during the nineties, when much effort has been put to model the plasmonic resonances of inhomogeneous metallic nanoparticles aggregates [19, 20, 21]. In fact, in the most common thin-film fabrication procedures, the growth process depends strongly by the surface morphology and the growing interfaces evolve into self-similar fractal forms [22]. As a consequence the surface roughness has been often modeled as self-affine system, i.e. self-similar 2D structures whose elements are characterized by a different scaling along the x and y directions[23, 24, 25]. The modeling led to tackle the problem in terms of QNM analysis in this system, with a mathematical approach very similar to the one used in this work [26, 20, 27]. Despite many similarities there are also several important differences between these previous work and the one presented here, that will be presented in section 2.3.2.

2.2 Coupled dipole formalism

The study of the resonances in finite size fractal systems has been performed modeling the scattering object as an ensamble of coupled electric dipoles and studying their collective excitations. This approach, also known as Coulped Dipole method (CDM), represent a robust approximation deeply used in the analysis of the scattering properties of collection of particles and single scattering centers with arbitrary distribution and shape [28, 29, 30, 31, 32]. Mapping the scattering objects as an array of electric dipoles, the optical response of the investigated system can be retrieved adapting the scattering properties of the single dipoles to the specific problem and computing the response of the whole array. In this work the CDM has been implemented in the point-scatterers

approximation, neglecting thus the shape of the single scattering object and subsituting it with a single electric dipole with resonant frequency ω_0 and resonance width Γ_0. Properly dipole scattering cross section have been chosen in order to provide a realistic description of the scattering process. Moreover, the strong resonant scatterer condition $\omega_0 \gg \Gamma_0$ have been required. This approach provides meaningful results not only in the case of wavelength bigger than the average scattering centers size but also, as it has already been observed in previous studied, when the wavelength of the propating field is comparable to the size of the scattering particle [33, 34, 35]. In this way the retrieved results have general validity for the description of QNM in open media made of strongly resonant scatterers.
We recall now the classical electrodynamics derivation from Maxwell equations of the electric field mode supported by an ensamble of dipoles, described in details in section 1.1.2. Starting from Maxwell equation in the integral form

$$\mathbf{E}(\mathbf{r}) = \mathbf{E}_0(\mathbf{r}) + \boldsymbol{\nabla} \times \boldsymbol{\nabla} \times \int d\mathbf{r}' \mathbf{P}(\mathbf{r}) \frac{e^{ik_0|\mathbf{r}-\mathbf{r}'|}}{|\mathbf{r}-\mathbf{r}'|}. \tag{2.1}$$

with incident monochromatic light $\mathbf{E}_0(\mathbf{r}, t) = E_0(x, y)e^{-i\omega_0 t}\hat{e}_z$, and assuming the medium as an ensamble of N point-like dipole with polarizability $\mathbf{P}(\mathbf{r}, t) = P(x, y)e^{-i\omega_0 t}\hat{e}_z$ with

$$P(x, y) = \sum_{a=1}^{N} p_a \delta_2(x - x_a, y - y_a), \tag{2.2}$$

it is possible to obtain a system of N linear equations

$$E'_a(\boldsymbol{\rho_a}) = E_0(\rho_\mathbf{a}) + \frac{1}{2i} \sum_{b=1}^{N} G_{a,b}(e^{i\phi_b} - 1)E'_b(\boldsymbol{\rho_b}) \qquad a = 1, ..., N \tag{2.3}$$

with $G_{a,b}$ 2D Green function, which solutions for vanishing incident fields, i.e. the eigenvectors of the Green function, represent the modes of the system. It is important to point out that in order to perform a reliable description of a general scattering system, with scattering particles size smaller or comparable to the wavelength, the point-scatterer approximation requires a representation for the scatterers that fulfills the optical theorem, that lead to the following expression for the coupling between the single dipole and the field

$$i\pi k_0^2 |\mathbf{p_a}| = \frac{e^{i\phi_a} - 1}{2} \mathbf{E}'(\boldsymbol{\rho_a}). \tag{2.4}$$

The complex polarizability phase is frequency dependent $\phi_a = \phi_a(k)$, assumed to be the same for all the system dipoles $\phi_a = \phi$. A further step now needed in the analysis consists in providing a physical interpretation of the eigenvalues of the Green matrix.

2.2.1 Eigenvalues interpretation: modes of the ensamble

A key feature of the model is the assumption on the dipoles scattering features, that require $\omega_0 >> \Gamma_0$, i.e. the scatterers are strongly resonant. In this frame it is possible to

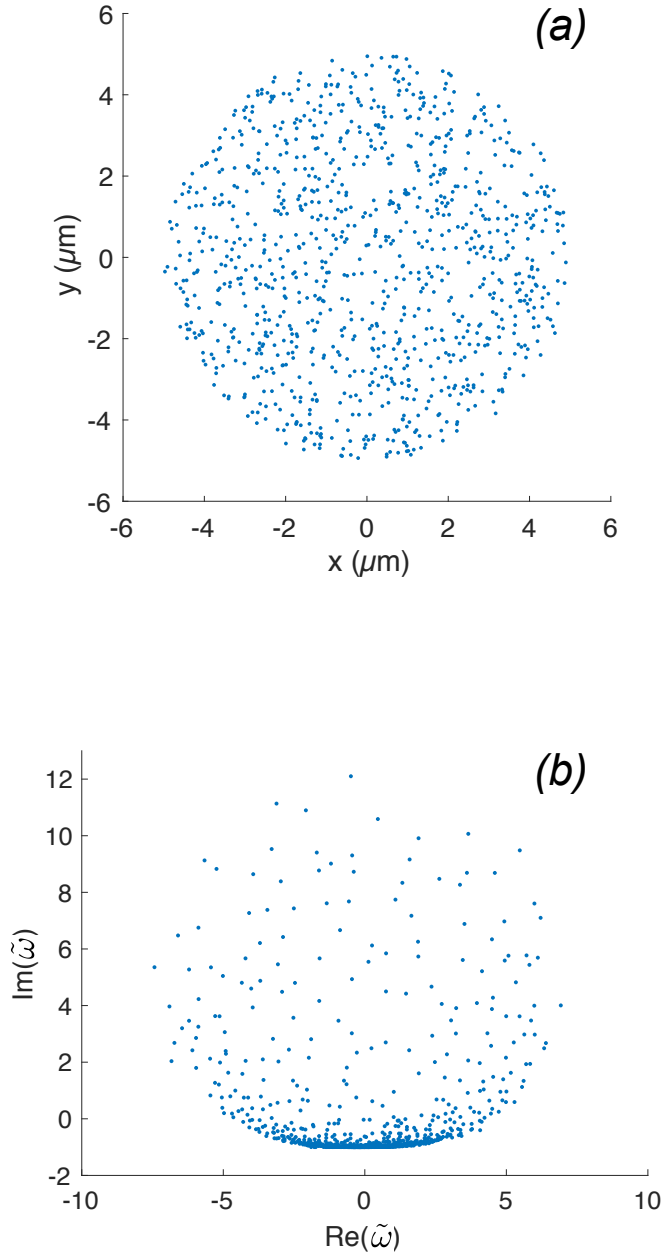

Fig. 2.1: *a*) Random distribution of 1024 dipoles inside a circle of radius 5 µm. *b*) Eigenvalues of the system depicted in (*a*).

describe the dipoles as Breit-Wigner scatterers and give a specific physical interpretation to the eigenvalues of the matrix [36, 6, 7, 37]. It is evident form (1.38) that the eigenvalues $\lambda_G(k)$ satisfy

$$\lambda_G(k) = \frac{2i}{(e^{i\phi(k)} - 1)} = \cot\delta(k) - i \tag{2.5}$$

where $\delta(k) = \phi(k)/2$. This relation holds for both the 2D and the 3D cases. As the Green matrix and its eigenvalues explicitly depend on the frequency, the problem is non-linear and analytical solutions can be retrieved only in specific cases. One of them is to assume that the scattering from the dipole is Breit-Wigner-type. For this purpose, performing the following series expansion of $\cot\delta$ near the resonance frequency ω_0 one gets

$$\cot\delta(\omega) \approx (\cot\delta(\omega))_{\omega=\omega_0} + \left(\frac{d\cot\delta(\omega)}{d\omega}\right)_{\omega=\omega_0} (\omega - \omega_0) + ... \tag{2.6}$$

Then we formulate the first-order term in the following way

$$\left(\frac{d\cot\delta(\omega)}{d\omega}\right) = \left(\frac{d\cot\delta(\omega)}{d\delta(\omega)}\frac{d\delta(\omega)}{d\omega}\right) = -\csc\delta(\omega)\frac{d\delta(\omega)}{d\omega}, \tag{2.7}$$

and we assume that the phase shift at the resonance is $\delta(\omega_0) = \frac{\pi}{2}$ and $\left(\frac{d\delta(\omega)}{d\omega}\right)_{\omega=\omega_0} = \frac{1}{\Gamma_0}$ (where Γ_0 is the spectral width of the dipole resonance). The expansion (2.6) becomes then

$$\cot\delta(\omega) \approx -\frac{\omega - \omega_0}{\Gamma_0}. \tag{2.8}$$

It is now possible to write the Green matrix eigenvalues as a function of frequency using (2.5) and (2.8), obtaining

$$\lambda_G(\omega) = -\frac{\omega - \omega_0}{\Gamma_0} - i. \tag{2.9}$$

The resonance complex frequencies $\tilde{\omega} = Re(\tilde{\omega}) + iIm(\tilde{\omega})$ can be formulated in terms of Green matrix eigenvalues, allowing to write the following iterative equation

$$\tilde{\omega} = \omega_0 - \Gamma_0(\lambda_G(\tilde{\omega}) + i). \tag{2.10}$$

Using now the strongly resonant scatterers assumption $\omega_0 \gg \Gamma_0$, it is possible to approximate (2.10) to

$$\tilde{\omega} \approx \omega_0 - \Gamma_0(\lambda_G(\omega_0) + i), \tag{2.11}$$

expression revealing the physical meaning of the eigenvalues. Real and imaginary part of each complex eigenvalue are directly related to the relative eigenvector (i.e. the relative

mode) frequency ($Re(\tilde{\omega})$) and spectral width ($Im(\tilde{\omega})$), both normalized to Γ_0, namely

$$Re(\tilde{\omega}) \approx \omega_0 - \Gamma_0 Re(\lambda_G(\omega_0)), \qquad Im(\tilde{\omega}) \approx \Gamma_0(1 - Im(\lambda_G(\omega_0))). \tag{2.12}$$

A representation of the complex plane resonances distribution for a 2D homogeneous disordered system and the relative dipole distribution are depicted in Figure 2.1. The dipole ensemble considered is made of $N = 1024$ dipoles distributed in a random fashion inside a circle of radius $R = 5\,\mu m$. The dipole resonance wavelength is set to the value $\lambda_0 = 0.6\,\mu m$, meaning that the number of scattering particles per square wavelength is $\rho\lambda^2$=4.7. A usefull quantity that can be now retrieved to get insights on the modes degree of localization is the Inverse Partecipation Ratio (IPR), quantity exploited to discriminate eigenvalues corresponding to extended and localized modes. Once the eigenvalue problem (2.5) is solved, i.e. the N Green Matrix eigenvalues $\{\lambda_G(\omega)_n\}_{n=1,\dots,N}$ are computed, the electric field values, i.e. the eigenvectors $\mathbf{E}_n = \{E_n(\mathbf{r}_i)\}_{i=1,\dots,N}$ at each dipole position $\{\mathbf{r}_i\}_{i=1,\dots,N}$, are known and they can be use to compute the IPR of each $\mathbf{E}_n$ through

$$IPR_n = \frac{\sum_{i=1}^{N} |E_n(\mathbf{r}_i)^4|}{\left(\sum_{i=1}^{N} |E_n(\mathbf{r}_i)^2|\right)^2}. \tag{2.13}$$

The inverse of the IPR is the Mode Spatial Extent (MSE) and it corresponds to the number of scattering centers in the region occupied by the electromagentic field $\mathbf{E}_n$. In Figure 2.2, the eigenvalues complex plane relative to two systems with the same number of particles and different size is reported. Color scale represents the modes IPR. Both the graphs show the distributions with adimensional frequency $(\omega - \omega_0)/\Gamma_0$ (i.e. $Re(\tilde{\omega})$) along the x-axis, and adimensional width $\delta\omega/\Gamma_0$ (i.e. $1 + Im(\tilde{\omega})$) along the y-axis, obtained from equations (2.12). Since now on we will refer to modes adimensional frequency and adimensional width respectively as frequency and width. The eigenmodes in Figure 2.2*a* are the logarithmic scale representation of the Figure 2.1b with colorbar, corresponding to a system with $N = 1024$ dipoles and size $R = 5\,\mu m$, while the the eigenvalue distribution in 2.2b) corresponds to a system with the same number of particles but smaller radius, $R = 3\,\mu m$. This means that the system in b has a higher density and thus, as the dipoles are distributed homogeneously on the system surface, a higher scattering strength $k_0 l$. As it is well known from the theories of diffusion and localization of light in random systems, the higher is the scattering strength of the system the higher is the number of localized mode generated by the interference of the scattered waves propagating in the medium [6, 38]. This is an evident feature also in the QNM distribution in the pictures, displaying how the higher scattering strength in the system leads to the formation of modes in *b* with high IPR, i.e. with small MSE, that are not present in *a*. These modes are indicated by a yellowish color of the color bar scale. The more localized exhibits higher lifetimes and thus narrow frequency width, as expected for open system modes. A detailed description of the MSE distributions as a function of the QNM frequency is provided in Figure 2.3. Again, the distributions reported correspond to system with $N = 1024$ dipoles and different radius (R = 1, 3, 6, 10 µm), with colorbar representing the modes width. It is possible to see how increasing the system scattering strength leads to the formation of modes localized on a lower number of scattering centers, like it has been already stated from the analysis of

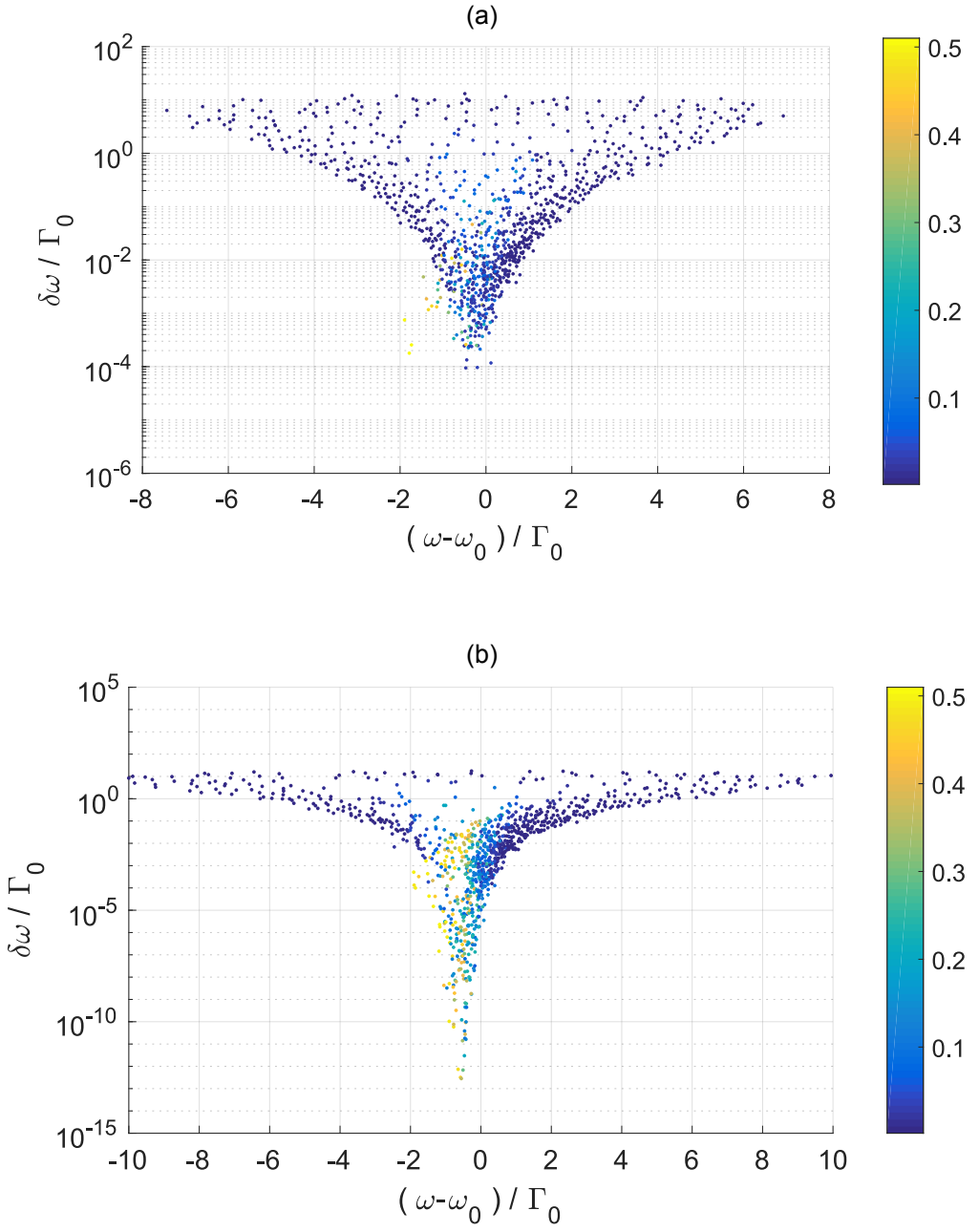

Fig. 2.2: QNM mode distribution plotted as a function of frequency and width. The color bar represents the modes IPR. *a*) QNM distribution for a system with $N = 1024$ dipoles inside a circle of radius $R = 5\,\mu\text{m}$. *b*) QNM distribution of a system with $N = 1024$ dipoles inside a circle of radius $R = 3\,\mu\text{m}$. The higher scattering strength of the system leads to the formation of QNM with higher IPR, i.e. more localized. Moreover these localized modes, as they are in the complex plane region corresponding to spectrally narrow (small δ/Γ_0) resonances, exhibits a higher lifetime.

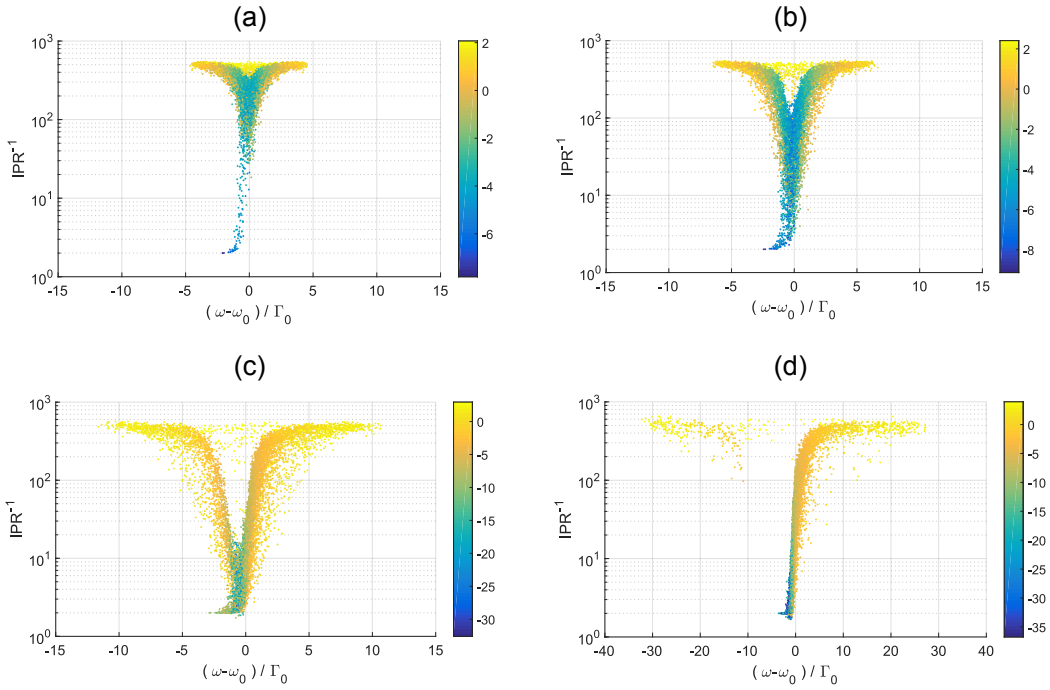

Fig. 2.3: *a*) IPR^{-1} Vs adimensional frequency of the QNM of a system with $N = 1024$ dipoles inside a circle of radius $R = 10\,\mu\mathrm{m}$. *b*) $R = 6\,\mu\mathrm{m}$. *c*) $R = 3\,\mu\mathrm{m}$. *d*) $R = 1\,\mu\mathrm{m}$.

Figure 2.2, most of them at small detuning from ω_0. An important feature that worth to point out is the particular "V-shaped" profile reached at $R = 3\,\mu\mathrm{m}$ (Figure 2.2c), consisting in a depletion of the graph region corresponding to high MSE and frequencies close to ω_0. Increasing further the scattering strength, reaching a radius comparable with the dipoles resonant wavelength, the frequency interval [-10,0] becomes populated of almost only localized states (Figure 2.3d). Once the eigenvalue problem (1.38) is solved, the eigenvectors allow, computing the dipole moments p_a in equation (1.35) and considering the expression (1.37), to determine each mode field distribution anywhere in space through

$$E'(\rho) = E_0(\rho) + \sum_{a=1}^{N} i\pi H_0^{(1)}(k_0|\rho - \rho_{\mathbf{a}}|)E'(\rho_{\mathbf{a}}). \tag{2.14}$$

In Figure 2.4, three examples of intensity distributions of modes of an homogeneous disordered system with $N = 1024$ and $R = 3\,\mu\mathrm{m}$ are reported, together with the corresponding eigenvalues representations in both the complex plane and the IPR^{-1} graph. The intensity maps have been computed defining a grid mesh of the system and retrieving with (2.14) the electric field values in each pixel. The type of mode

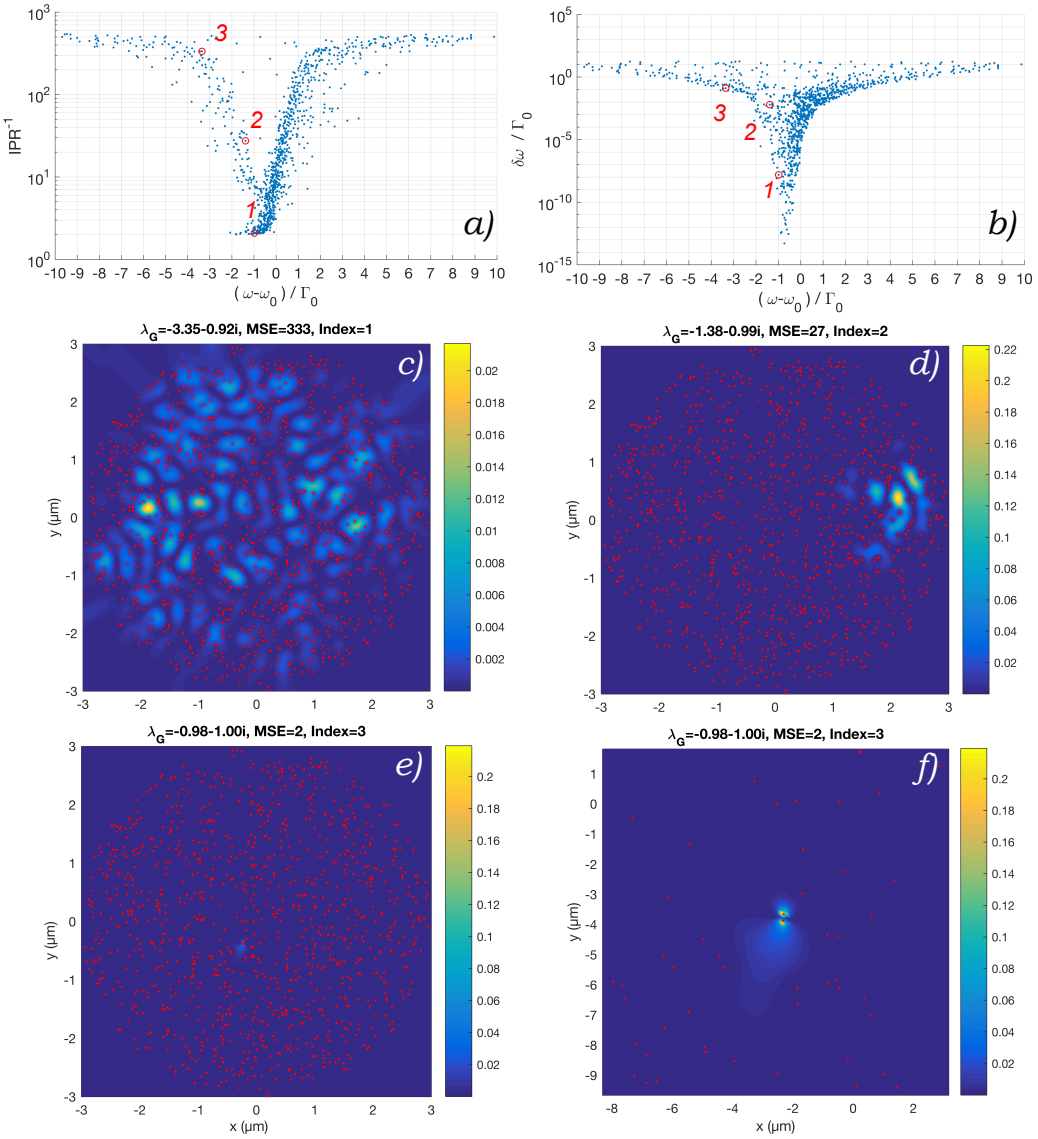

Fig. 2.4: *a*) and *b*) display the MSE distribution and the eigenvalue frequency plane of an homogenous disordered system with $N = 1024$ and $R = 3\,\mu\text{m}$. The red circles enlighten three specific modes, an extended one (3), a mode localized in a smaller area of the sample (2) and a mode confined on a couple of very close dipoles. *c*), *d*), *e*) are the modes map of (3), (2) and (1) respectively. The intensity distributions are computed with (2.14) in each point of the system corresponding to the centers of a "pixel" grid with side $\lambda/40$. *f*) insight of *e*).

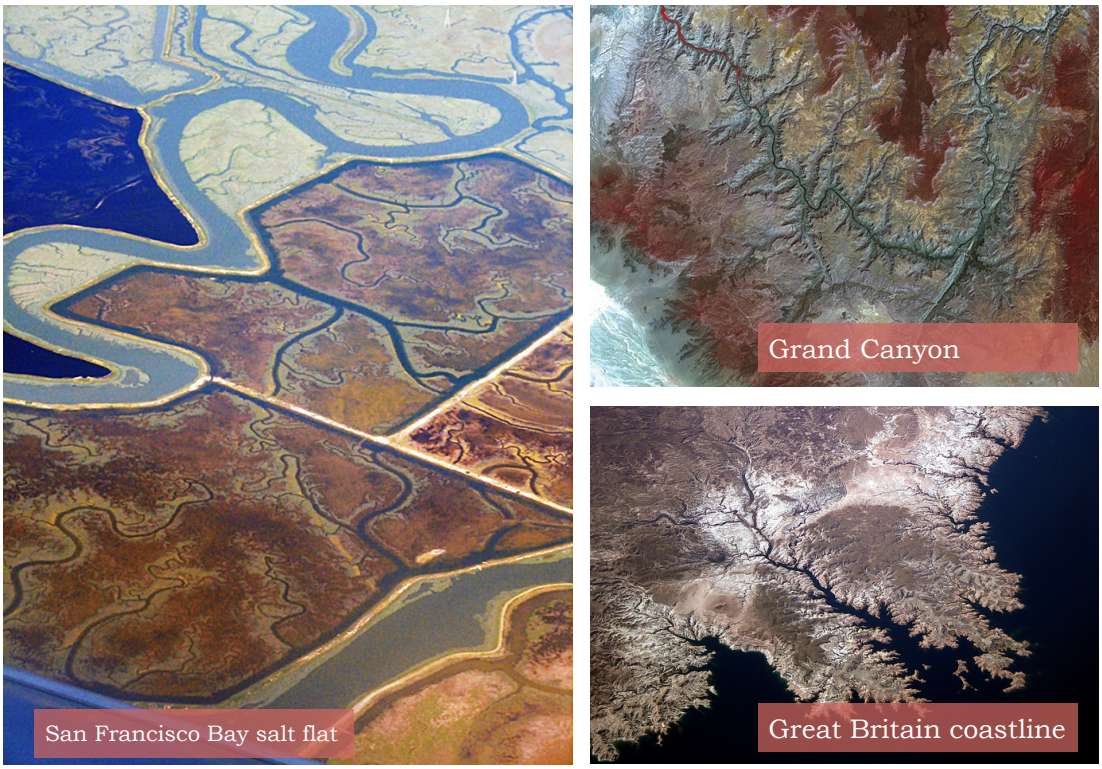

Fig. 2.5: Example of self-similar geological conformations.

localized on the pair is a "proximity resonance", a type of excitation manifesting when two scatterers are placed very closed together [39, 36].

2.3 Fractality: a brief overview

Before introducing the results obtained describing the QNM of 2D fractal systems through the coupled dipole formalism, an introduction of the general properties of fractals is presented, describing briefly some interesting optical properties arised from previous studies on fractals. Fractals are structures or objects that exhibit self-similarity properties, that is that part of the structure on smaller scale length looks like the whole. Formal mathematical treatments has been developed to describe the geometry of fractals, that can be applied also to model real systems of our world that exhibit self similarity [40]. Fractal feature can be found in territory conformation (coastlines [41], mountains [42], rivers [43, 44]), plants (leaves [45], trees branches), cells growing process [46, 47, 48], human body anatomy [49, 50, 51], and physiological processes, like the heart beat [52, 53]. Images with examples are reported in Figure 2.5 and 2.6. Fractality emerges also in stochastic processes like animal food foraging [54, 55, 56] and human travels [57, 58], described by a generalized type of random walk, the Lévy walk, characterized by an heavy tail step length distribution that ensure walk scale invariance [59, 60, 61]. The exotic spatial properties of the fractal models and their suitability to describe the statistical structural features of many system found in nature have led, as in the past till nowadays, to consider how scale invariance could affect wave transport.

A fractal distribution of voids inside a TiO_2 nanoparticles scattering matrix has been shown to lead to a Lévy walk for light (Section 2.3.1). Experimental observations and theoretical models of Lévy walk have been done also for self-similar transport of cold atoms in optical lattices [62, 63, 64] and in hot atomic vapours [65]. Fractal geometry has been also exploited to optimize antennas. The common log-periodic antennas, invented in 1958, are arrays of dipoles of different length, thus with different resonance frequency, ordered from the bigger to the smaller on a support, spaced at intervals following a logarithmic function of the frequency [66]. As opposed to this antenna arrays, single element antenna designed from self-similar shapes have been proposed in 1995, engeneered to be frequency and bandwidth invariant [67, 68, 69]. One last example of interaction between radiation and fractal geometries consists in the plasmonic resonances of inhomogeneous thin-films of metallic nanoparticles, know as supercontinuous films. Common methods of thin-film fabrication leads to the formation of rough surfaces, made of self-similar aggregates of metallic clusters. Several experimental studies on these structures reported near-field enhancement observations, like surface-enhanced Raman scattering [70, 71], and giant enhancement of nonlinear-optical responses of such clusters [72]. The localization of optical energy in small regions, denominated hot-spots [21, 73], has been intially interpreted as an Anderson localization effect. Further theoretical and experimental studies revealed how apparently the local field enhancement is a fingerprint of a mechanism called inhomogeneous localization, characteristic of the fractal. This optical effect consists in the formation of different plasmonic eigenmodes, which coexist at close frequencies and have completely different localization sizes [74, 75, 20, 25]. A detailed overview of the plasmonic resonance in this kind of system is presented in section 2.3.2.

One important concept arising from the geometrical description of fractal structures is the system fractal dimension d_f. As a rigorous mathematical treatment is beyond the scope of this section, an intuitive interpretation of d_f is here given through a popular example of fractal curve: the *Koch snowflake*. In Figure 2.7 the procedure to generate this geometry for a single side is depicted. Starting from a segment, the step 1 is performed, dividing it in 3 segments of equal length and substituting the central one with an equilateral triangle with the same side length of the segment. In each step the procedure is repeated for every segment. After each iteration, the number of sides of the whole curve increases by a factor of 4, so that after n iterations the number of sides is $3 \cdot 4^n$. In this way, starting from an equilateral triangle, after an infinite number of iterations, the Koch snowflake, illustrated for a finite number of step in the left of Fig. 2.7, is obtained. A sequence of iterations consisting in rearranging in each sub unit of the geometry a specific "generator" (in this case the segment), is the common strategy to built many ideal fractals [40]. The fundamental point is the exotic dimensionality of the curve obtained. Assuming that the length of the step 0 segment is 1, it is possible to show that the area of the Snowflake, again in the ideal case of an infinite number of iterations, is $8/5$, while its perimeter is infinite. But, as the curve itself it is a closed curve, topological dimension D is 1 and, according to euclidean geometry, it is expected to be possible to associates to it a finite length. This is a paradox that explain how the topological dimension is not a proper descriptor of the system dimensionality. The d_f is defined in a way to provide informations on the scaling properties of the curve. Considering in each step of Figure 2.7 the number of segments N and the scaling length

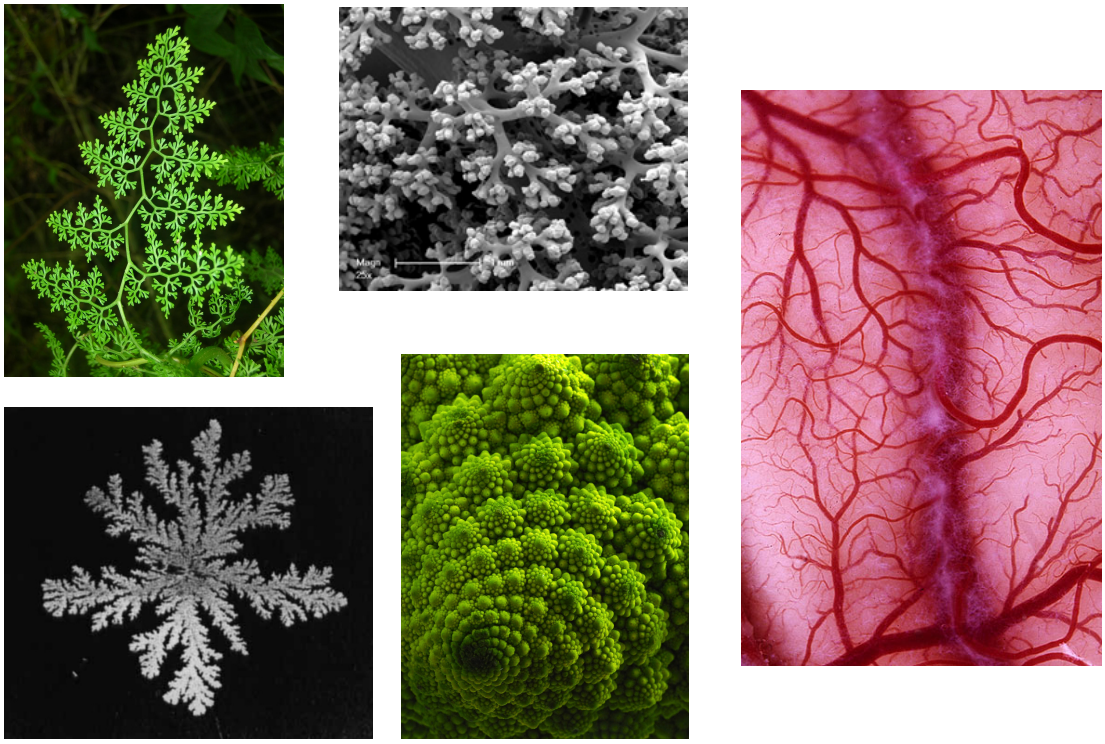

Fig. 2.6: example of fractal structures in biological systems like, plants, bacteria colonies, lung alveoli and blood veins.

factor ζ,[1] it is possible to define the scaling relation $N \propto \zeta^{-d}$. Defining from it the fractal dimension as

$$d_f = -d = \frac{\log N}{\log \zeta} \tag{2.15}$$

and applying the definition to the first iteration of the Koch curve, one obtains $d_f = \log 4/\log 3 = 1.2618$. If in each step of the process in Figure 2.7 the single segment would be divided in three segments of equal length (basically keeping dividing in each step the original segments in smaller units) then $-d$=1, meaning that, as expected from a non fractal object, the system dimension is equal to the topological one. The d_f value indicates that the Koch curve is an object with a dimensionality in between 1 and 2, i.e. that fills space more then ordinary curves but less then a surface. This peculiar space-filling properties of the geometry is a feature common to all the fractals exhibiting a fractional dimension. It must be pointed out that this definition of d_f is good for the case of the Kock curve but, for other geometries characterized by more complicated patterns, alternative definitions have been formulated to provide a proper description [40]. The d_f will be useful to perform the study of optical properties of 2D fractal point distribution in the chapter, analyzing how the electromagnetic modes can be affected by this quantity.

[1] In each step each segment length is reduced by a factor of 3.

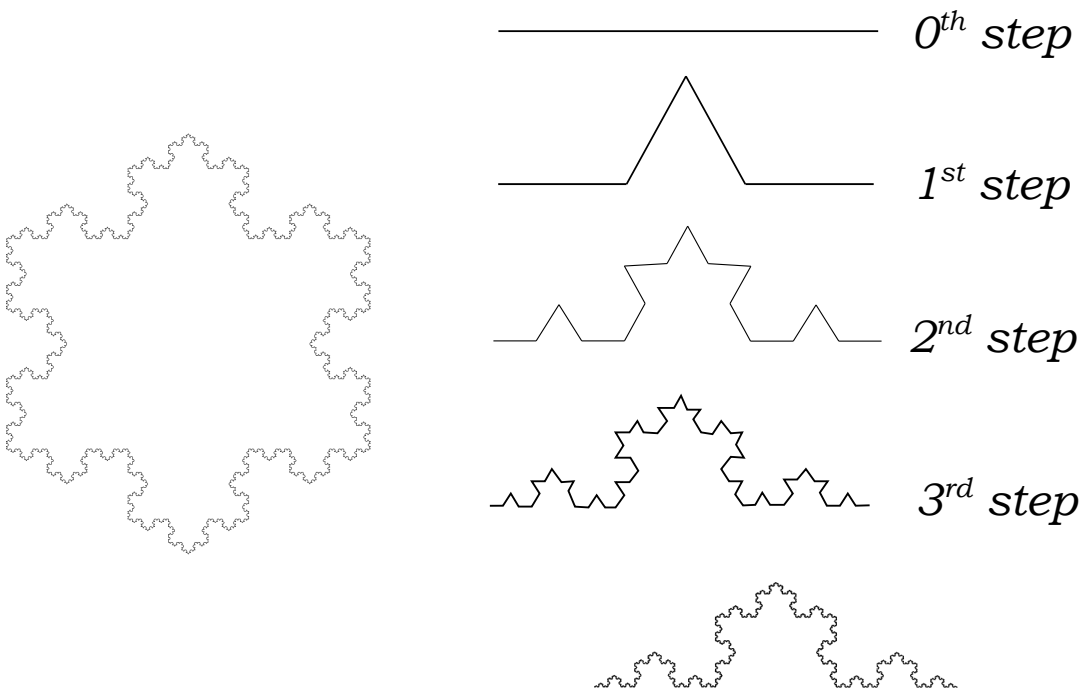

Fig. 2.7: On the left, illustration of the Koch snowflake. On the right, sequence of iterations to generate the Koch curve from an equilateral triangle. The iteration are displayed for a single side of the triangle.

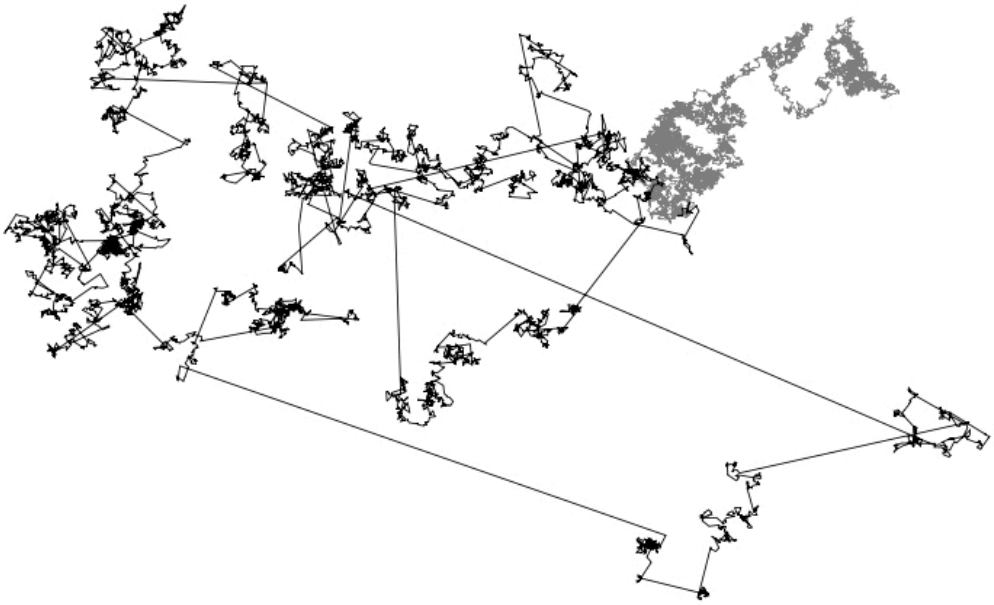

Fig. 2.8: Representation of the Lévy walk (black) with α=1.5, and the Brownian motion (grey), both after 10000 steps.

2.3.1 Lévy glasses

As already introduced in this section, the interaction of electromagnetic field with fractals has been a topic that already attracted scientists from the world of photonics. In this subsection, an experimental work that proves how self-similarity in a statistical disordered system can indeed be exploited to tailor the light random walk in a Lévy-walk with specific fractal dimension is presented. As already mentioned in section 1.2, the physics of light transport in random media is characterized by particular coherence properties that, in most of the cases, allow to neglect the wave nature of light propagation and to describe it in terms intensity diffusion. As a consequence, the transport problem can be mapped into a random walk. Assuming to deal with an homogeneous and isotropic disorder arrangement of scattering centers, the random walk for light evolves in a sequence of steps, which length is sampled by a normal distribution while its orientation is sampled uniformly in the solid angle. The random walk of this specific case is a Brownian motion. If the length of the steps is picked by an heavy tail distribution then the type of random walk obtained is completely different, as very long step acquire a non negligble probability to occurs. If the distribution is an α-stable Lévy distribution, i.e. with an asymptotic power law behaviors as $\sim |x|^{-(\alpha+1)}$ with the Lévy parameter $0 < \alpha < 2$ (note that for $\alpha < 2$ it has infinite variance), than the random walk is called Lévy walk. Example of Lévy walk and Brownian motion are compared in Figure **??**. The mean square displacement $\langle \mathbf{r}(t)^2 \rangle$ of the Lévy walk scales with time according to a power-law $\langle \mathbf{r}(t)^2 \rangle \propto t^\gamma$ (with γ scaling exponent dependent by α and also by the time distribution of the steps), thus faster than the normal diffusion process, where γ=1. This is the reason why the transport regime considered is called *superdiffusion*. Requiring

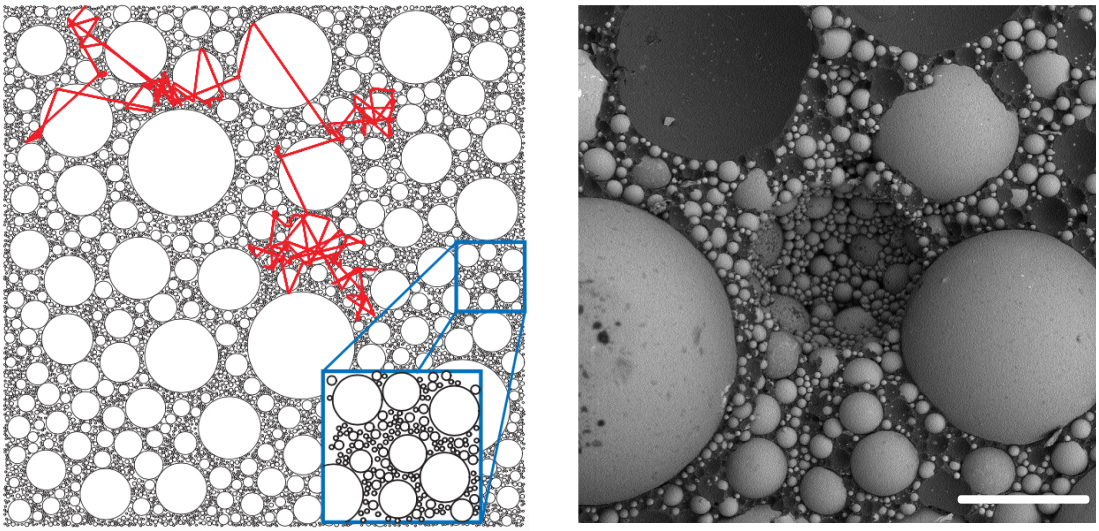

a) *b)*

Fig. 2.9: *a)* Lévy glass representation. White circles correspond to the glass spheres, thus the voids of scatterers. The grey regions are the areas with the Titanium dioxide nanoparticles, i.e. the scattering centers. The insight shows how the polydispersity of the glass sphere radius ensures in a certain length interval the self-similarity of the voids. *b)* SEM image of the Lévy glass. Scale bar $R = 100\,\mu\text{m}$.

$1 \leq \alpha < 2$ and a finite mean flight time, i.e. the average of the time required to perform the displacement of a single step is finite, it is possible to retrieve the following relation between the Lévy and the scaling parameters, $\alpha = 3 - \gamma$ [61, 60]. In references [76, 77, 78] the procedure to obtain a scattering material where light propagates in the superdiffusive regime with tunable α, that is the parameter that determine different step-length distributions, is presented. In order to engineer such material the concept of self-similarity is exploited, but instead of implementing it in the scattering particle size distribution, it is introduced in the density of scatterers. The reason behind this strategy is that different sizes would lead to different scattering processes, Mie scattering would occur for particles with size comparable to the wavelength while the scattering from particles with size much smaller than the wavelength would be Rayleight type. As the former presents a way larger cross sections than the latter, scattering would occurs mainly from the bigger particles. The adopted strategy is thus to use scattering centers with comparable size, but introducing fractally distributed region without scattering material. This has been realized fabricating samples with TiO_2 scattering nanoparticles and polydispersed glass spheres in a refractive-index matched polymer matrix. This novel scattering material have been called *Lévy glass*. In Figure 2.9 is reported a schematic representation of a 2D projection of the Lévy glass (a) and a SEM image (b) of the real sample. In the illustration on the left the white circles correspond to the glass spheres, thus the regions without scattering objects. The grey regions are the areas with the TiO_2 nanoparticles. The insight shows how the polydispersity of the glass sphere radius

ensures the self-similarity of the voids. In this way the light that propagates in the voids performs steps of a length depending by the radius of the glass sphere, while when it propagates in the gray region it undergoes to the scattering by the nanoparticles. The red line represents a possible path of the light in the system, resembling a Lévy walk. In the references, the authors show how the fractal dimension of the Lévy walk, and thus α, can be chosen tuning the distribution of diameters of the glass spheres $P_s(d)$. Ensuring a diameter distribution of the type

$$P_s(d) = \frac{1}{d^{2+a}} \tag{2.16}$$

the step length distribution takes the form $P(x) = 1/x^{a+1}$, that is the step length distribution of a Lévy walk, where $a = \alpha$, demonstrating how the scale invariance exploited to model specific random walk problems can indeed be realized in optical systems to obtain the same type of transport for light.

2.3.2 Supercontinuous films

A particular class of fractal structures already introduced at the beginning of the chapter is represented by the metallic thin-films made of fractal clusters of metallic nanoparticles, which surface-plasmon resonances have been theoretically modeled and experimentally investigated for more than 20 years. These systems are also known as supercontinuous films. The reason behind such effort is the peculiar character of the localization properties of plasmonic metal systems, where the optical energy propagates through the free electrons excitations on the metallic particle surface, that is through plasmons. On the contrary of electromagnetic waves in dielectric, where light can not be localized on less than half the wavelength, i.e. the diffraction limit, plasmons are not restricted by a characteristic wavelength and can localize the optical energy at a minimum scale of a few nanometers [79]. In fractal aggregates of plasmonic nanoparticles, this mechanism leads to the formation of hot-spots, restricted areas with huge field enhancement, initially considered as due to Anderson localization, where the fields of a plasmonic eigenmode decay exponentially in space [80]. Further theoretical work from the same author revealed a different type of localization mechanism underlying the hot-spot. Performing a plasmonic resonance analysis based on computing the dipolar spectral response of clusters, i.e. defining the cluster as en ensemble of dipoles excited by an external electric field, they retrieved the plasmonic eigenmodes of the system solving an eigenvalue problem for the frequency and the decay rate of the excitation. They found that each eigenmode may consist of a different number of sharp hot spots. These hot spots and their localization radii fluctuate strongly with the optical frequency and from cluster to cluster (Figure 2.10). For this reason they named this mechanism as inhomogeneous localization [20, 81].

This physical behavior has been claimed to be observed experimentally only in 2010 from the author of [74], that measured the statistical distribution of the local density of optical states (LDOS) in the supercontinuous films of gold covered by a thin SiO_2 layer. Depositing dielectric nanobeads containing fluorescent molecules on the surface, they excited them singularly sending a pulse with a far-field optical microscope and they measured the decay rates. Computing the normalized variance of the decay

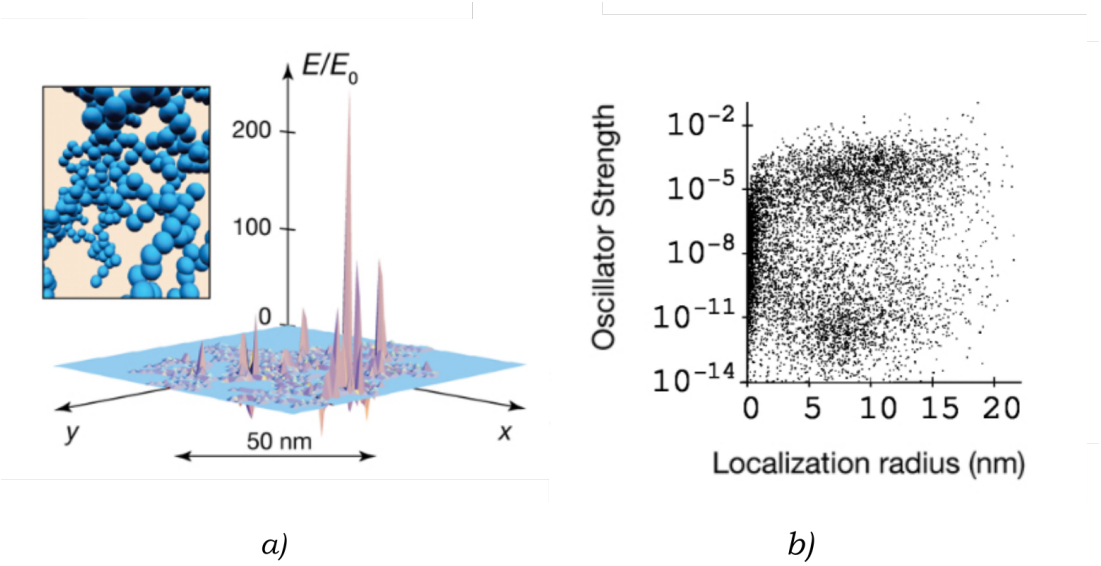

Fig. 2.10: Plamonic resonances in a supercontinuous film, adapted form [82]. (a) Hot spot of the local optical fields inside a sytem of silver nanospheres. Insert: Illustration of the cluster network (b) Plasmon eigenmodes for a semicontinuous film plotted against their oscillator strength and localization radius.

rates, assuming that the field under each individual nanobead is dominated by a single eigenmode, they retrieved the LDOS and the volume in which an eigenmode is localized [82]. Changing the density of the gold nanoparticles, moving thus from a dilute configuration to a more dense one, considered as a fractal distribution, they observed a change from low local density of optical states and weakly fluctuating local fields to a near-field enhancements, i.e. hot-spots appear. The different localization radii of each hot spots indicates that the mode volume fluctuates strongly from cluster to cluster.
The theoretical formalism and the type of investigation performed on the plasmonic resonances in supercontinuous films shows clear similarities to our approach to mode size investigation in fractals. However there are several important differences that must be discussed. First of all, the thin-film study is the attempt to understand one precise phenomenon in a specific type of system. The resonances calculations are performed using the 3D Green tensor to simulate the experiments made on the films. As already explained in section 2.2, we consider purely 2D systems, with the purpose to obtain results adaptable to any problem involving 2D distributed resonant scatterers. A second point is the type of considered resonance. In the plasmonic studies on thin-films the investigated resonances are strictly related to the optical feature of metal, affected by absorption and mostly located on the nanoparticle network. The system considered in this work is no affected by absorption so the mode computed are purely the result of multiple scattering. This means that our study describes a different type of resonances, strongly affected by the mutual arrangement of the scattering particles and suitable to understand the real impact of scale-invariance properties on the optical behavior. This is not the case of the plasmonic resonances described above, mostly affected by the proximity of the nanoparticles in the cluster and not by the structural feature of

the system as a whole. Moreover, despite the experimental work in [74] displays very interesting results exhibiting the fingerprints of inhomogeneous localization, it shows no evidences that the field fluctuations are due to the self-similarity of the film, as, according to the type of system considered, the field enhancement could in principle be linked to the heterogeneity of the nanoparticles distribution. To conclude, the model that will be analyzed in the next chapter, despite it is more ideal, allows a complete characterization of the mode size dependence by the system fractality.

2.4 Coexistance of mode size in fractal

In this section, after a description of the algorithm exploited to generate point distributions with self-similarity, the results obtained from the modal analysis in 2D fractal structures through the coupled dipole formalism are reported.

2.4.1 Soneira-Peebles algorithm

The fractal structures studied in this work have been obtained through the Soneira-Peeble algorithm [83], an algorithm designed to generate point distributions with a power-law pair correlation function. This algorithm have been originally designed to model galaxy distribution in the sky, managing to reproduce the main cluster statistics. The main parameters of the Soneira-Peebles are the three values η, L and ξ and the fractal distribution is generated in sequence of steps. The procedure starting by choosing the radius R_0 of the step-0 sphere. In the first step η spheres (step-1 spheres) with radius R/ξ, with $\xi > 1$, are placed randomly in a way that their center is inside the step-0 sphere. In the second step, again η spheres with radius R/ξ^2 are randomly placed inside each step-1 sphere. This process is repeated L times, keeping adding η spheres with smaller radius (R/ξ^i where i is the step number) inside the spheres of the previous step. In the end the centers of the η^L spheres with radius R/ξ^L of the last steps represent the point distribution. This procedure is illustrated in Figure 2.11. To get more insight in the effect of varying the three parameters η, L and ξ on the distribution, examples of simple point distributions obtained with the algorithm are reported in Fig. 2.12. For a fixed number of points, η determines the dynamic range of the resulting point distribution. The smaller is η, the higher is the number of steps required to reach a fixed number of points, while a large value of η leads to a smaller number of levels. A small value of η also results in a smaller filling fraction of space with spheres than a high value of η (1st row in Fig. 2.12). L corresponds to the total number of steps and it determines the range of densities and scales in the resulting point distribution. For a fixed value of η, L also determines the total number of points (second row in Fig. 2.12). Last, for given values of η and L, ξ determines the range of spatial scales. A value of ξ close to 1 means that the spheres of a low step number are of comparable size, while a values of ξ much larger than one means that sphere of a certain step are significantly smaller than the spheres in the preceding level (bottom row in Fig. 2.12). The most important feature of the algorithm is the possibility to tune the pair-correlation function, that can be analytical evaluated from the algorithm parameter. In fact the pair correlation

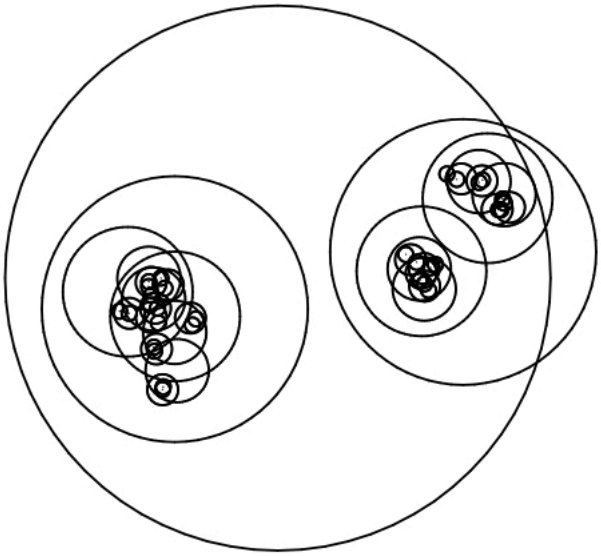

Fig. 2.11: Soneira-Peebles model. The largest circle represent the step-0 sphere. η step-1 circles are placed inside it with a radius which is smaller by a fixed factor. This process is repeated until one ends up with η^L level-L circles. At the center of these step-L circles, $N = \eta^L$ points are placed, which form the output distribution of the algorithm. Image adapted from [84].

function of the distribution depends from a factor γ by the following power law

$$g_2(r) \sim r^{-\gamma} \tag{2.17}$$

where, if D is the dimensionality of the space embedding the distribution,

$$\gamma = D - \left(\frac{\log \eta}{\log \xi}\right) \tag{2.18}$$

for $R/\xi^{L-1} < r < R$, where the log ratio corresponds to the fractal dimension of the point distribution. In this way it has been possible in the present work to generate structures with different fractal dimension to study how this quantity affects the optical modes properties.

2.4.2 2D fractal resonances

The Green matrix eigenvalue problem described in section 2.2 is here exploited to retrieve the QNM of a 2D fractal systems made of strongly resonant point scatterers with the same scattering properties. The analysis has been performed considering different fractal dimensions of the point-distributions obtained with the Soneira-Peeble algorithm. In Figure 2.13 three distributions with the same number of dipoles and varying γ are reported. In order to obtain low L configurations with significant differences at different d_f, the chosen value of η is 2. In this way, according to (2.18), the difference in the ξ of the systems, that is the scaling of the the radius at each step of the algorithm,

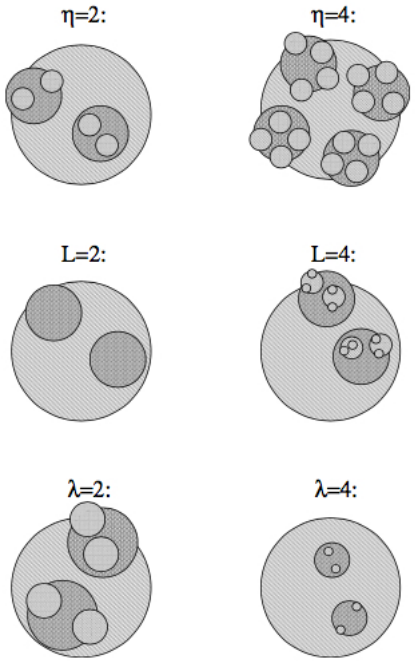

Fig. 2.12: Meaning of the three parameters η, L and ξ of the Soneira-Peebles model. The first row shows the effect of varying η, the number of circles which is placed in each circle. The second row shows the effect of varying L, the total number of steps. The last row shows the effect of varying ξ, the ratio of the radius of each circle with the radius of circles generated in the step before. Image adapted from [84].

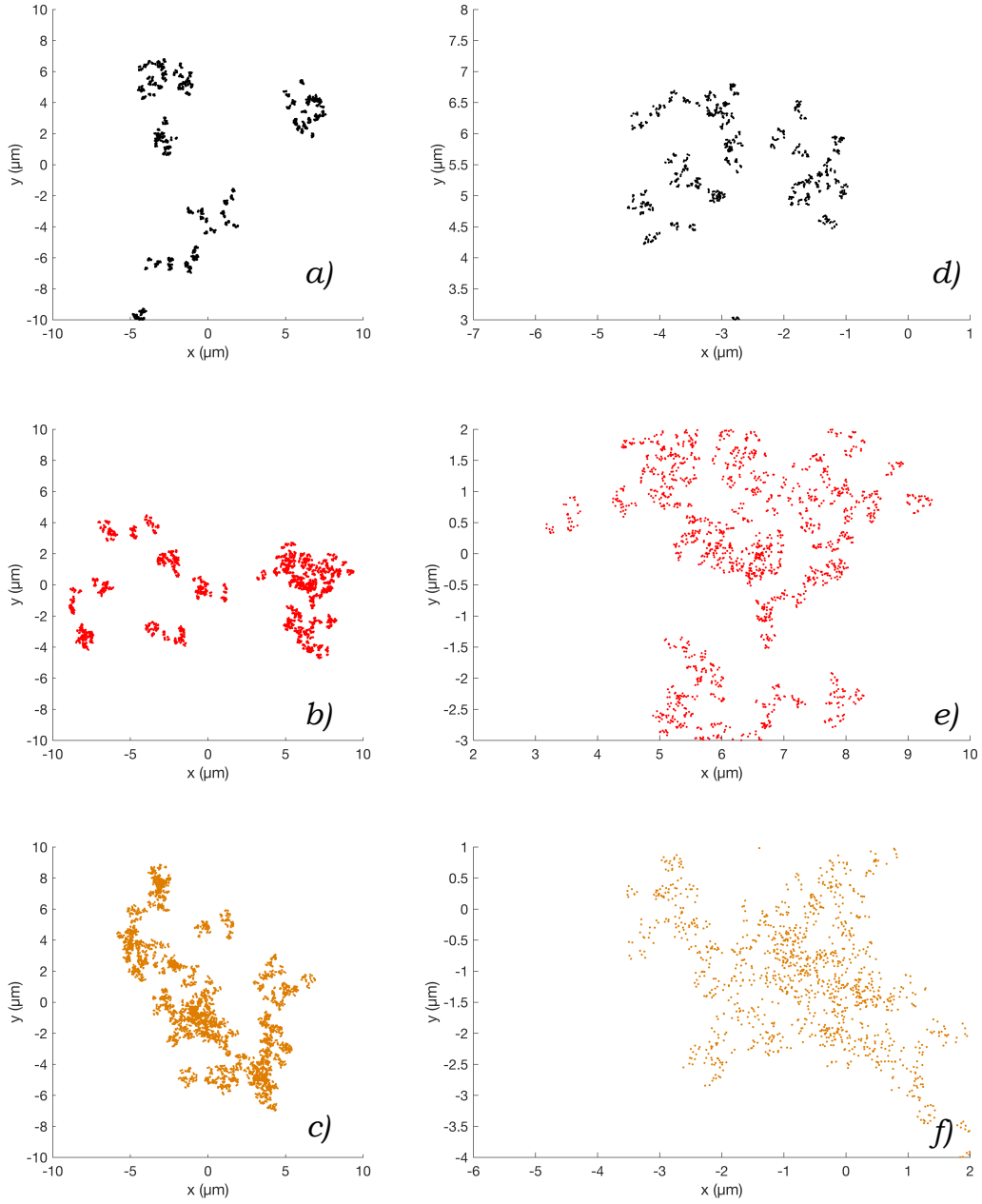

Fig. 2.13: Soneira-Peebles distributions. All the graph represent the 2D fractal structures obtained with the algorithm setting the parameters to the values η=2 and L=12, in order to get systems with N=4096 scatterers. The step-0 radius is set to R=10 µm. The ξ parameter is chosen to get fractal dimension 1.2 (a)), 1.4 (b) and 1.6 (c) respectively. d), e) and f) are the insight corresponding to a), b) and c). It is possible to see how setting a higher fractal dimension there is a higher degree of clustering of the scattering points.

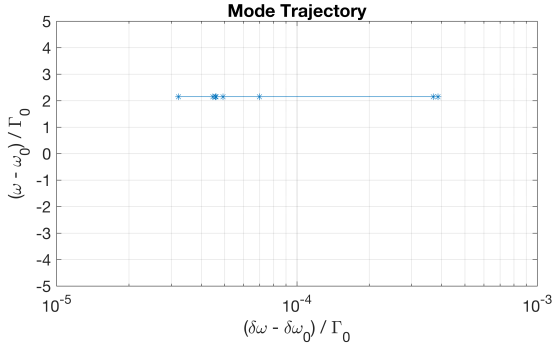

Fig. 2.14: Trajectory of a proximity resonance mode in the complex plane in a sequence of step where the surrounding scatterers, starting from those more far, are removed.

is maximized, leading to fractal point arrangements affected by their d_f values also at low algorithm steps. The Figure shows structures with d_f =1.2, 1.4 and 1.6. It is clear, looking also at the insight graph of the distributions, how the higher is the fractal dimension the more the scatterers tends to fill regions with smaller area. The eigenvalues complex plane of structures with d_f =1.2, 1.4 and 1.6 and same values η=2 and L =10 (thus a total number of particles N=1024) are reported in Figure 2.15, together with the one of a system with the same number of particles distributed homogeneously in the same area. The dipole resonance wavelength has been chosen in order to have, in the homogeneous case, $\rho\lambda^2$=13, i.e. a high scattering strength producing supported modes localized in space at a detuning from the dipole resonant frequency of of approximately Γ_0. Despite the fractals display space dependent fluctuation of $\rho\lambda^2$, they are system obtained choosing as value of the step-0 radius of the Soneira-Peeble algorithm the same of the homogeneous system, R=3 µm. The value $\rho\lambda^2$ is thus on average the same of the homogeneous case considered, allowing a proper comparison between fractality and randomness. A first difference arising from the study of the QNM distribution in this different type of disordered system is the frequency of the modes localized on a small number of dipoles, i.e. the modes with low value of log(MSE), described by the colorbar. In Figure 2.15a the tail of the high lifetime modes, and thus with small width, it is centered around a frequency approximately Γ_0 smaller than the dipole resonance one, while the fractal case exhibits localized modes with a larger negative detuning. A second feature is the lifetime of low log(MSE) state. An increase of d_f leads to the formation of a larger number of localized state but the maximum lifetime reached is low. This is evident from 2.16, where the graphs of the log(MSE) are reported as a function of frequency, that show how in the "most fractal" systems, for this specific value $\rho\lambda^2$=13, a large fraction of the modes tents to be confined on less than 10% of the system scatterers. All these feature are related to the geometry of the distributions and the different degree of clustering of particles in the homogeneous and the low d_f systems. In homogeneous disordered system modes localized on a very small number of particles or on pairs are surrounded by a uniform distribution of particles that contribute to increase the lifetime of the mode. In the case d_f=1.6, despite the heterogeneity of the point distribution, the area filled by "islands" of particle are larger compared to the

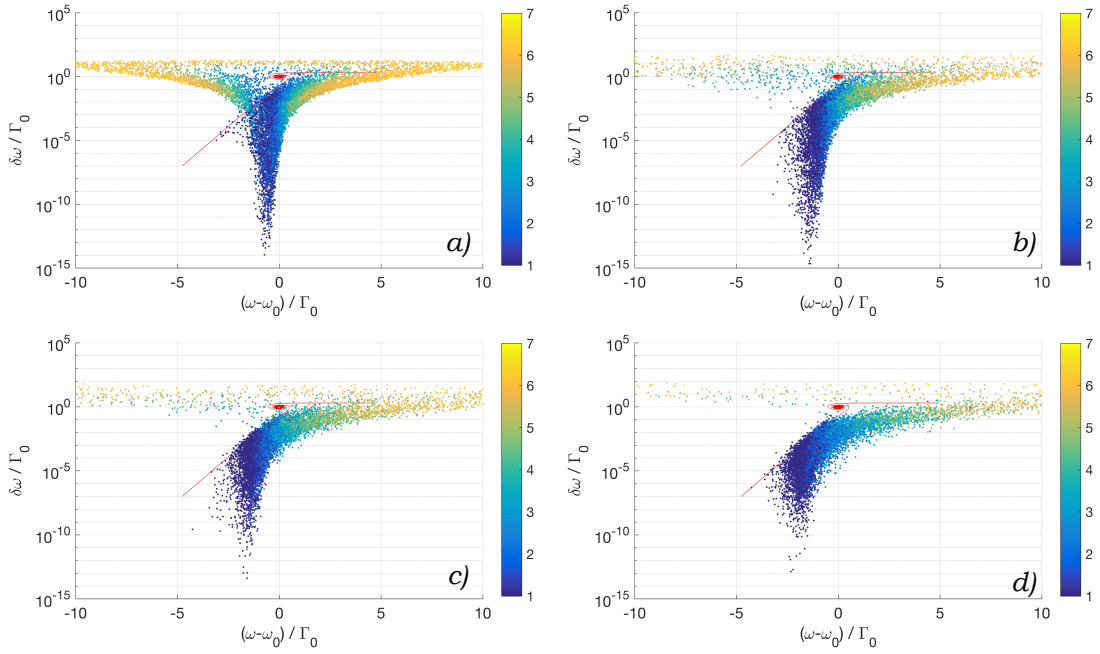

Fig. 2.15: Eigenvalues distribution of N=1024 2D dipoles system in a circle of radius R=3 µm of 10 disorder realization for four type of different systems. The red curve indicates the proximity resonances of a 2 particle systems at different distances between them, while the color bars rappresent the degree of spatial localization in terms of logarith of the number of particles involved in the mode log(MSE). In *a*) the resonances of the homogeneous disorder system are depicted. The dipole resonance wavelength has been chosen in order to have $\rho\lambda^2$=13. *b*), *c*) and *d*) correspond to Soneira-Peeble distributions with fractal dimension 1.6, 1.4 and 1.2 respectively. The decrease of fractal dimension leads to a higher proximity of the scattering particles and thus to a higher number of modes with low MSE, shifted towards more negative detuning from the dipole resonance frequency. However these modes localized on few scatterers exhibit a lower lifetime than the localized one of the homogeneous or the high fractal dimension systems. Moreover, expecially in the d_f=1.2 case, they are shifted in frequency and width towards the curve indicating the proximity resonance states.

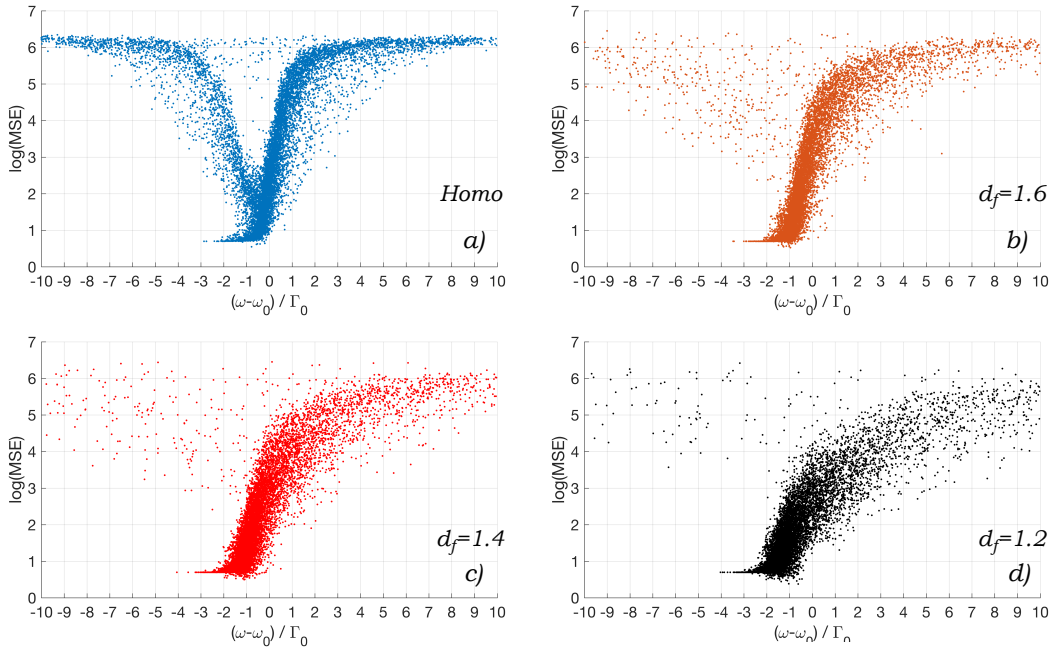

Fig. 2.16: Frequency Vs log(MSE) of 10 disorder realization of the homogeneous (a), fractal with d_f=1.6 (b), fractal with d_f=1.4 (c) and fractal with d_f=1.2 (d). The analysis have been performed on the same systems of Fig. 2.15.

case of d_f=1.4 and 1.2, where the pairs are in really high density spots but very close to large empty regions. This is a concept confirmed by the analysis reported in Figure 2.14, that show the trajectory of a proximity resonance mode in the complex plane in a sequence of steps where the surrounding scatterers, starting from those more far, are removed. In each step the modes of the system are computed again. In order to find in each iteration the "old" mode, the correlation of the new modes intensity maps with the original one are evaluated. The frequency and spectral width shifts are then computed for that specific iteration. It is clear how removing the scatterers around the pair the frequency of the mode keeps the same value but its lifetime tents to decrease.

MSE analysis

The MSE calculations reported in Figure 2.16 can be repeated for other radius of the system in order to perform a preliminary study of the mode extension as a function of the system density. As it is clear from the eigenvalues distribution in Figure 2.1 and 2.15, configurations with a higher average value of $\rho\lambda^2$, exhibit states confined on few scatterers with high lifetime and negative detuning approximately of one or two units of Γ_0. In previous studies on localization of QNM of point-like strongly resonant distributions [6], consisting as in this work in the calculation of the Green matrix eigenvalues, the spectral region considered to investigate the transport in the localization regime is a frequency interval around $Re(\lambda_G)$=1, the one where, increasing the scattering strength of the system, very significant changes occur in the modes size and width. It is thus reasonable to perform here a study on the mode spatial extent statistic in the same

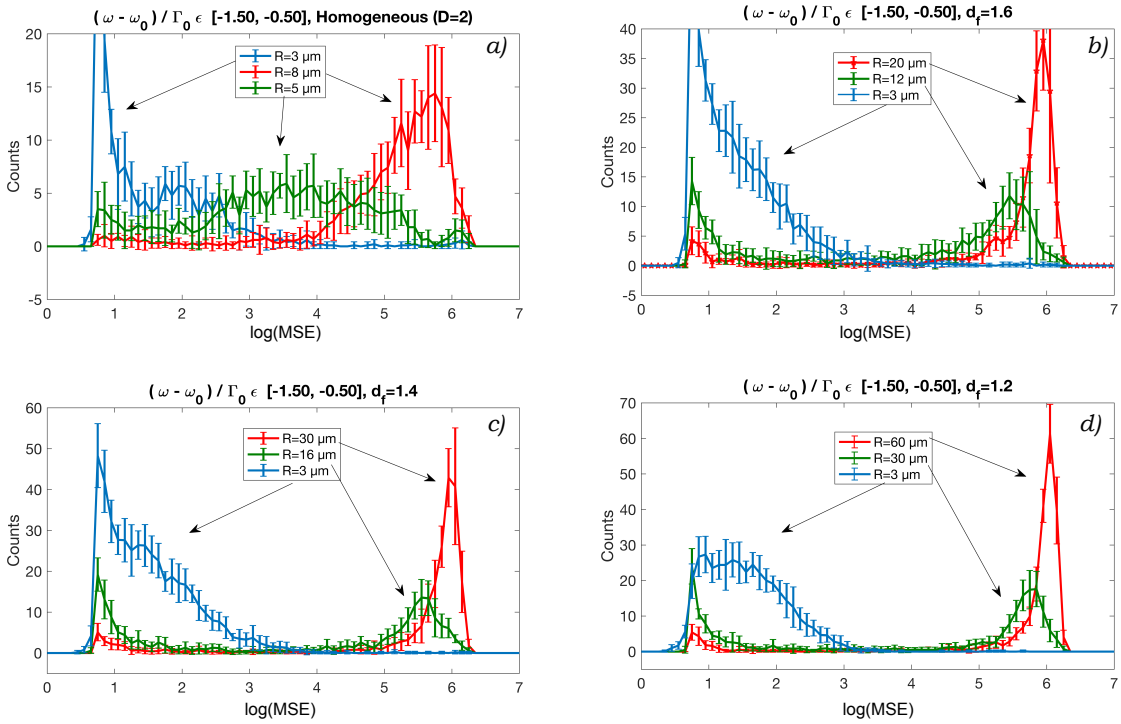

Fig. 2.17: Histogram rappresentation of the log(MSE) distributions in the frequency window $Re(\lambda_G)\ \epsilon\ [-1.5, -0.5]$ for *a)* homogeneous disordered distribution, *b)* fractal distribution with d_f=1.6, *c)* fractal distribution with d_f=1.4 and *d)* fractal distribution with d_f=1.2. In each graph, different radius of the system are considered, while the number of scattering particles is kept constant. In all cases, increasing the radius, i.e. decreasing the scattering strength, leads to a "migration" of modes average degree of localization from few to many scattering centers. While in the homogeneous case an intermediate configuration where a wide interval of log(MSE) is present (green curve of *a*), the fractal systems shows for every d_f only regimes where the transport occurs exclusively through states with either very few (approximately MSE<5) or a large number (approximately MSE>300) of scatterers involved.

interval. Moreover, in an hypothetical experiment where the system modes are excited with monochromatic light, the transport will occur with higher probability only through the states spectrally overlapped to the source frequency, and thus in a limited spectral region, legitimating a choice of Γ_0 as interval width. The histograms of the log(MSE) in the homogeneous and fractal systems referred to the interval $Re(\lambda_G)\ \epsilon\ [-1.5, -0.5]$ and different system size is reported in Figure 2.4. An interesting information retrieved by this analysis is how the consider quantity evolves changing the radius from small to large values, corresponding to configurations where the conserved amount of scattering particles become diluted and the log(MSE) tends to become on average larger. The histograms have been computed for 50 disorder realizations of each configuration and the mean values and the relative errorbars are reported in the graph. Figure 2.17, corresponding to the homogeneous case of systems with $\rho\lambda^2$=13, 4.7 and 1.8. The histograms show how decreasing the system density, the degree of localization, high at $\rho\lambda^2$=13 (blue curve), decreases, with a probability density moving to high number of scattering centers involved and thus low degree of localization (red curve). Furthermore, it is possible to find an intermediate density where the QNM MSE is spread on a broader interval (green curve). A different behavior can be found in graphs 2.17a, b and c reporting the analysis on the fractals distributions with d_f=1.6, 1.4 and 1.2 respectively. The higher is the fractal dimension, corresponding to a higher packing of the dipoles, the more the system has to be rescaled to get a configuration where most of the modes are extended on a large number of scattering particles. Important fact is that there is no intermediate configuration with a broad interval of log(MSE), as it happens in the homogeneous case, but instead a coexistence of modes localized either on a really small or very large number of scatterers occur (green curves). This indicates that the self-similarity in these systems allows the coexistence of the same number of modes with a completely different degree of localization inside the system. Nevertheless one has to be aware that the quantity just discussed is not a quantitative evaluation of the true size of the modes.

2.5 Mode size distribution in fractal systems

The previous MSE analysis considered in section 2.4.2 demonstrates how mode size is a quantity strongly affected by the arrangement of the scattering particles in the system. Anyway, it is fundamental to point out again the meaning of the MSE considered so far, that have been computed from the eigenvectors of the systems, i.e the electric field values at the positions of the scattering centers (see equation (2.13)). This means that the informations retrieved provide the degree of spatial extent of the modes only in terms of number of scattering points involved. In order to calculate an exact value of the mode size is necessary to repeat the IPR calculations in all the space, computing, from the eigenvectors, the propagator G from the dipole positions to any other point. This procedure has been applied to obtain the intensity maps in Figure 2.4 (see equation (2.14)). Of course, as the calculation is done numerically on a mesh of the system, the degree of accuracy will depend by the resolution of the mesh. From the electric field values of a single mode retrieved in this way, the IPR is computed in every pixel of the mesh and the mode area, defined as Mode Extent (ME), can be retrieved (Figure 2.18). In this last part of the chapter a ME analysis is presented. A comparison with

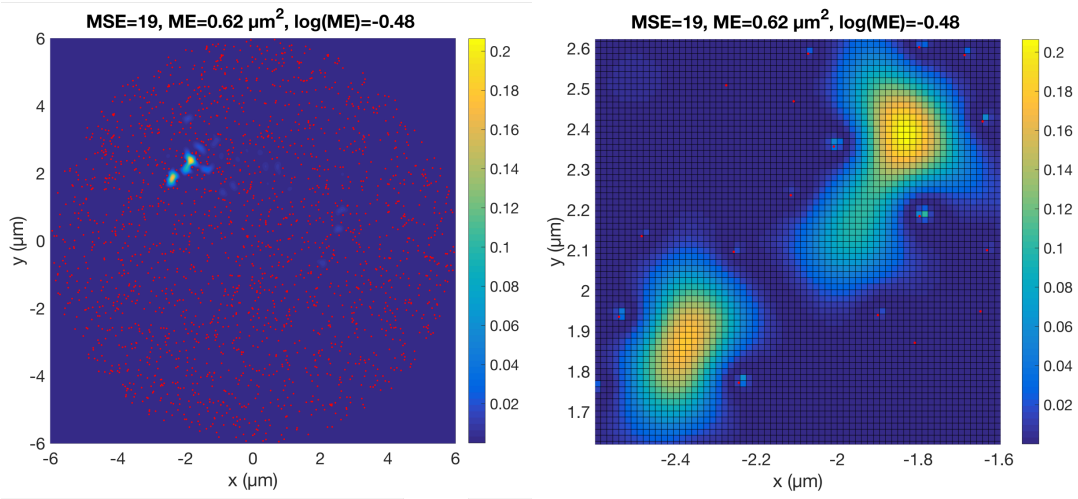

Fig. 2.18: On the left example of a localized QNM intensity map from an homogeneous disordered system with $N = 2048$ and $R = 6\,\mu\text{m}$, i.e. $\rho\lambda^2$=6.5. On the right an insight of the map shows a mesh with resolution $\lambda/40$. The mode intensity has been computed with equation 2.14 in each point of the mesh.

the result of the previous section is performed, i.e. with the histograms of the degree of localization in terms of number of particles involved in the mode (Figure 2.17). To keep the previous section notation, we will keep referring to this quantity as MSE. ME is a fundamental step in the study of the QNM size in fractals, because of the intrinsic heterogeneity nature of the fractal distributions. In fact in an homogeneous disordered system the MSE is a reliable quantity for a mode size evaluation as it is possible to define an average minimum distance between the nearest neighbors scattering points, and knowing the number of particles where the mode intensity does not vanish allows to obtain a reliable value of the mode area. This is evident in Figure 2.19, where the graphs of the frequency dependence of log(MSE) and $\log(\text{ME}/\lambda^2)$ for the homogeneous disordered system are displayed. The distributions are very similar and also in the case of the ME calculation the "V-shape" profile is present. The main difference is due to the boundaries of the MSE: the upper boundary is N/2, intrinsic of the model used, and a lower one is approximately 2, corresponding to the proximty resonance states. The log(ME) displays a lower boundary depending only on the mesh resolution, permitting to discriminate the sizes of both the proximity resonance, that show up for any particle distance causing the formation of modes on pairs that might have different size, and the localized modes in the system. These considerations become important in the study of mode size statistic in fractal distributions, where the lack of homogeneity does not allow to determine an average distance between the particles. As a consequence, modes with comparable MSE may reveal very different sizes. An example is reported in Figure 2.20.

Calculations of the ME have been performed on the previously studied fractal systems, i.e with parameters $N = 1024$, $R = 3\,\mu\text{m}$ and d_f =1.6, 1.4 and 1.2. to compare their mode size statistic with the one of the homogeneous case. The distributions so obtained[2] are depicted in Figure 2.21. It is here possible to appreciate, contrary to the homogeneous

[2]The distribution related to the system with $d_f = 1.2$ will be shown and commented later.

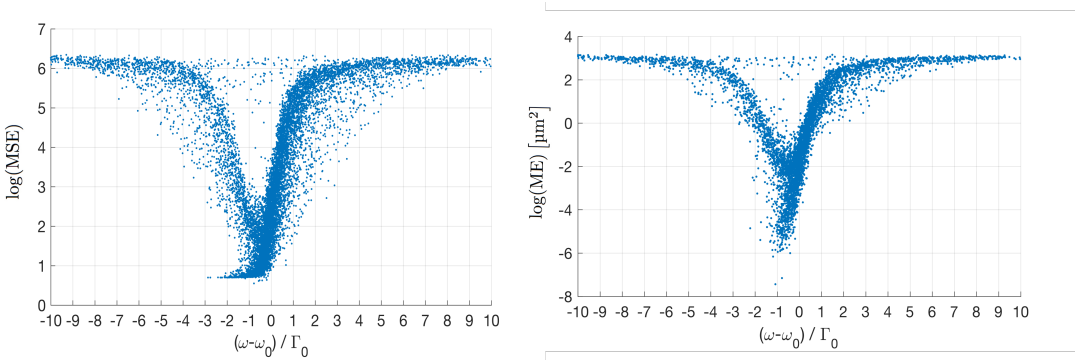

Fig. 2.19: Frequency dependence of log(MSE) and log(ME) for an homogeneous disordered system with $N = 1024$ and $R = 3\,\mu m$. The two distributions appear quite similar, due to the fact that the type of disorder allows to determine an average distance between the scattering particles, constant in all the sample. The number of particles in a single mode region is thus a good descriptor of the mode effective size.

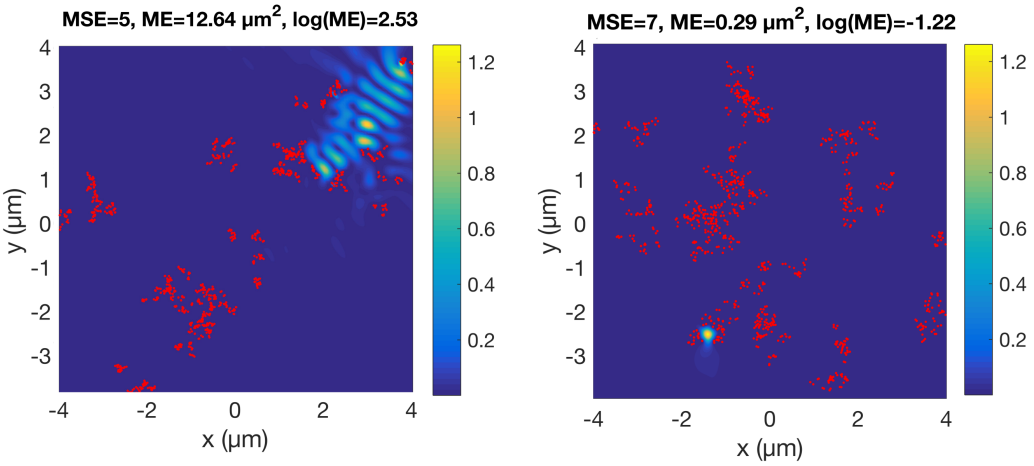

Fig. 2.20: Two modes in fractal system with comparable MSE but different ME. Despite the ME are very different, the region where modes intensity does not vanish is populated by approximately the same number of dipoles, due to the strong fluctuations of scatterers density in the system. A mode size analysis of fractal system needs thus to be performed computing the ME.

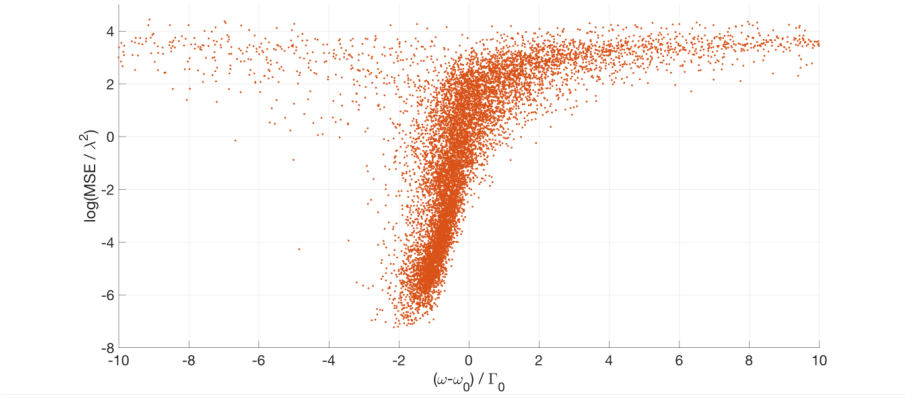

a)

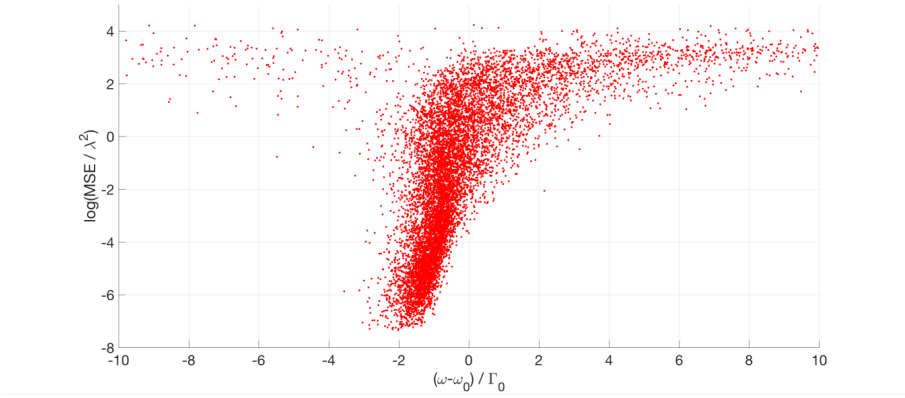

b)

Fig. 2.21: Mode size expressed as $\log\left(ME/\lambda^2\right)$ Vs modes frequency in Soneira-Peebles distributions with $N = 1024$ and $R = 3\,\mu\text{m}$, for $d_f = 1.6$ (a), orange points, $d_f = 1.4$ (b), red points. These graphs show different features from the MSE distribution in Figure 2.16, showing how mode size statistic in the fractals requires a study in terms of ME.

disordered case, the significant difference from the relative MSE distributions previously shown in Figure 2.16. In fact, in the spectral region considered for mode size statistic analysis, i.e. the one where the lifetime and the degree of localization is more affected by the changes in system scattering strength, a stripe of modes from a broad range of log(MSE) is present. This feature indicates the possible coexistence of mode of every possible size in a a 2D system with fractal arrangement of scattering centers. In order to get more insight in this relevant aspect of wave transport in the self-similar structure considered, a further analysis has been performed in order to verify the real impact of the fractality on the mode size coexistence. As the comparison presented so far concerns two extremely different types of disordered system, the Soneira-Peebles distributions and the homogeneous random distributions, it is necessary to consider the possibility that the coexistence of ME is not strictly related to the scale-invariance of the fractal structures but to the intrinsic heterogeneity of their scattering particle arrangements. In the next section the histograms of the ME distribution of a fractal, an homogeneous, and an heterogeneous system without scale invariance are presented, with the purpose to show how the mode size coexistence is a feature related to the system fractality and not to the mere heterogeneity.

2.6 Mode size coexistance in fractals

The coupled dipole formalism employed so far reveled how the mode properties of a random system are strongly affected by the nature of the underlying disorder and the mutual distances between particles. We have observed how, when there is a nearest neighbors distance between the scattering centers approximately constant for all of them, i.e. the homogeneous case, a limited range of mode size is supported.[3] On the other hand, introducing density fluctuations through the Soneira-Peeble algorithm leads to the formation of both extended and localized modes at the same frequency, as shown in Figure 2.21. To determine if the coexistence mechanism is a property strictly related to the scale-invariance of the fractal distribution, it is necessary to consider also systems with comparable interparticle distances but exhibiting a lack of self-similarity. In order to make a fair comparison, the heterogeneous systems considered have been obtained generating Soneira-Peeble structures and breaking the self-similarity of the point distribution, dividing the system in λ side square cells and rearranging the scattering centers inside each cell in a homogeneous fashion (Figure 2.22). It worths to point-out that, despite the examples in Figure 2.22b and c show structures where the maximum values of interparticle distance are different, the average mutual distance in the fractal and the heterogeneous cases becomes comparable averaging on more disorder realizations. For the ME analysis, the average $\log\left(ME/\lambda^2\right)$ on 50 disorder realizations in the frequency window [-1.5,-0.5] have been calculated. The fractal dimension of the fractal system considered is $d_f = 1.2$. The results are reported in 2.23. The histograms reveal how the Soneira-Peeble system exhibits a coexistence of modes with a wide range of sizes, indicating the presence of spectrally overlapped localized and extended states. This coexistence is not displayed by the homogeneous system, where the ME distribution presents a concentration of modes from a small size interval. This result

[3] We keep considering the frequency interval $(\omega - \omega_0)/\Gamma_0 \in [-1.50, -0.5]$, motivated in section 2.4.2.

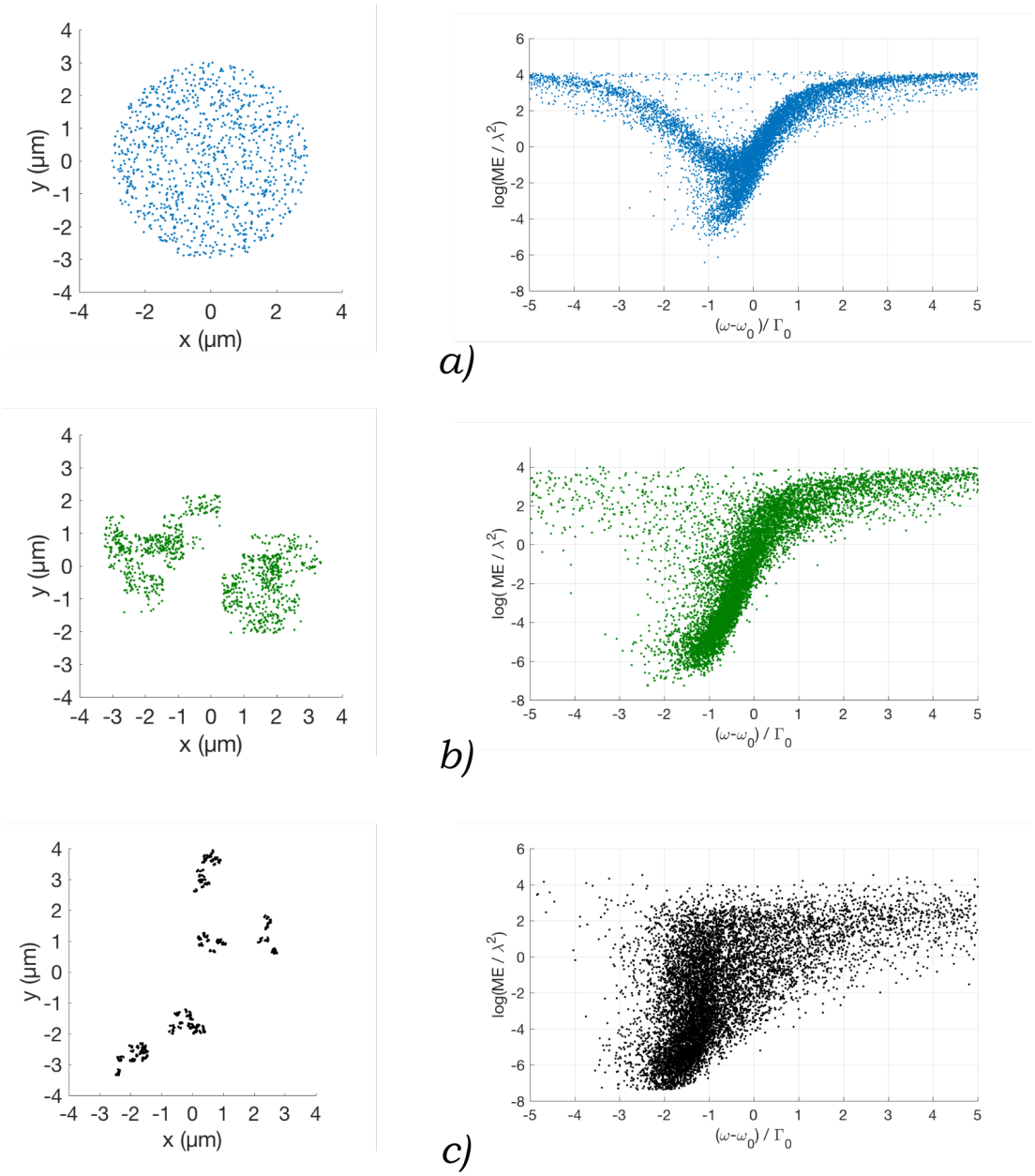

Fig. 2.22: Representation of the single realizations of the three disorder fashion investigated (left column) and the relative log $\left(ME/\lambda^2\right)$ distributions from 10 disorder realizations (right column). *a*) Homogeneous (blue) disordered distribution, with a specific average distance between the particle. *b*) Heterogeneous (green) distribution obtained rearranging the scatterers of a Soneira-Peeble distribution $d_f = 1.2$, with the scope of removing the self-similarity of the system. It has been shown that the results are, as expected, independent by the d_f of the initial Sonerira-Peeble structure. *c*) Soneira-Peeble, and thus fractal, system with $d_f = 1.2$. Performing a study on the ME of these systems, especially comparing the values in the fractal and in the heterogeneous cases, the structural feature responsible of the coexistence of modes observed in Figure 2.21 can be revealed.

confirms our consideration on the ME in fractals done in section 2.5. In Figure 2.23a, the size distribution of the heterogeneous is depicted. Despite the heterogeneous system displays a broader size distribution than the homogeneous, it is neither as large nor as flat as the one corresponding to the fractal system. In fact the green curve shows a peak, indicating that a large fraction of the mode in that frequency window is localized but there is a lack of extended states. It is important to stress that this particular effect is indeed due to the system self similarity and it is not a mere effect of the heterogeneity.
To make this claim stronger it is necessarily to show that this analysis is not restricted to the structural configuration considered, i.e. changing the size of the system it is not possible to find another configuration where either the homogeneous or the heterogeneous ensemble exhibit coexistence. For this purpose, we considered a more diluted system, with respectively $R = 6\,\mu\text{m}$. This choice is due to the distribution of the heterogeneous system for $R = 3\,\mu\text{m}$ (Figure 2.23), showing a lack of extended states. An hypothetical coexistance in the heterogeneous would be expected at higher R, where more extended states would be more likely to be found. Before performing this analysis, some considerations of the procedure to generate the heterogeneous distribution should be done. As already mentioned, to obtain an heterogeneous system suitable to make a comparison with the self-similar structures, the scatterers of a Soneira-Peeble are randomly redistributed inside square cells. Now that an analysis for different system size is performed, it is necessary to consider again the size of the square cell. This is due to the fact that the Soneira-Peeble structure are themselves statistical fractals, where in each step of the algorithm new points are randomly generated inside a specific volume. As the radius of each step of the algorithm depends on R, the 0 step sphere, the radius of the few last iterations, i.e. those determining the scatterers positions, will be different for different R. This means that, if the side of the square is not large enough with respect to R, the rearranged point distributions would become really close to be the analogous of another Soneira-Peeble disorder realization. This idea is explained in Figure 2.24, where a comparison between the fractal system and the corresponding rearranged heterogeneous system are shown for $R = 3\,\mu\text{m}$ (the case of Figure 2.23) and $R = 6\,\mu\text{m}$. In both cases the mesh defined has size λ. It is evident how the mesh of the $R = 6\,\mu\text{m}$ system is too fine, and the two structures looks very similar. Therefore, it has been chosen to perform the ME analysis for $R = 6\,\mu\text{m}$ redistributing the scatterers in 2λ size squares. The results are reported in Figure 2.25. Also in this case the fractal system exhibits a coexistence of all the possible mode sizes, not present in the heterogeneous and the homogeneous systems.

Fractal dimension comparison

One last analysis based on the ME calculation is the comparison of the $\log\left(ME/\lambda^2\right)$ distributions for fractal systems with different fractal dimensions. We report here the mode size distribution in both all the spectrum and the frequency interval $[-1.5, -0.5]$, depicted in Figure 2.26. All the systems display size coexistance, but the distribution does not reveal any strong dependence from the fractal dimension. Despite this evidence, it is not possible to state that the variations of structural parameters do not influence the mode size distribution of the fractals, as the reason behind this lack of

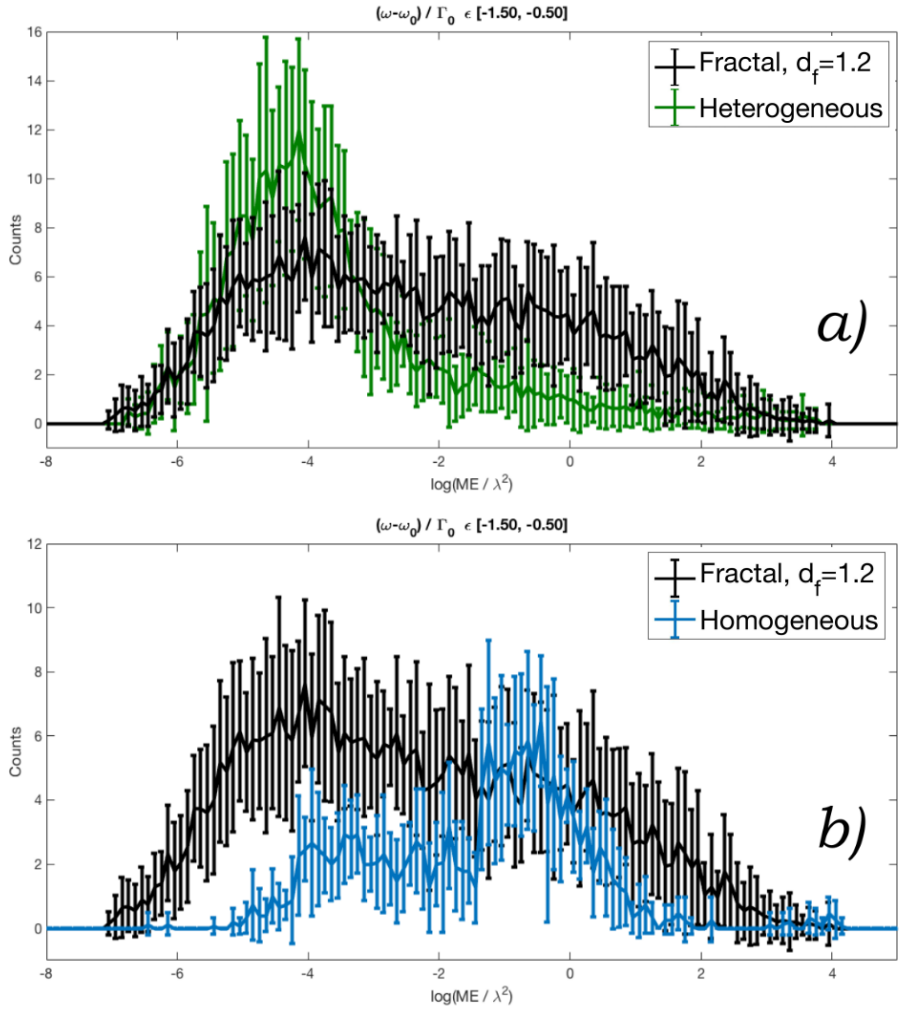

Fig. 2.23: Comparison of the ME distributions in the frequency interval $(\omega - \omega_0)/\Gamma_0 \in [-1.50, -0.5]$ between the fractal system with $d_f = 1.2$ and $a)$ Heterogeneous disordered system and $b)$ Homogeneous disordered system. The histograms have been computed averaging over 50 disorder realizations. The dipole distributions are of the type depicted in Figure 2.22. The histograms reveal how the fractal system exhibit a coexistance of modes with a wide range of sizes, indicating the presence of both localized and extended states spectrally overlapped.

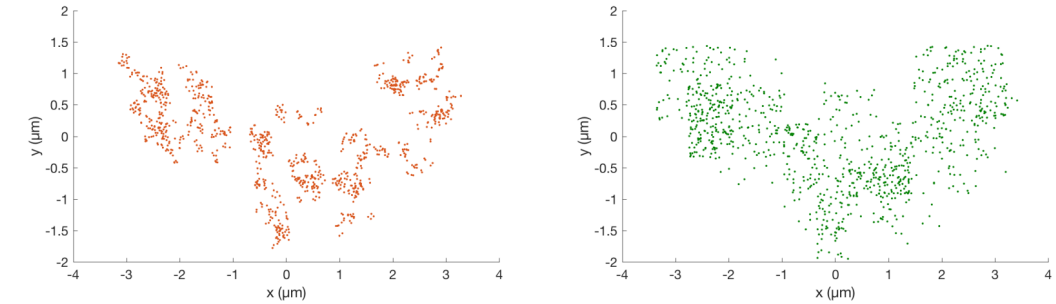

a)

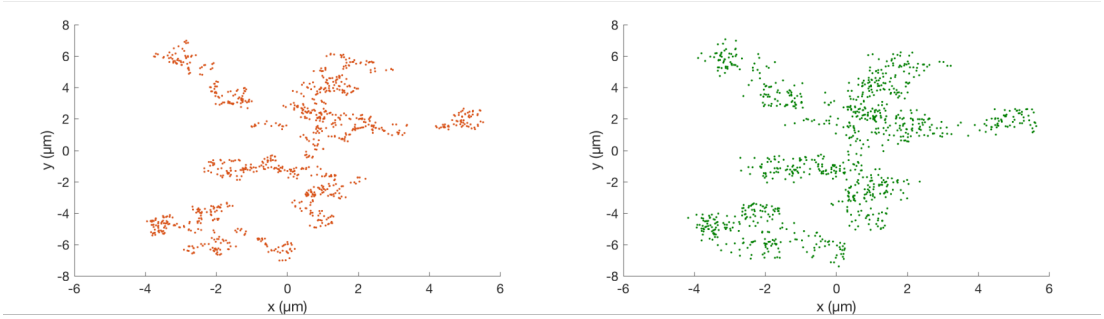

b)

Fig. 2.24: Comparison between Soneira-Peeble distributions and the heteorgeneous systems obtained dividing the system in λ side square cells and rearranging the scattering centers inside each cell in a homogeneous fashion. *a)* represents the case of radius $R = 3\,\mu\text{m}$, while *b)* represents the case of radius $R = 6\,\mu\text{m}$.

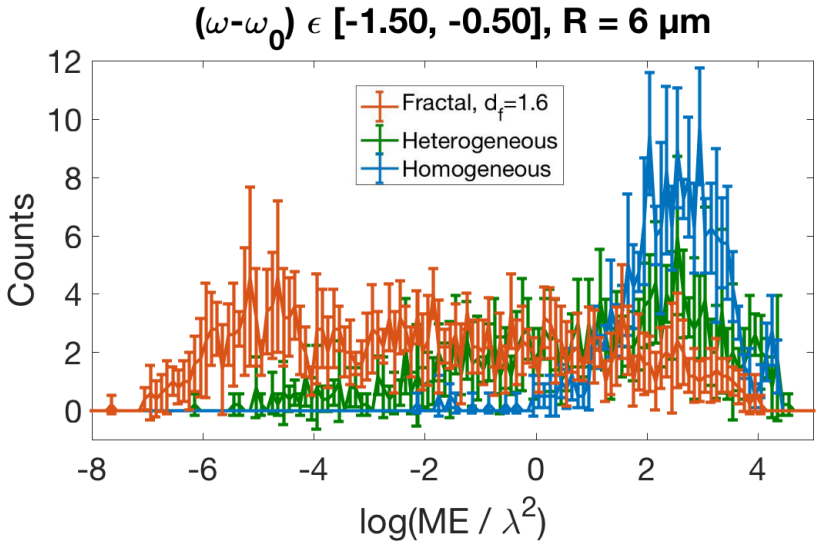

Fig. 2.25: Comparison of the ME distributions in the frequency interval $(\omega - \omega_0)/\Gamma_0 \in [-1.50, -0.5]$ between the fractal system with $d_f = 1.6$, the heterogeneous and homogeneous systems. The radius is set to $R = 6\,\mu\text{m}$.

different features at different fractal dimensions could in principle be strictly related to the specific self-similar systems investigated. In fact, the Soneira-Peeble structures considered are not ideal fractals and they exhibit self similarity only on a finite length intervals. It is thus reasonable to associates this behavior to an insufficient number of algorithm iterations, that lead to generate scattering centers configurations which mode size distribution is affected by the scale-invariance but it is not affected by the parameters that characterize the scaling. A dependence by d_f would thus be appreciated performing the calculations on larger systems generated by a larger number of iterations to provide the scale-invariance on more orders of magnitude.

To conclude, a study of the QNM in 2D disorder systems has been performed. Approximating the system scattering centers to point-dipoles, we retrieved quantitative results which validity is extended to any optical system with strongly resonant scatterers. The excitations of the electromagnetic fields have been computed by solving the Maxwell equations in the single-scattering approximation. Strongly resonance scatterers condition, i.e. Breit-Wigner type scatterers assumption, have been used to associates to each mode a specific frequency and lifetime. An analysis of the QNM size supported by the dipole ensemble has been performed in homogeneous disordered systems, heterogeneous disordered systems and scale-invariant systems generated through the Soneira-Peeble algorithm, an algorithm designed for the purpose to generate fractal point-distributions with tunable fractal dimensions. Calculating the size of the QNM mode, defined as ME, and comparing the results in the three different types of disorder, it has been possible to conclude that, contrary to the homogeneous and the heterogeneous disorder media, the fractal system presents at least one configuration where the geometric self-similarity affects the mode size statistics, generating a coexistence of a wide range of mode sizes.

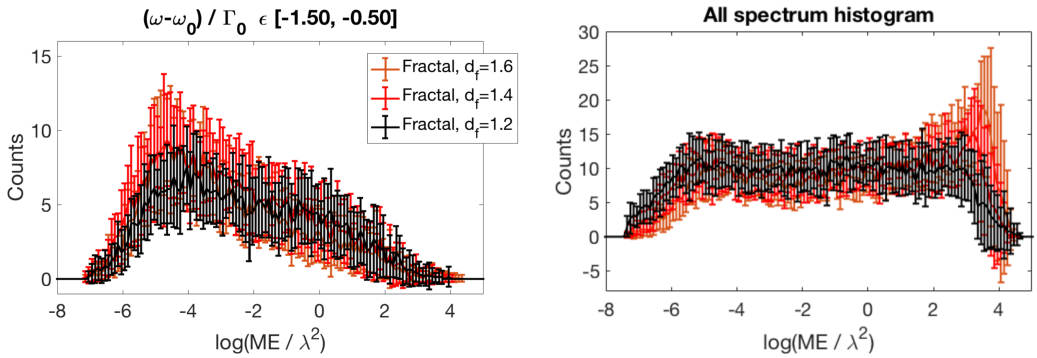

Fig. 2.26: Comparison between the ME histograms of Soneira-Peeble distributions with different fractal dimensions, corresponding to systems with $N = 1024$ and $R = 3\,\mu\text{m}$.

References

[1] P. T. Leung, S. Y. Liu, and K. Young. "Completeness and orthogonality of quasinormal modes in leaky optical cavities". In: *Physical Review A* 18 (1994), p. 3057.

[2] E. S. C. Ching et al. "Quasinormal-mode expansion for waves in open systems". In: *Reviews of modern physics* 70 (1998), p. 1545.

[3] P. Lalanne et al. "Light interaction with photonic and plasmonic resonances". In: *arXiv* 1705.02433 (2017).

[4] R. Chang and A. Campillo. *Optical processes in microcavities, Chap. 1.* World Scientific, London, 1996.

[5] B. Vial et al. "Quasimodal expansion of electromagnetic fields in open two-dimensional structures". In: *Physical Review A* 89 (2014), p. 023829.

[6] S. E. Skipetrov and I. M. Sokolov. "Absence of Anderson localization of light in a random ensemble of point scatterers". In: *Physical Review Letters* 112 (2014), p. 023905.

[7] S. E. Skipetrov. "Finite-size scaling analysis of localization transition for scalar waves in a three-dimensional ensemble of resonant point scatterers". In: *Physical Review B* 94 (2016), p. 064202.

[8] C. E. Màximo et al. "Spatial and temporal localization of light in two dimensions". In: *Physical Review A* 92 (2015), p. 062702.

[9] J. Andreasen et al. "Modes of random lasers". In: *Advances in Optics and Photonics* 3 (2011), pp. 88–127.

[10] A. Goetschy and S. E. Skipetrov. "Euclidean matrix theory of random lasing in a cloud of cold atoms". In: *Europhysics Letters* 96 (2011), p. 34005.

[11] X. Wu et al. "Effect of local pumping on random laser modes in one dimension". In: *Journal of the Optical Society of America B* 24.10 (2007), A26–A33.

[12] C. Sauvan et al. "Theory of the spontaneous optical emission of nanosize photonic and plasmon resonators". In: *Physical Review Letters* 110 (2013), p. 237401.

[13] J. P. Vasco and S. Hughes. "Statistics of Anderson-localized modes in disordered photonic crystal slab waveguides". In: *Physical Review B* 95 (2017), p. 224202.

[14] M. Segev, Y. Silberberg, and D. N. Christodoulides. "Anderson localization of light". In: *Nature Photonics* 7 (2013).

[15] G. M. Conley et al. "Light transport and localization in two-dimensional correlated disorder." In: *Physical Review Letters* 112.14 (2014), p. 143901.

[16] E. Abrahams, P. W. Anderson, and T. V. R. D. C. Licciardello. "Scaling Theory of Localization: Absence of Quantum Diffusion in Two Dimensions". In: *Physical Review Letters* 42.10 (1992), pp. 673–676.

[17] L. D. Negro, R. Wang, and F. A. Pinheiro. "Structural and Spectral Properties of Deterministic Aperiodic Optical Structures". In: *Crystals* 6.12 (2016), p. 161.

[18] A. Christofi, F. A. Pinheiro, and L. D. Negro. "Probing scattering resonances of Vogel's spirals with the Green's matrix spectral method". In: *Optics Letters* 41.9 (2016), pp. 1933–1936.

[19] V. M. Shalaev. *Nonlinear Optics of Random Media.* Springer, Berlin, 2000.

[20] M. I. Stockman. "Inhomogeneous eigenmode localization, chaos, and correlations in large disordered clusters". In: *Physical Review E* 56.6 (1997), pp. 6494–6507.

[21] D. P. Tsai et al. "Inhomogeneous eigenmode localization, chaos, and correlations in large disordered clusters". In: *Physical Review Letters* 72 (1994), p. 4149.

[22] M. V. H. Rao, B. K. Mathur, and K. L. Chopra. "Evaluation of the scaling exponent of selfaffine fractal surface from a single scanning probe microscope image". In: *Applied Physics Letters* 65.1 (1994), pp. 124–126.

[23] A. M. Brasil, T. L. Farias, and M. G. Cantalho. "Evaluation of the Fractal Properties of Cluster-Cluster Aggregates". In: *Aerosol Science and Technology* 3 (2000), pp. 440–454.

[24] R. Thouy and R. Jullien. "A cluster-cluster aggregation model with tunable fractal dimension". In: *Journal of Physics A: Mathematical and Theoretical* 27 (1994), pp. 2953–2963.

[25] V. M. Shaelev et al. "Optical properties of self-affine thin films". In: *Physical Review B* 54.1 (1996), pp. 440–454.

[26] V. A. Markel et al. "Theory and numerical simulation of optical properties of fractal clusters". In: *Physical Review B* 43.10 (1991), pp. 8183–8195.

[27] V. A. Markel et al. "Small-particle composites. I. Linear optical properties". In: *Physical Review B* 53.5 (1996), pp. 2425–2436.

[28] E. M. Purcell and C. R. Pennypacker. "Scattering and absorption of light by nonspherical dielectric grains". In: *Astrophys Journal* 186 (1973), pp. 705–714.

[29] B. T. Draine. "The discrete-dipole approximation and its application to interstellar graphite grains". In: *Astrophys Journal* 333 (1988), pp. 848–872.

[30] H. DeVoe. "Optical properties of molecular aggregates. I. Classical model of electronic absorption and refraction". In: *J. Chem. Phys.* 41 (1964), pp. 393–400.

[31] S. B. Singham and C. F. Bohren. "Light scattering by an arbitrary particle: a physical reformulation of the coupled-dipoles method". In: *Optics Letters* 12 (1987), pp. 10–12.

[32] B. T. Draine and P. J. Flatau. "Discrete-dipole approximation for scattering calculations". In: *J. Opt. Soc. Am. A* 11.4 (1994).

[33] A. Lagendijk and B. A. V. Tiggelen. "Resonant multiple scattering of light". In: *Physics Reports* 270 (1996), pp. 143–215.

[34] B. A. van Tiggelen, A. Lagendijk, and A. Tip. "Multiple-scattering effects for the propagation of light in 3D slabs". In: *Journal of Physics: Condensed Matter* 2.37 (1990), p. 7653.

[35] M. B. van der Mark, M. P. van Albada, and A. Lagendijk. "Resonant multiple scattering of light". In: *Phys. Rev. B* 37 (1988), p. 3755.

[36] M. Rusek, J. Mostowsky, and A. Orlowsky. "Random Green matrices: From proximity resonances to Anderson localization". In: *Physical Review A* 61 (1999), p. 022704.

[37] L. Bellando et al. "Cooperative effects and disorder: A scaling analysis of the spectrum of the effective atomic Hamiltonian". In: *Physical Review A* 90 (2014), p. 063822.

[38] E. Abrahams et al. "Scaling Theory of Localization: Absence of Quantum Diffusion in Two Dimensions". In: *Physical Reveiw Letters* 42.10 (2002), pp. 673–676.

[39] E. J. Heller. "Quantum Proximity Resonances". In: *Physical Review Letters* 77.20 (1996).

[40] B. Mandelbrot. *The Fractal Geometry of Nature*. W. H. Freeman and Company, 1982.

[41] B. Mandelbrot. "How Long Is the Coast of Britain? Statistical Self-Similarity and Fractional Dimension". In: *Science* 156 (1967), pp. 636–638.

[42] B. Mandelbrot. "How Long Is the Coast of Britain? Statistical Self-Similarity and Fractional Dimension". In: *Proceeding of Graphics Interface* (1993), pp. 174–180.

[43] D. G. Tarboton, R. Bras, and I. Rodriguez-Iturbe. "The Fractal Nature of River Networks". In: *Water Resources Center* 24.8 (1988), pp. 1317–1312.

[44] M. C. Giacometti et al. "Models of Fractal River Basins". In: *Models of Fractal River Basins* 91 (1998), pp. 1–15.

[45] O. M. Bruno et al. "Models of Fractal River Basins". In: *Information Sciences* 178 (2008), pp. 2722–2733.

[46] K. Ritz and J. Crawford. "Quantification of the fractal nature of colonies of Trichoderma viride". In: *Mycological Research journal* 94.8 (1990), pp. 1138–1152.

[47] T. J. Rudge et al. "Cell Polarity-Driven Instability Generates Self-Organized, Fractal Patterning of Cell Layers". In: *ACS Synthetic Biology* 2.12 (2013), pp. 705–714.

[48] T. Matsuyama and M. D. M. Matsushita. "Quantification of the fractal nature of colonies of Trichoderma viride". In: *Critical Reviews in Microbiology* 19.2 (1993), pp. 117–135.

[49] T. Smith, G. D. Lange, and W. Marks. "Fractal methods and results in cellular morphology - dimensions, lacunarity and multifractals". In: *Journal 0f Nanoscience Methods* 69 (2008), pp. 123–136.

[50] T. Smith, G. D. Lange, and W. Marks. "Modeling of Lung Morphogenesis Using Fractal Geometries". In: *IEEE Transaction on medical imaging* 7.4 (1988), pp. 123–136.

[51] B. Mauroy et al. "An optimal bronchial tree may be dangerous". In: *Nature* 427 (2004), pp. 633–636.

[52] A. Eke et al. "Fractal characterization of complexity in temporal physiological signals". In: *Physiological Measurements* 23 (2002), R1–R38.

[53] C. K. Peng et al. "Quantification of scaling exponents and crossover phenomena in nonstationary heartbeat time series". In: *AIP Chaos* 5.1 (1995), pp. 82–87.

[54] G. M. Viswanathan et al. "Lévy flight search patterns of wandering albatrosses". In: *Nature* 381 (1996), pp. 413–415.

[55] M. E. Wosniack et al. "The evolutionary origins of Lévy walk foraging". In: *PLoS Computational Biology* 13.10 (2017), e1005774.

[56] M. E. Wosniack et al. "Lévy flights and superdiffusion in the context of biological encounters and random searches". In: *Physics of Life Reviews* 5.3 (2008), pp. 133–150.

[57] D. Brockmann, L. Hufnagel, and T. Geisel. "The scaling laws of human travel". In: *Nature* 439 (2006), pp. 462–465.

[58] I. Rhee et al. "On the Levy-walk Nature of Human Mobility". In: *IEEE/ACM Transactions on Networking* 19.3 (2011), pp. 630–643.

[59] M. F. Shlesinger, J. Klafter, and Y. M. Wong. "Random walks with infinite spatial and temporal moments". In: *Journal of Statistical Physics* 27.3 (1982), p. 499.

[60] V. Zaburdaev, S. Denisov, and J. Klafter. "Lévy walks". In: *Review of Modern Physics* 87.2 (2015), p. 237401.

[61] M. F. Shlesinger, G. Zaslavsky, and U. Frisch. *Lévy Flights and Related Topics in Physics*. Springer, Berlin, 1995.

[62] Y. Sagi et al. "Observation of Anomalous Diffusion and Fractional Self-Similarity in One Dimension". In: *Physical Review Letters* 108.9 (2012).

[63] H. Katori, S. Schlipf, and H. Walther. "Anomalous Dynamics of a Single Ion in an Optical Lattice". In: *Physical Review Letters* 79.12 (1997), pp. 602–605.

[64] D. A. Kessler and E. Barkai. "Theory of Fractional Lévy Kinetics for Cold Atoms Diffusing in Optical Lattices". In: *Physical Review Letters* 108.23 (2002), p. 602.

[65] N. Mercadier et al. "Lévy flights of photons in hot atomic vapours". In: *Nature Physics* 5 (2009), pp. 602–605.

[66] S. J. DuHamel RH. *Frequency-independent antennas. In: Johnson RC, ed. Antenna Engineering Handbook. 3rd.* McGraw-Hill, 1993.

[67] C. Puente et al. "On the Behavior of the Sierpinski Multiband Fractal Antenna". In: *IEEE Transactions on Antennas and Propagation* 46.4 (1998), pp. 517–524.

[68] C. Puente et al. "Small but long Koch fractal monopole". In: *IEEE Electronics Letters* 34.1 (1998), pp. 9–10.

[69] R. Hohlfeld and N. Cohen. "Self-similarity and the geometric requirements for frequency independence in Antennae". In: *Advanced Functional Materials* 7.1 (1999), pp. 79–84.

[70] M. Moskovits. "Surface-enhanced spectroscopy". In: *Review of Modern Physics* 57 (1985), p. 783.

[71] M. I. Stockman et al. "Enhanced Raman scattering by fractal clusters: Scale-invariant theory". In: *Physical Review B* 46 (1992), p. 2821.

[72] A. V. Butenko et al. “Nonlinear optics of metal fractal clusters”. In: *Zeitschrift für Physik D Atoms, Molecules and Clusters* 17 (1990), pp. 283–289.

[73] M. I. Stockman et al. “Comment on: Photon Scanning Tunneling Microscopy Images of Optical Excitations of Fractal Metal Colloid Clusters”. In: *Physical Review Letters* 75.5 (1995), p. 2450.

[74] a. E. C. V. Krachmalnicoff, Y. D. Wilde, and R. Carminati. “Fluctuations of the Local Density of States Probe Localized Surface Plasmons on Disordered Metal Films”. In: *Physical Review Letters* 105.18 (2010), p. 3901.

[75] M. I. Stockman, L. N. Pandey, and T. F. George. “Inhomogeneous localization of polar eigenmodes in fractals”. In: *Physical Review B* 53.5 (1996), pp. 2183–2186.

[76] R. Hohlfeld and N. Cohen. “A Lévy flight for light”. In: *Nature* 453 (2008), pp. 495–498.

[77] M. Burresi et al. “Weak Localization of Light in Superdiffusive Random Systems”. In: *Physical Review Letter* 108 (2012), pp. 79–84.

[78] J. Bertolotti et al. “Engineering Disorder in Superdiffusive Lévy Glasses”. In: *Fractals* 20.6 (2010), pp. 965–968.

[79] D. K. Gramotnev and S. I. Bozhevolnyi. “Plasmonics beyond the diffraction limit”. In: *Nature* 4 (2010), pp. 83–91.

[80] M. I. Stockman et al. “Optical absorption and localization of eigenmodes in disordered clusters”. In: *Physical Review B* 51.1 (1995), pp. 185–185.

[81] M. I. Stockman, S. V. Faleev, and D. J. Bergman. “Localization versus Delocalization of Surface Plasmons in Nanosystems: Can One State Have Both Characteristics?” In: *Physical Review Letters* 87.16 (1995), pp. 7401–1.

[82] M. I. Stockman, S. V. Faleev, and D. J. Bergman. “Viewpoint: A fluctuating fractal nanoworld”. In: *Physical Review Letters* 3.90 (2010), pp. 7401–1.

[83] R. Soneira and P. Peebles. “A computer model universe-Simulation of the nature of the galaxy distribution in the Lick catalog”. In: *The Astronomical Journal* 83 (1978), pp. 845–860.

[84] In: *https://www.astro.rug.nl/ weygaert/tim1publication/lss2007/soneirapeebles.pdf* (2007).

CHAPTER 3

Structural coloration and whiteness in nature: the white beetles

The aspect of the object around us can often be understood through the law of optics, suitable to describe light matter interaction. It is surprising how nature has been able to develop and optimize photonics structures for specific purposes, from which we can learn and be inspired to built artificial optical devices. Some of these bio-photonics structures are found in animals, allowing them to achieve particular color properties exploited in many interaction processes that plays a fundamental role in natural selection. Animals use for example colors as a criterion for sexual selection, for distinction between male and female individuals (sexual dimorphism), for camouflage or, between different species, as a warning sign (aposematic coloration). Some colors act furthermore with a screening functionality, being important for example in thermoregulation. Among these optical structures we considered a specific one, the scale of the white beetle Chyphochilus, where a particular disordered arrangement of submicrometric elements leads to striking optical properties. In this chapter the concept of structural coloration in nature is introduced and the optical properties of the Chyphochilus are presented. A description of previous light transport experiments is reported together with a preliminary study on the dependence of light propagation from scale morphology.

3.1 Structural coloration in nature

Color properties are strongly exploited by animals in many natural processes, playing a fundamental role in the survival of the fittest and representing an influencing factor in the evolution of species. It has been observed that colors are used as a criterion for sexual selection [1, 2], for distinction between male and female individuals (sexual dimorphism) [3, 4], for camouflage [5, 6] or, between different species, as a warning sign (aposematic colouration) [7, 8]. Some colours act furthermore with a screening functionality, being

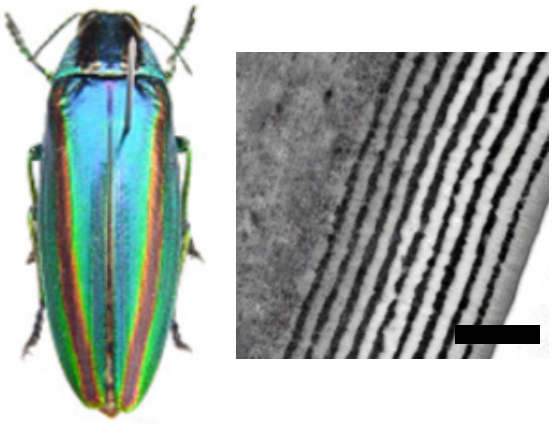

Fig. 3.1: On the left, image of Chrysochroa fulgidissima. On the right, SEM image of the multilayer stack of layers with different refractive index on the insect shell. Scale bar 400 nm. The multilayer acts as a Bragg grating producing constructive interference between the reflected beams obtaining strong spectral selectivity. Image taken from [22].

important for example in thermoregulation [9, 10, 11]. Theses colors can be studied and understood from an optical point of view. Analyzing the interaction of light with micro and nano scale components of the animal body [12, 13], two different mechanisms with different optical processes involved can be distinguished. The first one it is the interaction of light with pigments. In this case, specific frequencies are absorbed and re emitted by the molecules that constitute the pigments and that fully determine the resulting color. The second one, less common but extremely interesting, is the interaction of light with elements on the micro and nano scale that act as photonics structures. As a consequence the color properties arise by fundamental optical phenomena like interference and diffraction, without involving any molecular absorption. The latter mechanism is known as structural coloration [14, 15, 16] and it has been observed and studied in animals of every class, in order to understand how optical structures in nature are optimized for specific tasks. This observation provided also inspiration to design artificial materials exploiting similar strategy to reach comparable optical effects [17, 18, 19, 20, 21]. The smart use of structural coloration adopted by nature has not only the purpose to reach specific colors, but represent also a method to achieve optical properties satisfying also mechanical requirements. An example is the balance between weight and function of photonic structures observed in specific insects, fundamental for flight. It has been observed that brilliant and saturated colors exhibited by many insects, especially in the orders of *Coleoptera* and *Lepidoptera*, are due to the presence on their wings and scales of periodic structures, mostly Bragg reflactors and gratings [23, 24, 25], that, exploiting the band gap due to the modulation of the refractive index, ensure coherent scattering and selection of a narrow frequency interval of the reflected light. One example is the *Chrysochroa fulgidissima* (Figure 3.1), that exhibits a multilayer arrangement in the shell alternating approximately 20 layers with refractive indices of n_1=1.5 and n_2=1.712 [22]. Multilayer stacks of different complexity are the most common structures

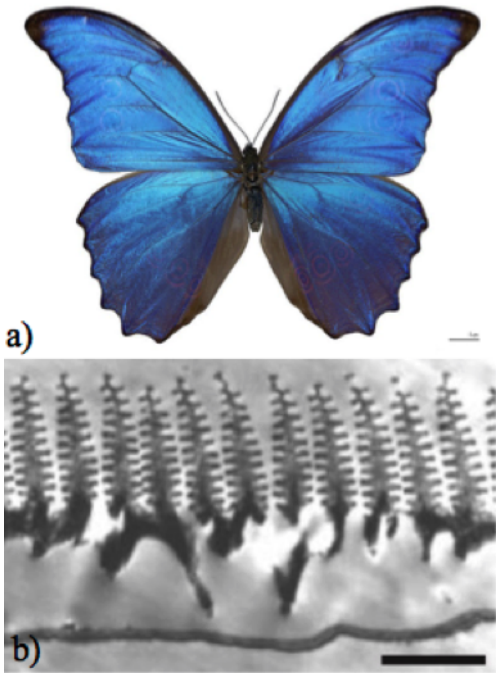

Fig. 3.2: *a*) Image of *Morpho didius*. *b*) Scanning electron microscopy image of the 'Christmas tree'-like periodic pattern on the butterfly wing. Scale bar 1.8 *um*. Image taken from [26].

found in nature to reach this optical effect, but they are not the only. More exotic 1D photonics crystals have been found in several Morpho butterflies exhibiting a strong blue color due to the presence of equally spaces ridges on the micro scale with a 'Christmas tree'-like periodic pattern (Figure 3.2) [26, 27]. The high coherence of the reflected light due the combination of the pattern and the ridges makes the butterfly visible from very long distances. This feature is used by the males to mark the territory and intimidates other rivals looking for female butterflies. Moreover the presence of small irregularities in the ridge distribution due to a random tilt of the single ridges increment the visibility on a wide angular range. This strategy based on combining regularities and irregularities, together with the help of pigments, it is quite common in insects in order to obtain a large angle reflection of the structural color [28, 29, 30].
Higher dimension photonics crystals are as well examples of geometries adopted to reach structural coloration effects. The sea mouse *Aphrodita*, depicted in Figure 3.3a, exhibits irridescent spines with the same distribution of voids of a photonic crystal fiber [31]. In the Scanning Electron Microscope (SEM) image of the spine section in 3.3b is possible to see how hollow cylinders are arranged in an hexagonal closed packed structure with their long axis along the spine. The spine displays brilliant red coloration for normally incident light (Figure 3.3d), but with obliquely incident light the colors shift towards the green and blue (Figure 3.3c). Another significant example of a 2D photonic crystal for structural coloration has been identified in the *Furcifer pardalis*, also known as panther chameleon. The periodic elements responsible of the coloration are guanine nanocrystals embedded in the chameleon cells [33]. A striking feature is the capability of this animal

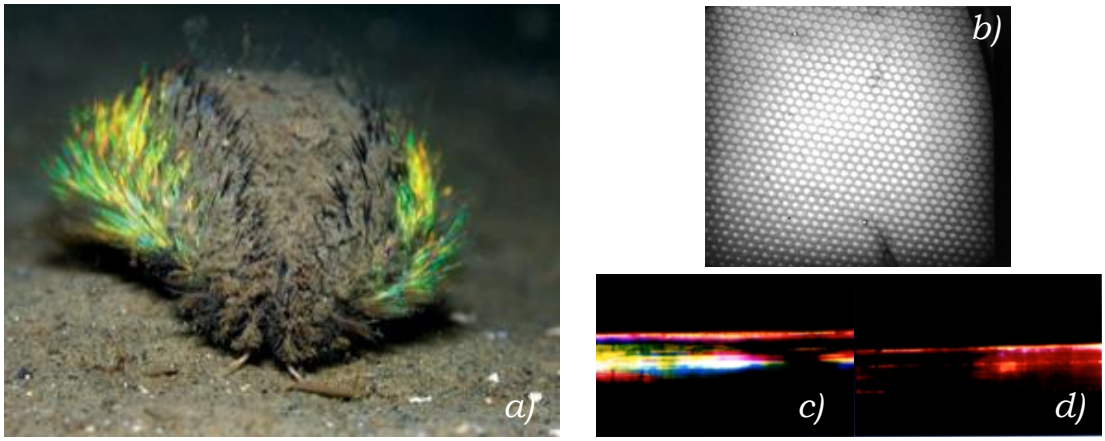

Fig. 3.3: The irridiscent spine of the sea mouse *Aphrodita*. *a*) Picture of the *Aphrodita*. *b*) SEM image of the spine section, revealing an hexagonal closed packed distribution of hollow cylinders in the interior of the spine. Image from taken from[31]. *c*) Bluish and greenish coloration displayed for obliquely incident light [32]. *d*) Red color exhibit by*Aphrodita* spine for normal incident light. Images *c* and *d* taken from [32]

to tune the lattice constant of the nanocrystal pattern changing its overall color either to comouflage or to intimidate the predators. Furthermore this feature potentially provides passive thermal protection.
Despite the previous examples of structural coloration are all based on periodicity, colors in nature are also the result of the interaction of light with disordered arrangements of the microscopic elements. It is well known in the field of optics that the class of random media is made of different types of disorder that result in a wide range of different optical properties. The scattering centers of a system can be distributed in a random fashion but with a certain degree of spatial correlations that induce wavelength dependent costructive interference and thus a frequency dependent transport mean free path. The blue and green colors of many birds feathers are often due to coherence effect in correlated disordered structures [35, 36, 37]. Examples of the structures are reported in Figure 3.5e and f, together with the corresponding diffraction pattern obtained with small angle X-ray scattering (SAXS) measurements (Figure 3.5h and i) [34, 38]. The diffraction pattern, i.e. the Fourier power spectrum of the structures, exhibits ring like fetures that prove the presence of correlation. Moreover they indicate isotropy in the scattering properties that makes the blue color independent from the angle of view, i.e. non-irridescent. This is a fundamental difference from the structural coloration of periodic structures, where the wavelength of the reflected light is angle-dependent. The β-keratine network inside a barb from a blue-grey feather of the *S. lunatus* (Figure 3.5d) rappresents a different strucural coloration strategy that exploit disorder. As it is possible to see from the Fourier spectrum of the structure show in 3.5g, no correlations are present in the system and the transport inside the feather is purely diffusive. The task of the disorder structure here is to "trap" the light in the thin scale increasing the efficient of absorption of the pigments.
So far they have been presented only example of structural coloration optimized to

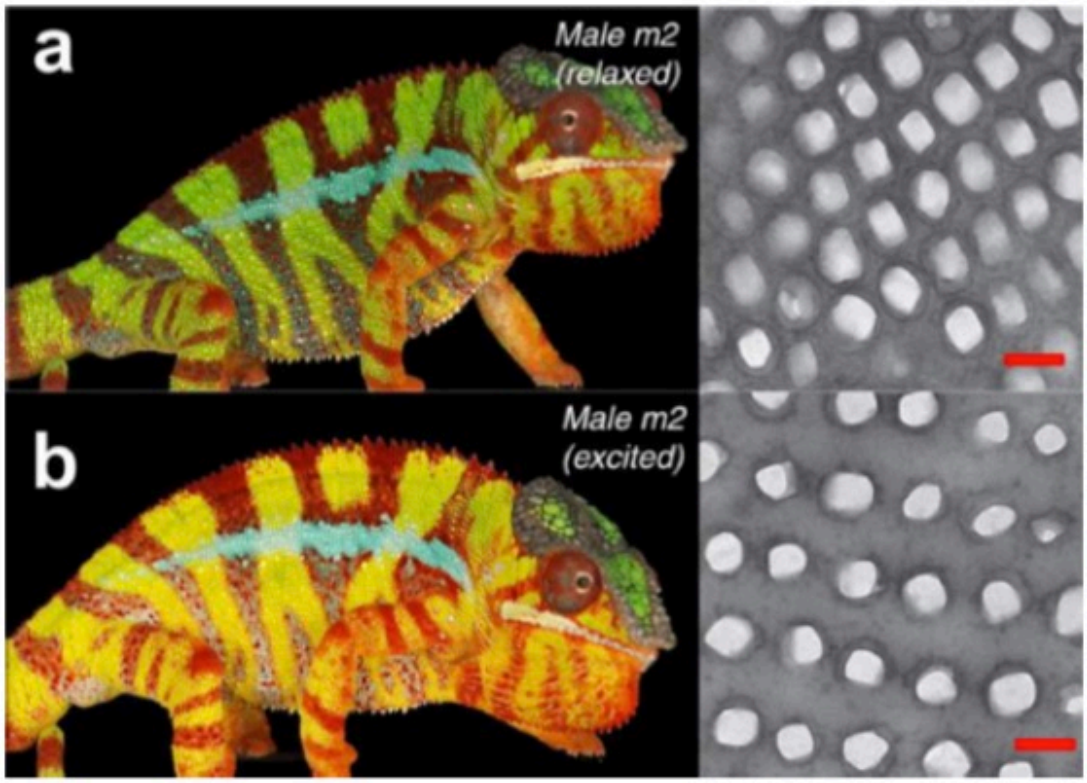

Fig. 3.4: Images of the panther chameleon (*Furcifer pardalis*). *a*) Relaxed; *b*) excited. On the right: TEM micrographs of the guanine nanocrystals contained in the iridophore cells of the chameleon. Scale bars 200 nm. Images modified from [33].

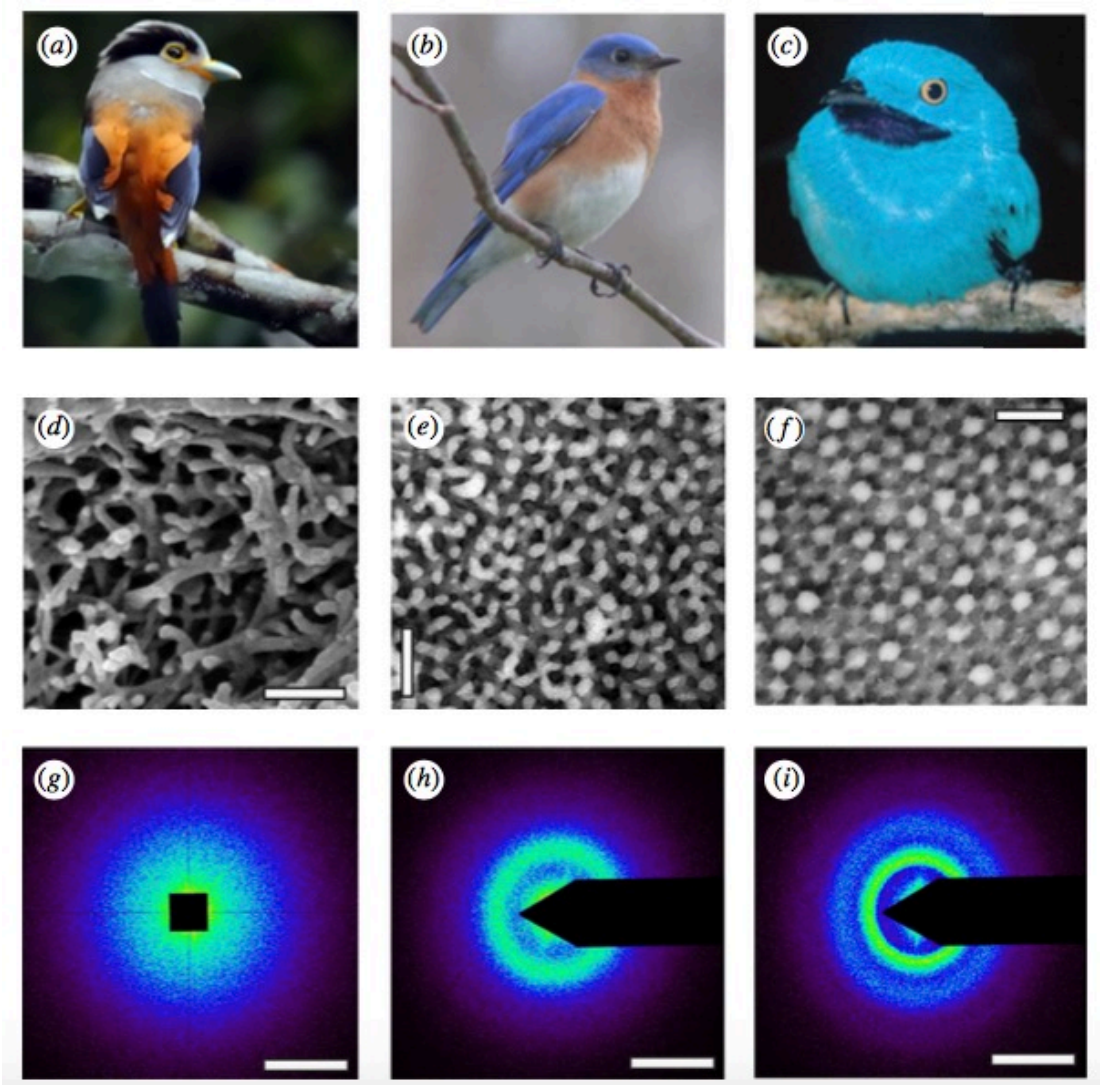

Fig. 3.5: Pictures of (*a*) Female Silver-breasted Broadbill (*Serilophus lunatus*, Eurylaimidae), (*b*) Male Eastern Bluebird (*S. sialis*, Turdidae), (*c*) Male Plum-throated Cotinga (*Cotinga maynana*, Cotingidae). (*d*) SEM image of the β-keratine network inside a barb from a blue-grey feather of the *S. lunatus* (scale bar 250 nm). (*e*) TEM image of the β-keratine network from blue back contour feather barbs of *S. sialis* (scale bar 500 nm). (*f*) TEM image of the sphere-type β-keratin nanostructure from the dark turquoise blue back contour feather barbs of *C. maynana* (scale bar 500 nm) (*g-h-i*) Fourier power spectrum of the structures in *d-e-f* obtained through small angle X-ray scattering (SAXS) (scale bar 0.05 nm^{-1}). The pattern in (*e-f*) reveil the short-range correlation beneath the disorder β-keratin structures while the absence of rings in the pattern (*e*) is the fingerprint of diffusive transport without correlations in the blue feather of *S. lunatus*. All images taken from [34].

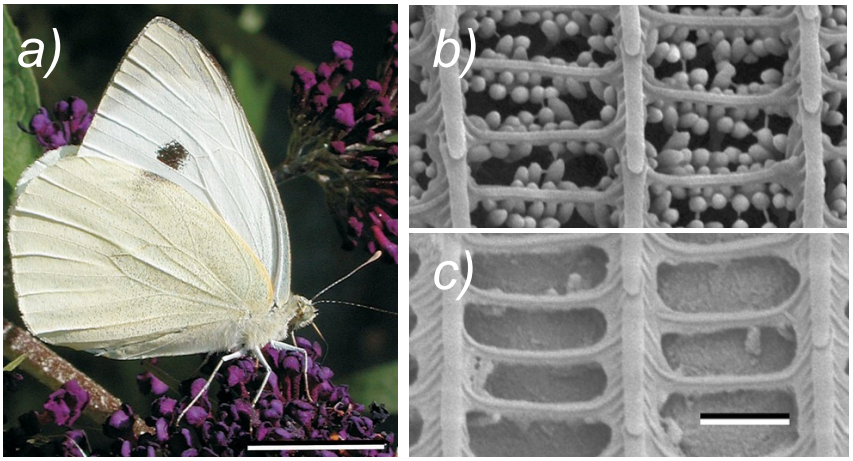

Fig. 3.6: The *Pieris Rapae*. *a*) Image of the white butterfly *Pieris Rapae*. Imahe taken from [39]. *b*) SEM image of the photonic structure embedded in the wing formed by an ordered grid of ridges with a disordered distibution of beads, responsible for the white appearence of the wing. *c*) SEM image of grid in one of the black spots region on the wing. As no beeds are present in the structure, light scattering drammatically decrease and a negligble fraction of the incident light is reflected. Images *b* and *c* taken from [41].

reflect specific wavelength. Anyway nature designed photonic structures also to provide white coloration. This is achieved in systems with no pigments and no correlation, where scattering properties are wavelength independent. An example is the wing of the cabbage butterfly *Pieris Rapae* [39, 40, 41], displaying an ordered net of ridges and crossridges decored with a disorder and dense distribution of beads 3.6. The few black spots on the wings corresponds to scales where the beads are not present and the naked structure made of ridges, characterized by a very low thickness (*ca* 60 *nm*), reflect only a small amount of the incident light. The disordered distribution of beads added to the other scales has the task to increase the scattering strength of the system enhancing the total reflectance. It now worth to explain in deep important physical properties associated to the white coloration. According to our experience white object around us do not appear white in the same way. Assuming that absorption doesn't occur in this systems, the white perceived by the eye depends on two features: whiteness and brightness. A system exhibits high whiteness when its reflectance spectrum tends to be flat in all the visible range while high brightness is the effect due to a high reflectivity. A bright white system is thus characterized by a flat spectral response and a high reflectance, characteristic really difficult to achieve, especially in biological structures where the refractive index is usually low. High scattering strength could in principle be reached in low refractive index systems when thickness is high but, especially for insects, this is a strategy avoided by the evolution as it would cause an unwanted increment of weight. Anyway this trade off between thickness and refractive index did not prevent nature to realize a very thin low refractive index structure with high brightness and high whiteness. This system is the scale of the white beetle *Chyphochilus*.

Fig. 3.7: On the left the beetle *Chyphochilus*, on the right the *Leipidiota stigma*

3.2 The bright white beetles

In this section the system responsible for the striking optical feature of the beetles is presented. Despite the next chapter will be focused on the study of light scattering optimization in the *Chyphochilus*, it worths to mention also the many analogies and the important differences with another white beetle, the *Leipidiota stigma* that presents similar optical properties. Both this insects (Fig. 3.7) are members of the same family (*Scarabaeidae* family) and they live in environment rich of white fungi in south-east Asia [16, 42]. This fact supports the idea that years of evolution leaded this animals to strategically adapt their bright white coloration to the environment for camouflage purposes. Another advantage provided by the white coloration is the thermoregulation. As it's been already observed, white insects are able to forage longer when transferred in a warmer environment [43, 44]. In order to understand the physics behind the white coloration of the beetle, it is necessarily to study the morphology of the micrometric scales that cover its back. The scales of the *Chyphochilus* (Fig. 3.8) are very thin systems, around 7 µm, with an approximated size of 250 µm × 100µm [42]. Those of *Leipidiota stigma* (Fig.3.9) are slighly bigger, showing on average a thickness larger 10 µm and a more elongeted shape with size 450 µm × 150µm. The SEM images of cutted scale cross sections reveil the disorder photonics structures embedded inside the scales of these two animals: a dense random network of chitin filaments (n=1.56) with filling fraction values, i.e. the fraction of the system volume occupied by chitin, in between 0.5 and 0.7 [42, 45]. Each single filament has approximately a diameter of 250 nm in the *Chyphochilus* network and 350 nm in the *Leipidiota stigma*. In Figure 3.10a, a comparison between the two beetles reflectance and the one of other white materials, as a single sheet of paper, polystyrene and the beetle *Calothyrza margaritifera*, is reported [45]. Both *Chyphochilus* and *L. stigma* exhibit a very high degree of whiteness, higher then the one of artificial materials. Moreover they display also a really high reflectivity,

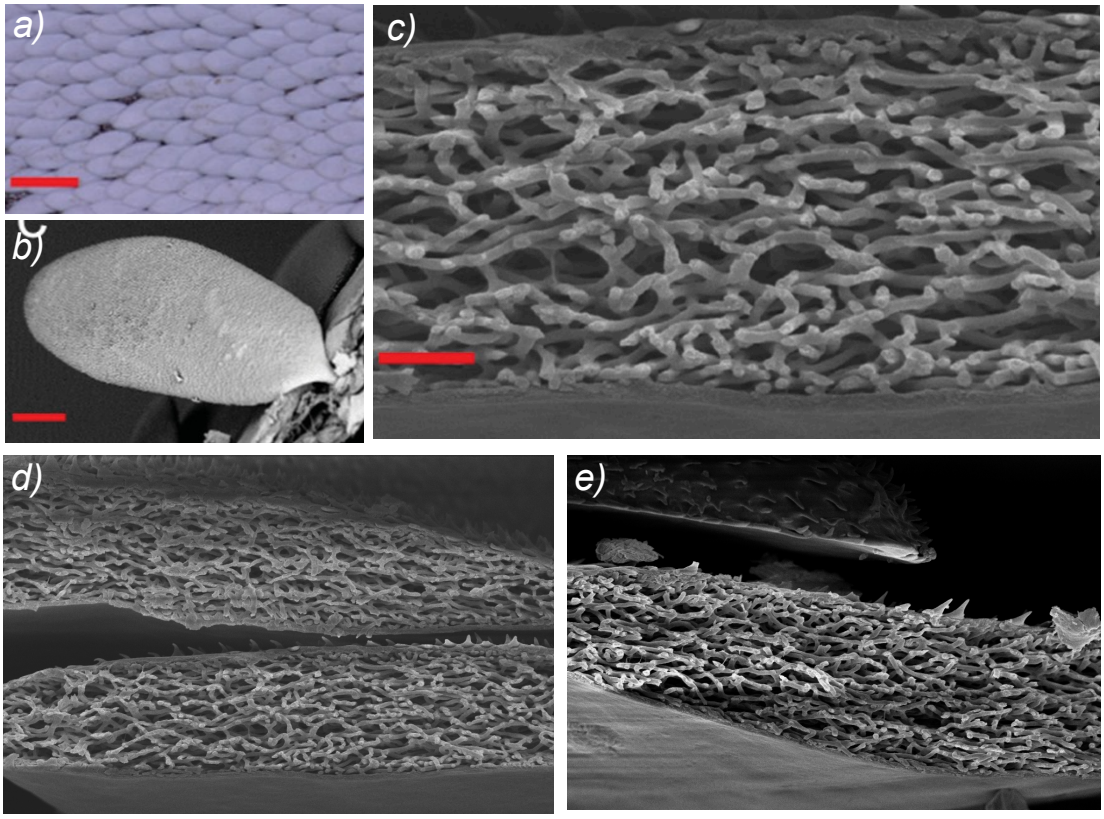

Fig. 3.8: The *Chyphochilus*. *a*) Optical image of the scales of the white beetle *Chyphochilus*. Scale bar 400 µm *b*) SEM image of a single scale of the white beetle *Chyphochilus*. Scale bar 25 µm. *c*-*d*-*e*) SEM image of the chtin random network inside a dissected scale. Scale bars 2 µm.

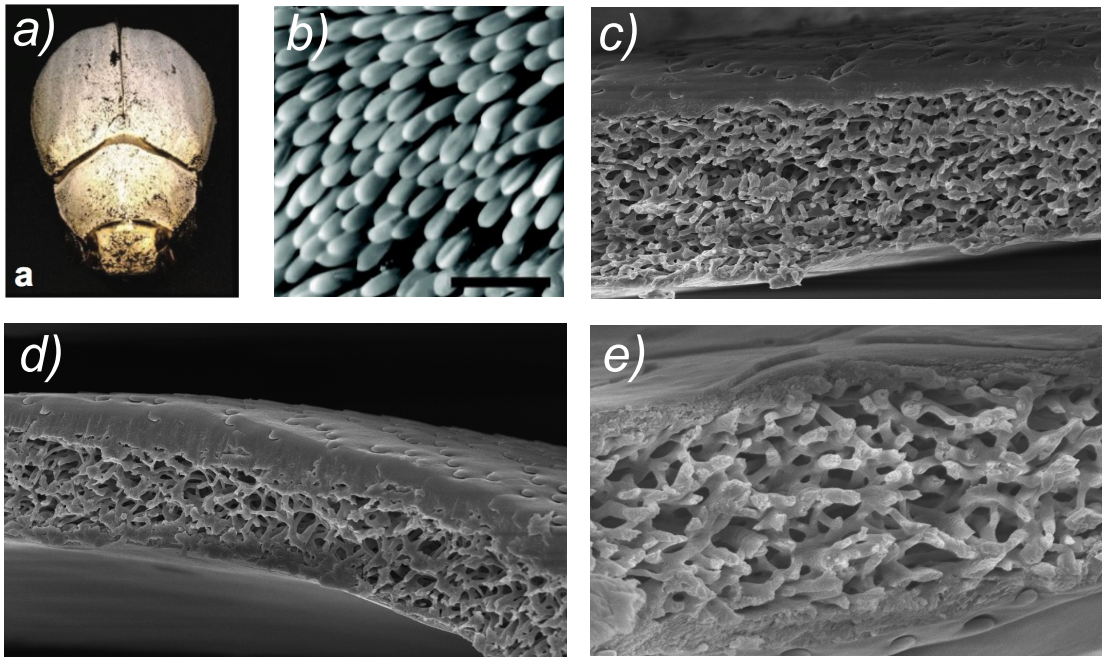

Fig. 3.9: The *Leipidiota stigma*. *a*) Image of the white beetle *Leipidiota stigma*. *b*) Optical microscope image of the scales taken from [45]. Scale bar 500 µm. *c*)-*d*)-*e*) SEM micrograph of a dissected scale. Scale bars 2 µm.

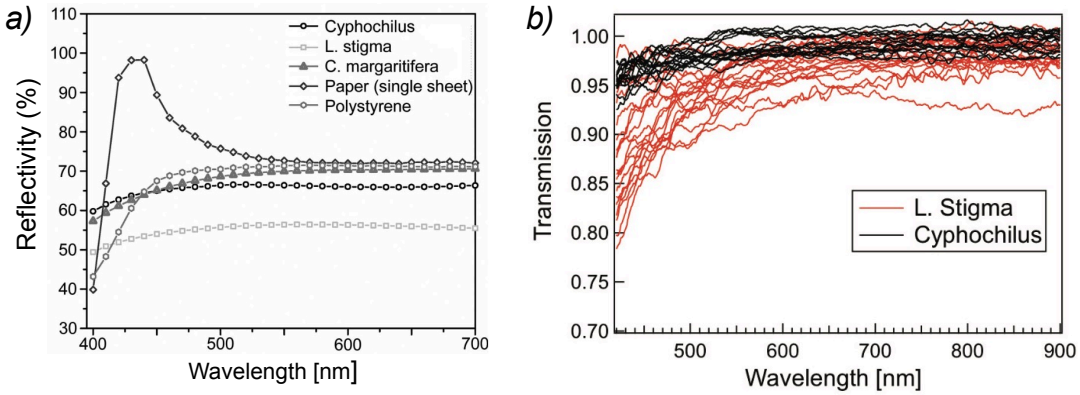

Fig. 3.10: a) Reflectance values for different white systems [45]. The scale of the white beetle *Chyphochilus* is the one that exhibit the most flat response at such low thickness. b) Transmission spectra of the scales infiltrated with index matched oil.

especially the *Chyphochilus* with a 10% higher value than *L. stigma*, that together with the high whiteness makes their scales a unique example of low thickness and low refractive index systems, able to reach enough scattering strength to provide a bright white coloration. In the case of *Chyphochilus*, the brightness at wavelength higher then 500 nm is only 10% smaller then the paper sheet used in the experiment, whom thickness is ten times larger. It is anyway important to point out a difference between the two beetle scales considered here: the absorption. In Fig. 3.10b the transmission spectra of the scales infiltrated with index matched oil shows that *L. stigma* scales absorbs light at all visible frequencies, especially in the blue part of the spectrum, fact that explain the yellowish aspect of the beetle due to the presence of melanine. On the other hand, the light propagating in *Chyphochilus* infiltrated scale exhibits a flat transmission almost equal to 1. For this reason, we will analyze further scattering properties of *Chyphochilus*.

3.3 Multiple scattering in the beetle scales: time-resolved characterization

The exotic optical properties of the chitin random network described in this chapter are a result of the effect of disorder on light transport. A first study of the scale scattering through the physical quantities that characterize the wave propagation in random media has been performed in [46], with the goal of investigating the presence of multiple scattering. The occurrence of multiple scattering inside the chitin network is a non trivial question as, on one side, the system considered displays a low thickness and low refractive index but on the other the white is a property achieved also in single scattering random media. To get insight on this concept, time resolved light transport measurements have been performed to unveil the presence of multiple scattering in order to justify the interpretation of the experimental results with diffusion theory. These measurements have then been combined with a steady state experiment to retrieve the transport mean free path and the filling fraction. The time-resolved measurement are based on a non-linear frequency generation setup. They have been performed impinging along the direction perpendicular to the scale with a probe ultra-fast laser pulse ($\sim$100 fs) at 810 nm. The probe pulse experienced a temporal delay with respect to a reference pulse at 1550 nm due to the scattering inside the scale. Both the transmitted probe pulse and the reference impinge on a non-linear crystal and measuring the variation of delay between them is possible to reconstruct their temporal cross-correlation detecting the sum-frequency signal. In this way it is possible to distinguish the 'early' light, which undergoes only few scattering events, from the 'late' light, characteristic of a multiple scattering process [47, 48]. The so obtained time resolved profiles of the transmitted pulse and reference pulse are reported in Figure 3.11. It is evident from the figure that the interaction of the probe pulse with the beetles scales induces a delay and deformation of the pulse. This effect can be explained as the result of a process of light multiple scattering that light occurs inside the beetles scales. Indeed a single scattering mechanism would lead only to a pulse-peak delay of few fs width (comparable to the ballistic time-of-flight) and to an unmodified pulse shape. On the contrary, the measured delays of the pulses, passed through the samples, are approximately of 80 fs (*Cyphochilus*) and 140 fs (*L. stigma*), and the relative exponential tails are stable over several orders of magnitude. This is a clear fingerprint that light diffuses trapped in

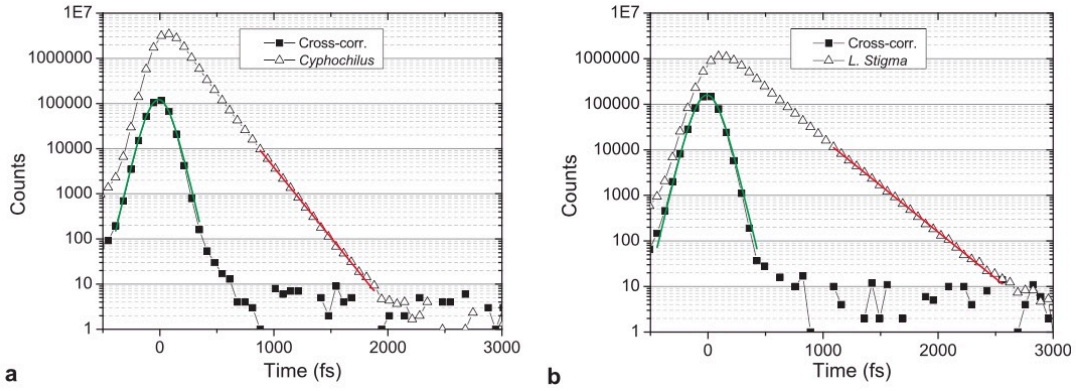

Fig. 3.11: Time-of-flight of light transmitted through the scales of *a*) *Cyphochilus* and *b*) *L. stigma*, respectively (open triangles). The reference measurement (cross-correlation) of the probe pulse is shown as black squares. The fit of the probe pulse (green line) yields a pulse duration of 130 fs. The pulse transmitted through the scales exhibits an exponential tail over three orders of magnitude in intensity. The exponential fit (red line) allows to retrieve lifetimes of $\tau \approx$ 140 fs and $\tau \approx 210$ fs for (a) and (b) respectively. Image taken from [46].

the scales, reemerging at late times. This is quite counter intuitive for such thin and low refractive index systems. According to diffusion theory the exponential-decay time constant is related to the photon lifetime, i.e. the average time spent by light inside the scale. The lifetime has thus been obtained performing a fit of the exponential tails, that gave the value $\tau \approx$140 fs for the *Chyphochilus* and $\tau \approx$210 fs for the *L. stigma*. The static measurement combined with the time-resolved results described above consists of a total transmission acquisition with an integrating sphere. In this experiment the light incident again along the direction perpendicular to the scale is transmitted inside a sphere with perfectly reflective coated interior. All the incoming light is than multiply scattered on the sphere walls. This corresponds to integrate all the input light that passed through the scale and to detect a steady state signal by a sensor placed on an output door of the sphere. Further details about this technique are reported in Chapter 4. The experiment was performed with the same probing condition as in the time-resolved experiment ($\lambda = 810$ nm). Both the beetle scales do not exhibit absorption at the wavelength chosen for the experiment, allowing to retrieve from the total transmitted intensity the system brightness, i.e. the reflectance $R_{tot} = 1 - T_{tot}$. The values obtained for the *Chyphochilus* and the *L. stigma* are $R_{tot} = 0.70$ and $R_{tot} = 0.74$ respectively.

3.3.1 Diffusion theory interpretation

Combining the photon lifetime and the measured total transmission, it has been possible to estimate for the first time the transport mean free path l_t of the systems and to retrieve also the filling fraction f. It is worth to point out that the diffusion approximation (Section 1.2) works very well in diluted systems where the independent scattering approximation, i.e. the assumption that the field exciting a particle is due to the incident field only and not to the field scattered by the other particles, can be applied. In the

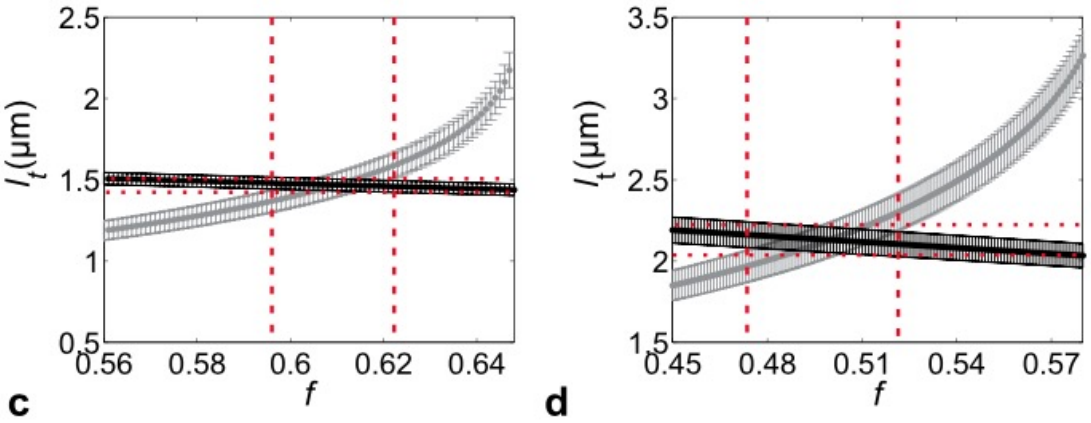

Fig. 3.12: Transport mean free path l_t for fixed thickness and varying filling fraction f for *Cyphochilus* (a) and *L. stigma* (b) scales. The grey symbols correspond to the prediction of Eq. 3.2, the black symbols to the prediction of Eq. 3.3. The crossing points provide the estimates of lt and f, delimited by the dashed red lines.

case of a high packed chitin random network, the density and the arrangement of the scattering centers does not allow to apply the independent scattering approximation. Nevertheless, a high filling fraction system (f>50) in air with index of refraction n is suitable for a diffusive transport description. This can be done considering it as an effective medium with transport velocity $v_e = c/n_e$ where n_e is the effective refractive index [49], related to the n by the Maxwell Garnett mixing rule

$$n_e = n_{air}\left(\frac{1+2f\alpha}{1-f\alpha}\right)^{1/2} \tag{3.1}$$

with $\alpha = (n^2 - n_{air}^2)/(n^2 + n_{air}^2)$. Applying the effective medium approximation and substituting n in the Maxwell Garnett rule with the index of refraction of the chitin n, it is possible to obtain in the diffusive transport case the following expression for the photon lifetime

$$\tau = \frac{(L+2z_e)^2}{\pi^2 D} \tag{3.2}$$

where L is the system thickness, D the diffusive constant (related to l_t by the relation $D = v_e l_t/3$) and z_e the extrapolation length (See subsection 1.3.1), depending on n_e. Combining 3.1 and 3.2 it is possible to determine an expression of $l_t(L,f)_{time}$ as a function of filling fraction and thickness. Measuring the thickness of a scales (*Cyphochilus* L=8.1 µm, *L. stigma* L=13.7 µm) a relation that relates l_t directly to the system f is obtained. Another important consideration on the applicability of the diffusion approximation is the accuracy of l_t calculations in a system with small optical thickness OT defined as $OT = L/l_t$. Previous studies reported $OT > 8$ as the limit required to obtain the maximum accuracy [47, 48], making the diffusion approximation suitable to describe also optically thick dense systems. The accuracy is likely to decrease at lower OT. Despite

	ℓ_t (μm)	D (m^2s^{-1})	OT	OT_n (10^3 $g^{-1}cm^2$)
Cyphochilus	1.47 ± 0.07	112 ± 6	5.5	7.8
L. stigma	2.1 ± 0.1	167 ± 9	6.5	6.7
Paper	13 ± 0.65	1100 ± 55	8.7	1.0
Syringe filter	6 ± 0.3	480 ± 24	27.6	3.7
Photonic Glass	2.9	190	19	5.9

Fig. 3.13: l_t comparison of the beetles scattering strength parameters with those of other white artificial materials. The two beetles display at the same time the shortest l_t and the lowest optical thickness OT, due to the scattering optimization in such thin scales.

the low thickness of the beetle scales, l_t obtained from 3.2 is expected to have a 5% accuracy [50]. The expression 3.2 can be combined with the Ohm's law for light

$$T_{tot} = \frac{l_t + z_e}{L + 2z_e} \tag{3.3}$$

that expresses the total transmission through a diffusive multiple scattering system [51] where the ballistic light constribute has been neglected [46] and that provides another relation $l_t(f)_{static}$. Thus the values τ measured with time-resolved experiment and T_{tot} obtained in the static experiment allow to retrieve $l_t(f)_{time}$ and $l_t(f)_{static}$ from 3.2 and 3.3 and combine them to express l_t and f (Fig. 3.12). The values find are $f = 0.61 \pm 0.02$ and $l_t = (1.47 \pm 0.07)\mu m$ for the *Cyphochilus*, and $f = 0.50 \pm 0.03$ and $l_t = (2.1 \pm 0.1)\mu m$ for the *L. stigma*. The values of the filling fractions result consistent with previously reported values (0.68 ± 0.07 for *Cyphochilus*, 0.48 ± 0.03 for *L. stigma*) [52, 53], feature the corroborate the validity of the experiment and that indicate also a simpler procedure to retrieve f in a diffusive sample without performing imaging or tomography. In Figure 3.13 a table that summarizes the results and compare the l_t of the beetles with those of other white artificial materials is depicted. The random networks embedded in the beetles scale display a scattering strenght that is higher than all the other materials, reaching a value even higher than photonic glass, a material made of polysterene microsphere engineered to maximize scattering efficiency in the visible. It is interesting to note that l_t of the white beetles is at least 6 time lower then the one reported for paper, another well known high density (f ∼0.5) fibrous system made of low refractive index material (cellulose n ∼1.48), but on average ten times thicker. These data indicate that in order to understand the features behind surprising scale scattering strength, a study of the scatterers shape and arrangement is required. This analysis is presented in Chapter 4.3.1 and 5.3.3 for the *Chyphochilus*, the beetle that reaches with a lower average thickness the highest scattering strength. Moreover the lack of absorbance allows a easier modeling of the structure.

References

[1] R. R. Baker and G. A. Parker. “The evolution of bird coloration”. In: *Philosophical Transactions of the Royal Society B: Biological Sciences* 287.1018 (1979), pp. 63–130.

[2] B. D. Wilts et al. “Sparkling feather reflections of a bird-of-paradise explained by finite-difference time-domain modeling.” In: *Proceedings of the National Academy of Sciences* 112.12 (2014), pp. 4363–4368.

[3] Y. Obara and M. E. N. Majerus. “Initial mate recognition in the british cabbage butterfly, pieris rapae rapae.” In: *Zoological Science* 17.6 (2000), pp. 725–730.

[4] Y. Obara and M. E. N. Majerus. “Inaccurate mate recognition as a mating strategy of a ‘pioneer male’.” In: *Proceedings of the Japan Academy. Series B, Physical and Biological Sciences* 85.6 (2009), p. 198.

[5] L. M. Matgher, a. N. J. M. E. J. Denton, and R. T. Hanlon. “Mechanisms and behavioural functions of structural coloration in cephalopods”. In: *J. R. Soc. Interface* 6.Suppl 2 (2009), S149–S163.

[6] B. Wilts et al. “Brilliant camouflage: photonic crystals in the diamond weevil, Entimus imperialis.” In: *Proc. R. Soc. B* 279 (2012), pp. 2524–2530.

[7] T. Guilford. “The evolution of aposematism. Insect defenses: adaptive mechanisms and strategies of prey and predators”. In: *Proceedings of the Japan Academy. Series B, Physical and Biological Sciences* (2009), pp. 23–61.

[8] K. L. Prudic, A. K. Skemp, and D. R. Papaj. “Aposematic coloration, luminance contrast, and the benefits of conspicuousness”. In: *Behavioral Ecology* 18.1 (2007), pp. 41–46.

[9] A. E. Seago et al. “Gold bugs and beyond: a review of iridescence and structural colour mecha- nisms in beetles (Coleoptera).” In: *Journal of the Royal Society Interface* 6.Suppl 2 (2009), S165–S184.

[10] N. F. Hadley, A. Savill, and T. D. Schultz. “Coloration and its thermal consequences in the New Zealand tiger beetle Neocicindela perhispida”. In: *Journal of Thermal Biology* 17.1 (1992), pp. 55–61.

[11] a. M. R. P. Simonis et al. “Radiative contribution to thermal conductance in animal furs and other woolly insulators”. In: *Optics Express* 22.2 (2014), pp. 1940–1951.

[12] P. Vukusic and J. R. Sambles. “Photonic structures in biology”. In: *NAture* 424.6950 (2003), pp. 852–855.

[13] M. Srinivasarao. “Nano-optics in the biological world: beetles, butterflies, birds, and moths.” In: *Nature* 99.7 (1999), pp. 1935–1962.

[14] A. Parker. “515 million years of structural colour”. In: *INFOCOM 2008. The 27th Conference on Computer Communications.* 2.6 (2000), R15–R28.

[15] S. Kinoshita and S. Yoshioka. “Structural colors in nature: the role of regularity and irregularity in the structure”. In: *ChemPhysChem* 6 (2005), pp. 1442–1459.

[16] S. Kinoshita. *Structural colors in the realm of nature*. World Scientific, 2008.

[17] M. Kolle et al. “Mimicking the colourful wing scale structure of the papilio blumei butterfly”. In: *Nature Nanotechnology* 5.7 (2010), pp. 511–515.

[18] C. Mille, E. C. Tyrode, and R. W. Corkery. “Inorganic chiral 3-D photonic crystals with bicontinuous gyroid structure replicated from butterfly wing scales”. In: *Chemical Communications* 47.35 (2011), pp. 9873–9875.

[19] F. Zeighami and M. A. Tehran. “Developing optically efficient nanofiber coatings inspired by Cyphochilus white beetle”. In: *Journal of Industrial Textiles* 46.2 (2015), pp. 495–509.

[20] A. L. Holt et al. “Photosymbiotic giant clams are transformers of solar flux.” In: *Journal of The Royal Society Interface* 11.101 (2014), p. 20140678.

[21] J. Yip, S.-P. Ng, and K. H. Wong. “Brilliant whiteness surfaces from electrospun nanofiber webs.” In: *Textile Research Journal* 79.9 (2009), pp. 771–779.

[22] S. Kinoshita, S. Yoshioka, and J. Miyazaki. “Physics of structural colors”. In: *Reports on progress in physics* 6 (2008), pp. 76401–76500.

[23] H. Tabata et al. “Microstructures and optical properties of scales of butterfly wings”. In: *Opt. Rev.* 3 (1996), pp. 139–145.

[24] H. Ghiradella et al. “Ultraviolet reflection of a male butterfly: interference color caused by thin-layer elaboration of wing scales”. In: *Science* 178 (1972), p. 1214.

[25] A. Huxley. “Theoretical treatment of the reflexion of light by multilayer structures.” In: *J. Exp. Biol.* 48 (1968).

[26] P. Vukusic et al. “Quantified interference and diffraction in single morpho butterfly scales.” In: *Proceedings of the Royal Society of London B: Biological Sciences* 266.1427 (1999), pp. 1403–1411.

[27] W. Wang et al. “Design of a structure with low incident and viewing angle dependence inspired by Morpho butterflies”. In: *Scientific Reports* 3.3427 (2013).

[28] P. Vukusic and I. Hooper. “Directionally controlled fluorescence emission in butterflies.” In: *Science* 310.5751 (2005), p. 1151.

[29] B. D. Wilts et al. “Papiliochrome II pigment reduces the angle dependency of structural wing colouration in nireus group papilionids.” In: *The Journal of Experimental Biology* 215.5 (2012), pp. 796–805.

[30] K. Michielsen and D. G. Stavenga. “Gyroid cuticular structures in butterfly wing scales: biological photonic crystals.” In: *Journal of The Royal Society Interface* 5.18 (2008), pp. 85–94.

[31] A. R. Parker et al. “Photonic engineering: Aphrodite’s iridescence”. In: *Nature* 409 (2001), pp. 36–37.

[32] R. C. McPhedran et al. “The Sea Mouse and the Photonic Crystal”. In: *Australian journal Of Chemistry* 54 (2001), pp. 241–244.

[33] J. Teyssier et al. “Photonic crystals cause active colour change in chameleons”. In: *Nature Communications* 6 (2015), p. 6368.

[34] V. Saranathan et al. "Structure and optical function of amorphous photonic nanostructures from avian feather barbs: a comparative small angle X-ray scattering (SAXS) analysis of 230 bird species". In: *J. R. Soc. Interface* 216.23 (2013), pp. 4358–4364.

[35] H. Yin et al. "Amorphous diamond-structured photonic crystal in the feather barbs of the scarlet macaw". In: *Proceedings of the National Academy of Sciences* 109.27 (2012), pp. 10798–10801.

[36] H. Noh et al. "How noniridescent colors are generated by quasi-ordered structures of bird feathers". In: *Advanced Materials* 22.26-27 (2010), pp. 2871–2880.

[37] J. Tinbergen, B. D. Wilts, and D. G. Stavenga. "Spectral tuning of Amazon parrot feather coloration by psittacofulvin pigments and spongy structures." In: *The Journal of Experimental Biology* 216.23 (2013), pp. 4358–4364.

[38] R. O. Prum et al. "Two-dimensional Fourier analysis of the spongy medullary keratin of structurally coloured feather barbs." In: *Proceedings of the Royal Society of London B: Biological Sciences* 266.1414 (1999), pp. 13–22.

[39] D. G. Stavenga et al. "Butterfly wing colours: scale beads make white pierid wings brighter." In: *Proceedings of the Royal Society of London B: Biological Sciences* 271 (2004), pp. 1577–1584.

[40] B. Wijnen, H. L. Leertouwer, and D. G. Stavenga. "Colors and pterin pigmentation of pierid butterfly wings." In: *Journal of Insect Physiology* 53.12 (2007), pp. 1206–1217.

[41] S. M. Luke, P. Vukusic, and B. Hallam. "Measuring and modelling optical scattering and the colour quality of white pierid butterfly scales." In: *Optics Express* 17.17 (2009), pp. 14729–14743.

[42] P. Vukusic, B. Hallam, and J. Noyes. "Brilliant whiteness in ultrathin beetle scales." In: *Optics Express* 315.5810 (2007), p. 348.

[43] A. E. Seago et al. "Gold bugs and beyond: a review of iridescence and structural colour mecha- nisms in beetles (Coleoptera)." In: *Journal of the Royal Society Interface* 6.Suppl 2 (2009), S165–S184.

[44] N. F. Hadley, A. Savill, and T. D. Schultz. "Coloration and its thermal consequences in the New Zealand tiger beetle Neocicindela perhispida." In: *Journal of Thermal Biology* 17.1 (1992), pp. 55–61.

[45] B. T. H. S. M. Luke and P. Vukusic. "Structural optimization for broadband scattering in several ultra-thin white beetle scales." In: *Applied Optics* 46.22 (2010), pp. 4246–4254.

[46] M. Burresi et al. "Bright-white beetle scales optimise multiple scat- tering of light." In: *Scientific Reports* 4.60075 (2014), pp. 55–61.

[47] R. Elaloufi, R. Carminati, and J.-J. Greffet. "Diffusive-to-ballistic transition in dynamic light transmission through thin scattering slabs: a radiative transfer approach". In: *JOSA A* 21.8 (2004), pp. 1430–1437.

[48] R. H. J. Kop et al. "Observation of anomalous transport of strongly multiple scattered light in thin disordered slabs." In: *Physical Review Letters* 79.22 (1997), p. 4369.

[49] M. P. van Albada et al. "Speed of propagation of classical waves in strongly scattering media." In: *Physical Review Letters* 66.24 (1991), p. 3132.

[50] R. Savo et al. "Walk dimension for light in complex disordered media." In: *Physical Review A* 90.2 (2014), p. 023839.

[51] D. J. Durian. "Influence of boundary reflection and refraction on diffusive photon transport". In: *Physical Review E* 50.2 (1994), p. 857.

[52] P. Vukusic, B. Hallam, and J. Noyes. "Brilliant whiteness in ultrathin beetle scales." In: *Science* 315.21 (2007), pp. 348–348.

[53] S. M. Luke, B. T. Hallam, and P. Vukusic. "Structural optimization for broadband scattering in several ultra-thin white beetle scales." In: *Applied Optics* 49.22 (2010), pp. 4246–4254.

CHAPTER 4

Anisotropic light transport measurements in *Chyphochilus*

Bright white coloration is an optical property that could be achieved exploiting disorder structures that, on the contrary of ordered or spatially correlated systems, manifest the same scattering efficiency for all the visible wavelengths. Moreover high brightness and high whiteness require high system reflectance, almost flat in the visible range. Despite these features are very difficult to achieve in biological disordered media, characterized by low values of the refractive index and thus low scattering strength, the white beetle Chyphochilus manifests a high degree of whiteness and a very high reflectivity. Exploiting a random network of chitin filaments embedded in the interior of its scale diffusion of light occurs, despite the low system thickness, on average 7 μm. The transport mean free path first measured for this system reports a value of $l_t = (1.47 \pm 0.07)\mu m$, lower then the one of artificial highly scattering white materials. Moreover the reflectance of the scales is comparable or slightly smaller with the one of those materials in samples at least ten times bigger then the scale. In the chapter a study of the strategy adopted by the beetle to reach this incredible optical behavior is performed. Addressed by the presence of structural anisotropy in the scale, we carried on an experiment to understand whether the filaments arrangements plays a role in the scattering optimization.

4.1 Structural anisotropy of the chitin network

The high scattering strength of the white beetle *Chyphochilus* scale is investigated, analyzing the filament network morphology to understand the key character of scattering optimization. As it is possible to see from the SEM scale picture 3.8 in the previous chapter and from Figure 4.1, the chitin filaments are not homogeneously distributed in the 3D space and the network appears compressed along the direction perpendicular to the scale. The higher density of filaments along this direction (z-axis) apparently

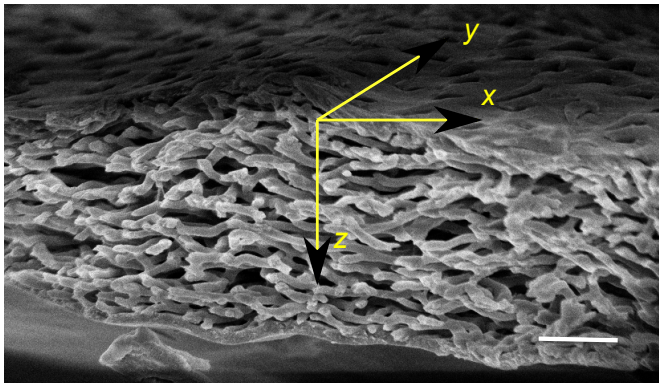

Fig. 4.1: SEM image of the chitin network embedded in the *Chyphochilus* scale. Scale bar 2 µm.

indicate structural anisotropy. Beside the low refractive index, another network feature that is unusual for strong scattering random system is the extremely high filling fraction $f \sim 0.6$. It is well known that the increase f does not lead to an enhancement of the scattering strength, but to an overall decrease due to correlation effect induced by the proximity of scatterers. This effect is named optical crowding [1, 2, 3, 4, 5]. Many experimental works have been done to quantify the possible f values that maximize the scattering strength in different disordered systems but, to our knowledge, values above $f \sim 0.4$ have never been reported. Moreover the scattering properties, for increasing f, show dependence also on the shape of the single scatterers. It is proved that high packing of spherical shape scatterers introduces spatial correlation in the system and thus the scattering strength decreases [6]. On the other hand strongly anisotropic scatterers, like the network filaments, can be packed with high f-values and without spatial correlation only aligning them on average with a planar orientation, thus introducing a certain degree of anisotropy. This feature leads the authors in [7] to interpret the high value of brightness at high filling fraction as a result of both the anisotropic shape of the single scatterers and the network morphology. This fact imposes the scattering elements to be connected, reducing the contact surfaces between them (i.e. connected only at the extremities) and preventing the occurrence of optical crowding. In order to understand if these structural features affect light transport in the scale, and thus understand if anisotropy is the mechanism behind the brightness optimization, optical measurement have been performed, investigating the dependence of transport by the direction of propagation. More considerations on the role of anisotropy in the scale, together with modeling and simulations, are the subject of Chapter 5.

4.2 Light transport measurements

To investigate the occurrence of anisotropic light transport inside the chitin random network of the *Chyphochilus*, we adopted a strategy similar to the one described in 3.3, combining independent experiments to estimate l_t. We performed two static experiments: a total transmission measurement and an imaging measurement of the diffused profile transmitted through the scale. According to diffusion theory the optical thickness

$OT = L/l_t$ of a non absorbing slab geometric system can be retrieved from the total transmission that, knowing the physical thickness, gives l_t. In the case of anisotropic diffusion this procedure is still valid, but the values so obtained correspond to l_t value along the incident beam direction only (z direction). Considering the shape of the scale, it is thus reasonable to model it as a slab with finite size in the direction perpendicular to it (the z-axis in Fig. 4.1), and to estimate by a total transmission T_{tot} measurement along z-axis the value $l_{t,z}$. On other hand the transmitted intensity distribution in the x-y plane $T(x, y)$ of the anisotropic slab is dependent on $l_{t,x}$ and $l_{t,y}$, but also on the transport properties along z. Thus in an anisotropic diffusive picture, $l_{t,z}$ is a necessary quantity to interpret correctly $T(x, y)$, that can be measured imaging the light on the output surface of the scale. Combining the imaging and the total transmission measurement is thus possible to take further the analysis of l_t in [7] and determine its values in the three directions $l_{t,x}$, $l_{t,y}$ and $l_{t,z}$.

4.2.1 Experimental setup

For both the static experiment performed, the same source has been employed, a Fianium Femtopower 1060 supercontinuum laser. It is a high-power fibre laser generating ultrabroadband supercontinuum radiation. The supercontinuum generation occurs when a high power pump femtosecond laser is injected in a non-linear photonic crystal optical fibre. After the non-linear process the pulse spectrally broadens, covering a wide range of wavelengths. The emission ranges from 390 nm to 2400 nm, the average integrated output power is 4 W. The output beam hs been polarized linearly and, to perform the experiment at a specific wavelength, the white light has been filtered with a band pass filter of 550 nm and $\Delta\lambda = 10$ nm (as we will discuss later in Chapter 5, the relatively broadband filter is necessary to reduce the speckle effects in the spatial profile). This specific wavelength has been chosen in order to avoid absorption in the system (absorption spectra are reported at section 3.2).

Total transmission measurements setup

A schematic rappresentation of the setup assembled to perform the total transmission measurement is depicted in 4.2. Light exiting from the source, after being spectrally filtered, is temporally modulated at a frequency of 80 Hz using a chopper. Then it is focused on the sample with an aspheric lens. The focal spot diameter is between 1.5 µm and 2 µm. The diffusive sample is fixed on a neutral density (ND) filter at the entrance port of the integrating sphere (Newport 819C). This is necessary to prevent the contribution of reflection from the sample to the background light. The use of an integrating sphere for total reflectance and transmittance measurements of a diffusive system is a well established technique, often used in the last decades [8, 9, 10]. An integrating sphere (represented inside the setup in Fig. 4.2) is a hollow spherical cavity which interior is covered by a 'perfectly' diffusive (Lambertian) white coating. There are entrance ports for the input light beam and output ports for detectors. The function of the sphere is to spatially integrate radiant flux. All the light incident on the input port is collected inside the sphere, multiply scattered by the diffusive coating and eventually distributed over all angles. The light flux becomes very uniform at the detector port, and ideally independent of the spatial and polarization properties of the introduced light.

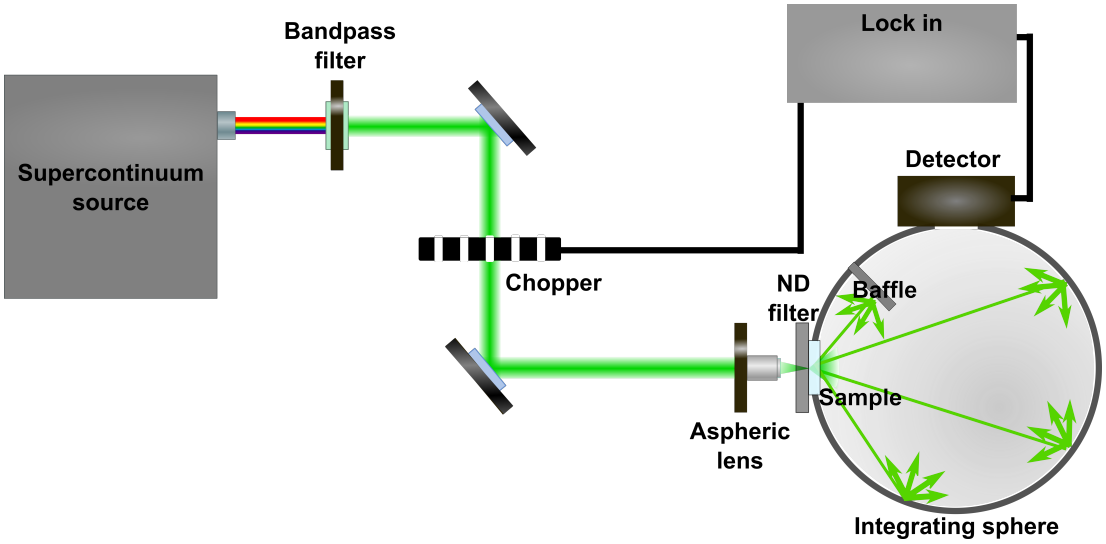

Fig. 4.2: Scheme of the experimental setup for total transmission measurements

To prevent light from going directly from a source port to a detector port, diffusive baffles are usually inserted between the two ports. In this way the detected optical power depends only on the total introduced power. For an exhaustive dissertation on integrating sphere theory and applications the reader can refer to [11, 12]. Through a micrometric precision 3D translation stage it is possible to move the sample, controlling its position with respect to the optical axis of the beam. The transmission at the output of the sphere is detected using a silicon photodiode combined with a lock-in amplifier in order to reduce the background light from the environment.

Imaging of the spatial transmission profile setup

The setup used for the imaging experiments reported in this thesis is schematically depicted in Figure 4.3. Once the light emitted from the supercontinuum source is filtered to select the wavelength, the polarization of the light (linear or circular) incident on the sample can be selected with the polariser P1 and the quarter waveplate P2. The beam is focused on the sample with an aspheric lens with high NA in order to have a spot size in the front surface of the sample of only 1.5 µm. A small spot in the sample is necessary in order to approach the hypothesis for the solution of the diffusion equation. As it will be explained more in deep in 4.2.3, according to diffusion theory, transmission profile through a slab exhibits a bell-shape, with FWHM of the order of the sample thickness, barely affected by the transport properties. However, the exponential tails of such profile depend mostly on l_t. Thus accurate spatial measurements, with proper background subtraction and reduction of aberrations, can be used to infer the transport properties of the beetle scales. The imaging part of the setup is composed by an infinity corrected objective, a tube lens and a CCD camera. The infinity corrected objective (Olympus 20X NA = 0.40), combined with the appropriate tube lens (focal length 180 mm), is necessary to reduce the spherical aberrations that could affect the determination of the transport mean free path in the fit procedure. The image of the light transmitted on the

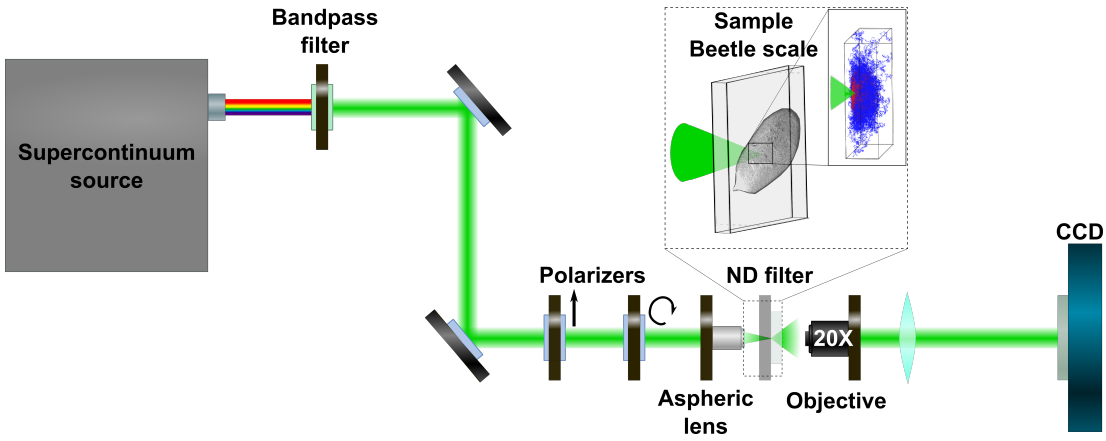

Fig. 4.3: Scheme of the experimental setup for imaging measurements of the diffused transmitted profile through the beetle scale.

rear surface of the sample is collected in a Apogee Alta 2000 CCD camera, with a 1600 × 1200 pixels matrix, cooled at a temperature of T = -20°C to reduce the electronic noise.

4.2.2 Total transmission

The setup described in paragraph 4.2.1 have been used to perform measurements of the light diffused and transmitted through the scale. In order to collect data suitable for a diffusion theory interpretation, valid for slab systems as explained at the beginning of the section, the experiment has been operates focusing the beam on the central part of the scale, orthogonal to its surface. In this way it has possible to neglect the smooth curvature of the sample at the edges, fulfilling the geometry conditions. The measurements have been repeated impinging on different points inside this small area in the scale center to collect statistics. The value obtained is $T_{tot} = 0.29 \pm 0.02$. As the measured value is the result of multiple scattering with negligible ballistic contribute [7], the diffused total transmission can be expressed with the Ohm's law for light

$$T_{tot} = \frac{l_t + z_e}{L + 2z_e} = \frac{1 + \frac{2}{3}A}{OT + \frac{4}{3}A}. \tag{4.1}$$

where $z_e = 2Al_t/3$ is the extrapolation length and A the coefficient that takes into account the internal reflection due to the refractive index mismatch with the environment (it depends on the effective refractive index n_e, see section 1.3.1 for further details). A has been calculated as done by the group in [7], applying Maxwell Garnett mixing rule with a filling fraction of 0.61 to calculate the average refractive index of the scale. This assumption is reasonable due to the fact that the scales used in the experiment proposed here come from the same region of the same beetle elytron. Inserting in 4.2 the measured value of the measured value of T_{tot} and the computed value of A a value of $OT = 5.8 \pm 0.7$ has been obtained. To finally determine l_t, a measure of the scale thickness is required. An evaluation of the thickness through SEM image requires a dissection of the scale, making the sample not suitable for future analysis. Therefore a

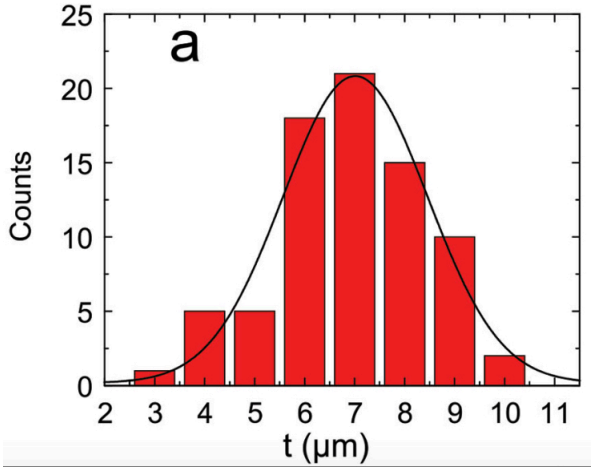

Fig. 4.4: Histrogram of the measured thicknesses of the 80 beetle scales. The black curve represents a Gaussian fit. The average value of the distribution is approximately 7 µm.

different strategy have been adopted, acquiring images of 80 other scales of the same beetle, gently dissected with a razor blade, determining the thickness distribution. In Figure 4.4 is reported the retrieved histogram of the measured thicknesses, fitted with a Gaussian function. Th average scale thickness obtained is 7 µm, with a standard deviation $\sigma = 1.5$ µm.

4.2.3 Imaging measurement of transmitted profile

The second part of the experiment has been performed exploiting the imaging technique described in 4.2.1. In Figure 4.5 is reported the geometric sketch of the experiment (a), together with an example of an acquired image (b): the laser beam has been focused on the front side of the scale, and the spatial transmission profile $T(x, y)$ on the rear side has been imaged on the CCD camera; the image plane is parallel to the xy plane, and the beam direction to the z axis. The beam impinged in the central part of the scale (the same investigated with total transmission measurements), and, moving the sample respect to the beam axis, we investigated a region of approximately 40 µm radius centered in the initial beam focus, acquiring 20 different images and processing the average to get the profile. The choice of this region is again motivated by the requirement to perform measurements not affected by the scale curvature in order to approximate the system to a slab. Collecting many images, together with the choice of a relatively broadband source ($\Delta\lambda = 10$ nm), has a precise scope. Besides the accuracy of the statistical analysis, changing the focus position, that in a statistical homogeneously random media corresponds to replicate the measurement for a different realization of disorder, reduces the speckle pattern contribution, smoothing the profile and reveling the diffusive transport fingerprint. The benefits of this procedure can be appreciated in Figure 4.6. In a) a profile from a single acquisition is reported, while (b) display an example of image after averaging and background subtraction. The crosscut of the profiles in (a), black line and (b), red line, are reported in the graphs (c) and (d) in

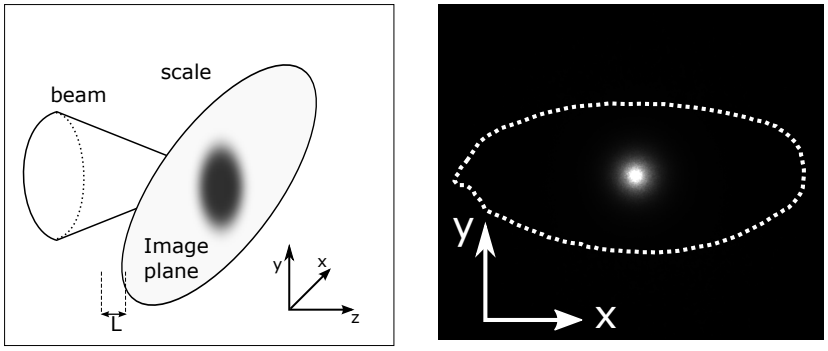

Fig. 4.5: On the left, geometric sketch of the experiment. On the right, an actual image of the spatial profile of the light transmitted through the scale as acquired by the camera. The dashed line is the contour of the scale.

linear and semilog scale. Coherent effects, i.e. speckles, and background make the signal fluctuating (evident in linear scale), 'hiding' the exponential tails of the profile (evident in semi-log scale) which behavior depends on l_t. Averaging on more disorder realizations and subtracting the background allow to retrieve a smooth signal decaying exponentially over more than two orders of magnitudes, suitable to detect the dependency by l_t.

4.3 Results

In order to study if the structural anisotropy actually affects the light transport in the scale, the profiles obtained in the imaging experiment (Figure 4.6 (e) and (f)) have been first compared with the prediction of isotropic diffusion theory for a slab system (Equation 1.53) with the same OT measured in the total transmission experiment. The physical thickness adopted in the calculation has been chosen according to the statistical analysis performed and described in 4.2.2, considering values in the 2σ range with respect to the center of the Gaussian distribution (Figure 4.4). This analysis, reported in Figure 4.7 (a), clearly demonstrates the discrepancy between the measured profile and the prediction of isotropic diffusion theory. The appropriateness of isotropic diffusion to describe light transport in such a thin system must be evaluated, since its accuracy rapidly decreases for OT < 10 [13]. Therefore we performed isotropic Monte Carlo simulations for a disordered slab with OT $= 5.8$ and the same effective refractive index of the scale. Figure 4.7b) shows the simulated isotropic profile with an isotropic diffusion theory fit of the profile tail. Despite the low optical thickness the transport parameters are retrieved within an accuracy better than 1%, as long as the central points of the profile are excluded. This is necessary since ballistic and low order scattered light, which have a dominant contribution to the peak of the transmission profile in thin slabs, are not taken into account in the diffusion approximation [14]. We conclude that the large discrepancy shown in Figure 4.7a) is not due to a possible breakdown of diffusion theory, but must be caused by the very nature of light transport in the scale (i.e. transport is not isotropic).

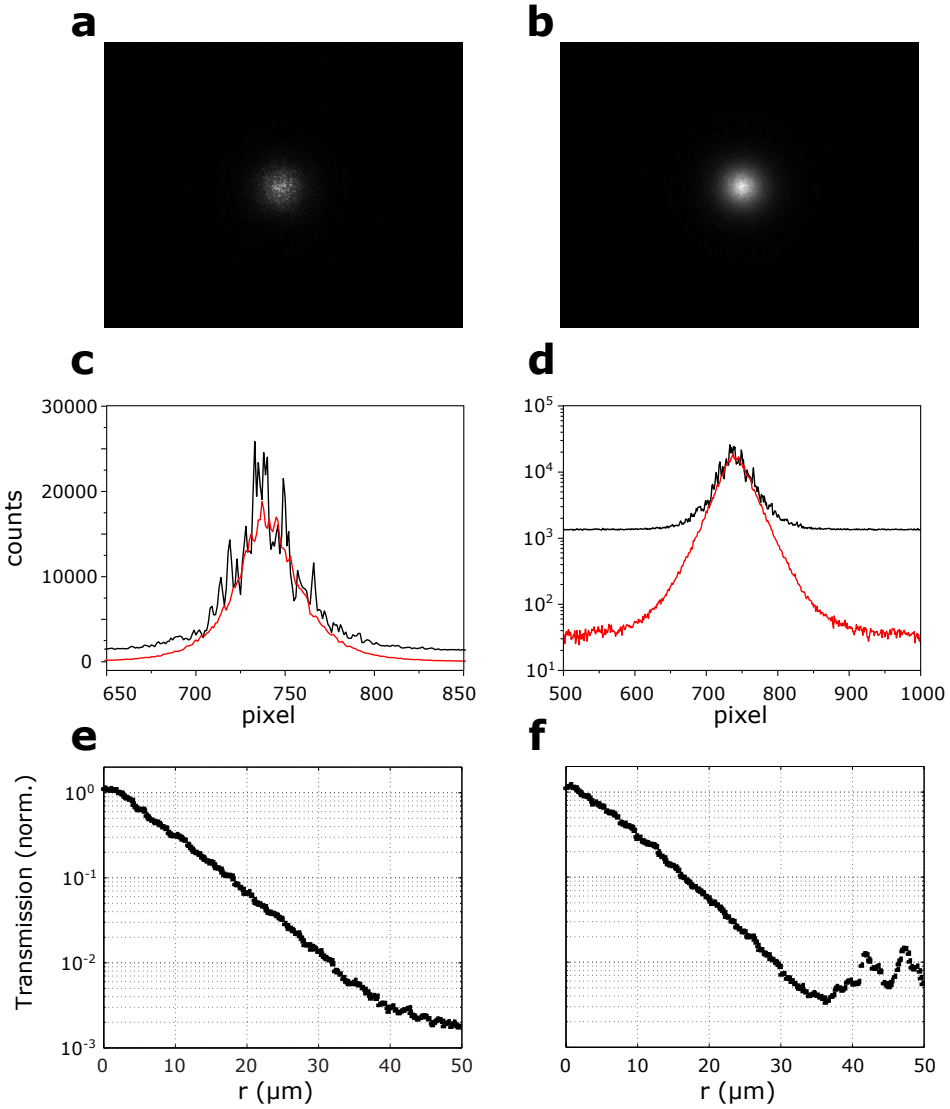

Fig. 4.6: Imaging of the spatial transmission profile through a scale. (a) Image of a single acquisition of the CCD camera. (b) Average of 20 different acquisitions with background subtracted. (c) and (d) Horizontal crosscuts of (a), black lines, and (b), red lines, in linear and semi-logarithmic scale. Images (e) and (f) report crosscuts, along x and y axis respectively, of the profile relative to the reference scale; to further smooth the speckles, the 'bell shaped' profile has been folded with respect to its symmetry axis and averaged again.

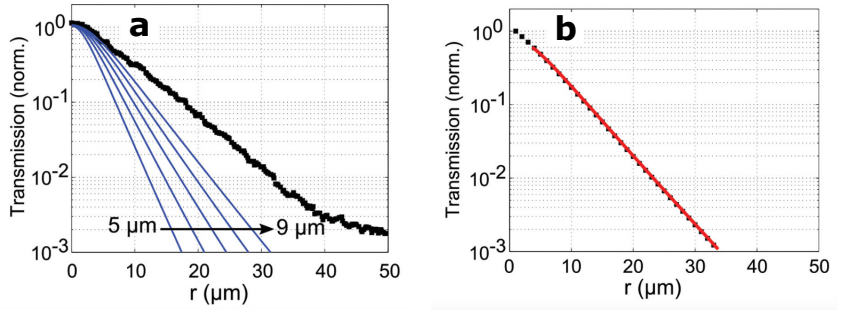

Fig. 4.7: Isotropic diffusion theory interpretation. *a*) The black points represent the crosscut along the x axis of the spatial transmission profile (experimental data). The blue lines are the prediction of isotropic diffusion equation for OT = 5.8 and increasing thickness, from $L = 5\,\mu m$ to $L = 9\,\mu m$, corresponding to a 2σ range with respect to the center of the distribution (Figure 4.4). *b*) The black dots indicate a Monte Carlo simulated spatial profile of an isotropic sample with OT = 5.8. The red line is the isotropic diffusion equation fit.

4.3.1 Interpration through anisotropic diffusion theory

Since isotropic diffusion theory does not provide reasonable results, although the OT is such that it should work reliably, the transmission profile of the scale has been fitted using the anisotropic diffusion equation, which, in a slab configuration, links the static profile of diffuse light emerging from the outer surface of a diffusive medium with the diagonal elements of the diffusion tensor and its thickness. In this framework, the steady-state spatial transmission profile through a non absorbing slab of thickness t, is given by [15]:

$$T(x,y) = \frac{1}{4\pi\sqrt{D'_x D'_y D'_z}} \times \sum_{n=-\infty}^{\infty} (L - z_{1,n})\left(\frac{x^2}{D'_x} + \frac{y^2}{D'_y} + \frac{(L-z_{1,n})^2}{D'_z}\right)^{-3/2} - (L - z_{2,n})\left(\frac{x^2}{D'_x} + \frac{y^2}{D'_y} + \frac{(L-z_{2,n})^2}{D'_z}\right)^{-3/2} \tag{4.2}$$

where $z_{1,n} = 2ntL + 4nz_e + l_{t,z}$, $z_{2,n} = 2nL + (4n-2)z_e - l_{t,z}$, and we assume a direct relationship between the diffusion tensor and the transport mean free path, $D_i = D'_i v_e = 1/3 l_{t,i} v_e$ (see Chapter 1). As already pointed out, in the case of anisotropic transport, the Ohm's law is still valid, provided that l_t in Equation 4.2 is replaced with the transport mean free path along the direction orthogonal to the scale surface ($l_{t,z}$ with the notations of Figure 4.5). Hence, to increase the brightness is only necessary to decrease the mean free path along the z-direction, regardless of the in-plane properties. Even in the anisotropic diffusion approximation, we can still define the optical thickness as $OT = L/l_{tz}$ and determine it experimentally. As before, we considered a set of $l_{t,z} = L/OT$ values, keeping $OT = 5.8$ constant and varying L in a 2σ range with respect to the centre of the measured distribution. Then we performed fits of crosscuts along the

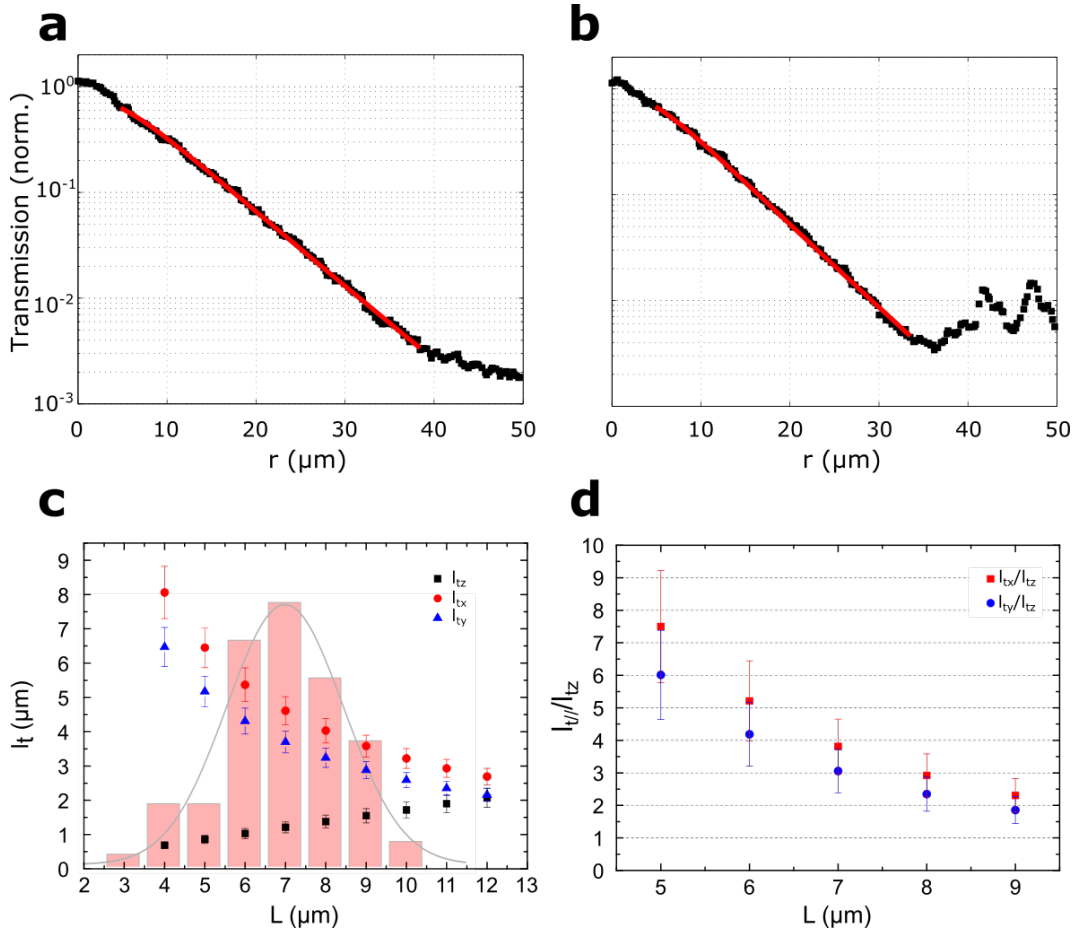

Fig. 4.8: Anisotropic diffusion theory interpretation. a) The dots in the graph represent intensity crosscuts of the imaged transmitted profile (experimental data) along a) x and b) y. The red line are the respectively anisotropic diffusion equation fits. c) Values of l_t along the three different axes obtained fitting the transmission profiles with the anisotropic diffusion equation for fixed values of thickness, chosen in a range compatible with the actual size of the scales. The graph is overlapped with the thickness distribution. d) Ratio between l_t in the plane of the scale surface and l_t perpendicular to the scale surface. The results are displayed only for values of thickness in a range of 2σ with respect to the center of the distribution.

$L(\mu m)$	$l_{tz}(\mu m)$	$l_{tx}(\mu m)$	$l_{ty}(\mu m)$
4	0.69 ± 0.09	8.02 ± 0.76	6.47 ± 0.57
5	0.86 ± 0.12	6.45 ± 0.58	5.18 ± 0.45
6	1.03 ± 0.15	5.37 ± 0.49	4.31 ± 0.38
7	1.21 ± 0.16	4.61 ± 0.41	3.70 ± 0.32
8	1.38 ± 0.19	4.03 ± 0.36	3.24 ± 0.28
9	1.55 ± 0.21	3.58 ± 0.32	2.88 ± 0.25
10	1.72 ± 0.24	3.22 ± 0.29	2.59 ± 0.22
11	1.90 ± 0.26	2.93 ± 0.26	2.35 ± 0.21
12	2.07 ± 0.28	2.69 ± 0.24	2.16 ± 0.19

Fig. 4.9: Transport mean free path along the three directions. The values have been retrieved from the experimental data considering possible values of the scale thickness scale determined by the statistical analysis described in subsection 4.2.2.

x and y axes of the imaged transmission profile using the anisotropic diffusion equation, with, respectively, $l_{t,x}$ or $l_{t,y}$ as the only fitting parameter. Examples of anisotropic fits are reported in Figure 4.8a) and b), respectively for crosscuts along the x and y axes. The results of the fits for different thicknesses are reported in the table depicted in Figure 4.9, and are plotted in Figure 4.8c) and d). We found that $l_{t,x}$ and $l_{t,y}$ are always appreciably larger than $l_{t,z}$. For thickness inside an interval larger than 2σ with respect to the center of the distribution the ratio between $l_{t,//}$ and $l_{t,z}$ lays between 7 and 2. The plotted data suggest as well that $l_{t,x}$ (transport along the long axis of the scale) is slightly bigger than $l_{t,y}$ (short axis). This implies an in-plane anisotropy which seems to be plausible since the 'growth' direction of the scales is along the x axis. However, we can not make any definitive statement on the subject since the scales have a more pronounced curvature along the y-direction and this might create some reshaping in the transmitted profile. In contrast, the z-direction anisotropy of light transport is clearly evident, demonstrating that the anisotropy of the intra-scale structure is the strategy adopted to pack efficiently the dense network in the thin scale, in order to optimize the scattering along the direction normal to the scale surface. This feature necessarily introduces a larger in-plane transport mean free path, which however does not contribute to the brightness. The reason behind the evolution of a system with such features is probably the need of the *Chyphochilus* to maximize the brightness keeping the weight low. An increase of the scale thickness would as well lead to an increase of the brightness, but such a high reflectance would require a higher amount of chitin, increasing the weight of each single scale. On the other hand, an anisotropic arrangement of the scatterers, i.e. introducing angular correlation in the network geometry, avoids the appearance of spatial correlations and selectively enhances the scattering strength in the normal direction. Light scattering is therefore optimized using as little material as possible within the thinnest possible system, and fulfilling in the white beetle the scattering conditions required to appear white and succeed to fly. The results shown in this Chapter can be considered also for technological applications [16, 17, 18]. The internal structure of the scales can indeed be taken as inspiration in developing new materials with high diffuse reflectivity and low thickness. In fact the performances of Light Emitting Diodes (LEDs) and displays can be improved introducing beetle-inspired ultrathin diffuse reflector layers.

Moreover, optimizing angular correlations (i.e. the anisotropy) in network-like optical materials seems still a large unexplored strategy in many applications. Considering for example the recently growing field of cellulose photonics, it is well known that for highly packed systems, moving from micrometric fibers (like common paper) to sub-µm fibrils leads to increased transparency [19, 20, 21]. On the contrary, we demonstrated that an optical system with analogue high density and low refractive index can exhibit an exceptional turbidity even with submicrometer scatterers, provided that its geometry is properly optimized. To further explore geometrical requirements of such anisotropic fashion, a computational study on how angular correlations affect the reflectance of a network of low-refractive-index rods is proposed in the following Chapter.

References

[1] M. K. Gunde and Z. C. Orel. "Absorption and scattering of light by pigment particles in solar-absorbing paints." In: *Applied Optics* 39.4 (2000), pp. 622–628.

[2] B. L. Drolen and C. L. Tien. "Independent and dependent scattering in packed-sphere systems." In: *Journal of Thermophysics and Heat Transfer* 1.1 (1987), pp. 63–68.

[3] L. E. McNeil and R. H. French. "Multiple scattering from rutile TiO2 particles". In: *Acta Materialia* 48.18 (2000), pp. 4571–4576.

[4] R. R. Naraghi et al. "Near-field effects in mesoscopic light transport." In: *Physical Review Letters* 115.20 (2015), p. 203903.

[5] J.-C. Auger, V. A. Martinez, and B. Stout. "Theoretical study of the scattering efficiency of rutile titanium dioxide pigments as a function of their spatial dispersion." In: *Journal of Coatings Technology and Research* 6.1 (2009), pp. 89–97.

[6] L. F. Rojas-Ochoa et al. "Photonic properties of strongly correlated colloidal liquids." In: *Physical Review Letters* 93 (2004), p. 073903.

[7] M. Burresi et al. "Bright-white beetle scales optimise multiple scat- tering of light." In: *Scientific Reports* 4.60075 (2014), pp. 55–61.

[8] D. K. Edwards et al. "Integrating sphere for imperfectly diffuse samples." In: *Journal of the Optical Society of America* 51.11 (1961), pp. 1279–1288.

[9] J. W. Pickering et al. "Double-integrating- sphere system for measuring the optical properties of tissue." In: *Applied Optics* 32.4 (1993), pp. 399–410.

[10] J. F. Beek et al. "In vitro double-integrating-sphere optical properties of tissues between 630 and 1064 nm." In: *Physics in Medicine and Biology* 42.11 (1997), p. 2255.

[11] J. M. Palmer and B. J. Grant. *The Art of Radiometry.* SPIE Press, 2010.

[12] H. K. H. III and H. L. Mason. *Precision Measurements and Calibration: Selected NBS Papers on Radiometry and Photometry.* NBS Special Publication, 1971.

[13] R. Elaloufi, R. Carminati, and J.-J. Greffet. "Diffusive-to-ballistic transition in dynamic light transmission through thin scattering slabs: a radiative transfer approach". In: *JOSA A* 21.8 (2004), pp. 1430–1437.

[14] T. J. Farrell, M. S. Patterson, and B. Wilson. "A diffusion theory model of spatially resolved, steady-state diffuse reflectance for the noninvasive determination of tissue optical properties invivo." In: *Medical Physics* 19.4 (1992), pp. 879–888.

[15] A. Kienle, F. Foschum, and A. Hohmann. "Light propagation in structural anisotropic media in the steady-state and time domains." In: *Physics in Medicine and Biology* 58.17 (2013), p. 6205.

[16] F. Zeighami and M. A. Tehran. "Developing optically efficient nanofiber coatings inspired by Cyphochilus white beetle". In: *Journal of Industrial Textiles* 46.2 (2015), pp. 495–509.

[17] J. Yip, S.-P. Ng, and K. H. Wong. "Brilliant whiteness surfaces from electrospun nanofiber webs." In: *Textile Research Journal* 79.9 (2009), pp. 771–779.

[18] J. Huang et al. “Harnessing structural darkness in the visible and infrared wavelengths for a new source of light.” In: *Nature Nanotechnology* 11 (2016), pp. 60–66.

[19] Z. Fang et al. “Novel nanostructured paper with ultrahigh transparency and ultrahigh haze for solar cells.” In: *Nano Letters* 14.2 (2014), pp. 765–773.

[20] M. Nogi, A. N. N. S. Iwamoto, and H. Yano. “Optically transparent nanofiber paper.” In: *Advanced Materials* 21.16 (2009), pp. 1595–1598.

[21] V. Kumar et al. “Comparison of nano and microfibricated cellulose films.” In: *Cellulose* 21.5 (2014), pp. 3443–3456.

CHAPTER 5

Modeling the network anisotropy

The scale of the white beetle Chyphochilus is a unique example of high brightness-low weight optimization in a low-refractive index and low thickness photonic structure. The light propagating inside this system undergoes to multiple scattering and the particular geometry of the scattering system confers to the beetle a bright-white appearance due to a extremely high reflectance (high brightness), almost constant in all the visible spectrum (high whiteness). It has been shown that the scattering properties of the scale are directional dependent, i.e. anisotropic transport occurs. This is a direct consequence and fingerprint of the structural anisotropy of the disordered network of chitin filaments which characterize the scales interior. The filaments appear compressed along the direction perpendicular to the scale, configuration that provide high scatterers density along the same direction, i.e. the one relevant to achieve high reflectance, avoiding spatial correlation. Moreover the network geometry, that prevents the filament to overlap, makes possible to reach an incredibly high filling fraction (0.61) without been affected by optical crowding, that would otherwise manifest in common high density media. All these structural features allow the system to reach an incredible high scattering strength with low thickness, still not emulated by high refractive index artificial materials engineered to maximize light scattering. In this chapter a study of the dependence of the reflectance by the degree of anisotropy in random networks is presented, modeling the beetle structure and designing a simple algorithm to generate beetle-like networks. The algorithm parameters allows full control on the structural properties claimed to play a role in the rare scattering behavior of the system, like filling fraction and degree of anisotropy. FDTD simulations have been performed in order to retrieve informations on the dependence of the reflectivity by the network properties, in order to open up new strategies to engineer high scattering materials.

5.1 Angular correlations for brighness optimization

From previous works on packing geometrical shapes, it is well known that anisotropic scatterers, like cylinders, can be packed with higher densities introducing a lower degree of spatial correlations [1, 2, 3, 4, 5, 6, 7, 8], with respect to isotropic shapes, like spheres. The lack of correlations in optical media ensures the absence of frequency dependent coherence effects, manifesting comparable scattering efficiency in all the spectrum. This is a clear feature of the *Cyphochilus* scale reflectance spectrum (Figure 3.10), which does not exhibit any important feature, remaining flat in a very broad range of wavelength covering the visible and part of the near infrared. Spatial correlations between scatterers indeed will result in phase relations for the scattered waves. High filling fraction of rods can be obtained only introducing a certain degree of angular correlations (i.e. overall anisotropy). A clarifying example is provided by the different densities of the different phases of liquid crystals, which increases as the alignment increases [9]. A structural anisotropy of the scattering system is responsible of anisotropic transport [10, 11, 12, 13]. In particular the intra-scale network of Cyphochilus beetle is compressed along the direction orthogonal to scale surface. This particular arrangement 'trades' the in-plane scattering strength in order to increase the out-of-plane scattering, which is responsible of the total amount of reflected light (i.e. the brightness). A quantitative analysis on how the light transport of a disordered anisotropic network behaves at different average scatterer orientation can represent a further step in the study of the link between structural properties and photonic effets and a precious knowledge to fabricate novel and efficient scattering materials. In fact, modeling the beetle chitin network allows to define general network systems with tunable structural features. Informations on the impact of different filling fraction and size values on the chitin network have been provided by Wilts et al.[14], that performed light transport simulation on a cube-shape part of the chitin network ($7\times7\times7$ μm^3) numerically reconstructed from tomography acquisitions (Figure 5.1). The authors compared the reflectance of the network cube simulating white light incident along the direction of compression of the scale filament and along the plane of the scale (Figure 5.1b). Their results are in agreement with the experimental work shown in 4.3.1, where light transport measurement revealed the presence of anisotropic light transport. Further study have been done modifying the filling fraction of the imaged system, reported to be $45 \pm 6\%$, increasing and decreasing the average radius of the filaments, simulating light impinging in the direction perpendicular to the scale. As it is reported in Figure 5.1d, the author obtained an increase of the scattering strength for increasing filling fraction till volume fraction of the 40-50 % and then a slight decrease. The gray dots, indicating the reflectance spectrum of the scale, lay in this interval, indicating that the structure morphology allows an increasing of the brightness till filling fraction values around 50-60 %. Above these percentage values there is not a consistent reflectance increase and optical crowding effect affect the transport. This is a result that corroborates the hypothesis that the single scatterer anisotropy and the type of network architecture display no correlation effect, making possible high density packing together with high scattering strength, not normally achievable without anisotropy. A different type of analysis has been done, Figure 5.1c, stretching the system along the direction perpendicular to the scale. In this way the author obtained network systems with different thickness, filament radius and average filament orientation. Compressing

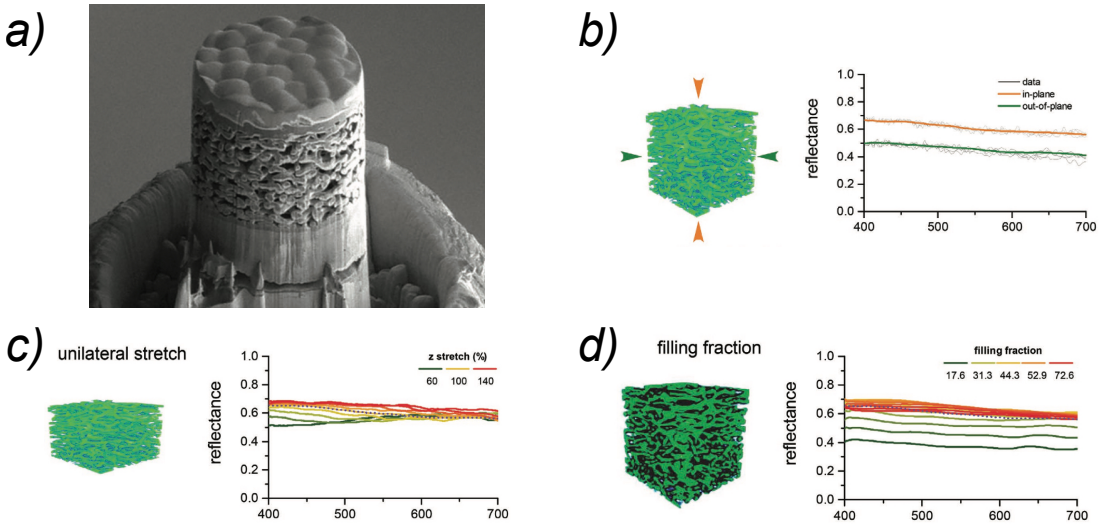

Fig. 5.1: *a*) SEM image of a scale part taylored with focus ion binning from the hole network. X-ray nanotomography has then been performed to obtain a 3D image of the chitin random network of 7×7×7 μm^3 volume. All images are taken from [14].

or stretching the structure leads the filament to be either more or less oriented along the scale plane, i.e. there is a change in the degree of anisotropy. They observed that compressing the structure lead to a decrease of the reflectance, especially at low wavelength, of more than 10 %. Stretching it to 140 % of the original thickness does not lead to any increase at low wavelength but to a ∼10 % higher brightness at high visible wavelength. The claim in the paper is that the thickness decrease is compensated by an increase in the anisotropy, that keeps the scattering strength quite high, while the stretching leads to a lower degree of anisotropy that, despite the higher thickness, lead to a loss of the scattering strength. Despite the results of the simulation, indicating that the different filament orientation might strongly affect the system brightness, the brightness changes in the study cannot be attribute to the anisotropy only, as many other structural parameters are changing, i.e. It is not possible by this analysis to distinguish the individual contribute to the brightness enhancement of parameters, like the degree of anistropy. Moreover, modifying the filament diameters decreases the whiteness making the variation of brightness extremely different in different spectrum regions. Thus the role and the real dependence of a beetle-like network reflectance by the amount of compression of the chitin scatterers in the scale plane is still an open topic.

5.2 Modeling the beetle scale: networks generation

In order to emulate the structure of the *Chyphochilus* network, the filaments have been approximated to rod-shaped scatterers (cylinders), that, to reproduce the flat response of the scale, require to be arranged in a disorder fashion without correlations. Moreover the network geometry needs to be taken into account in the modeling. All these features have been considered in the design of the algorithm, chosing to simulate a random-walk-like

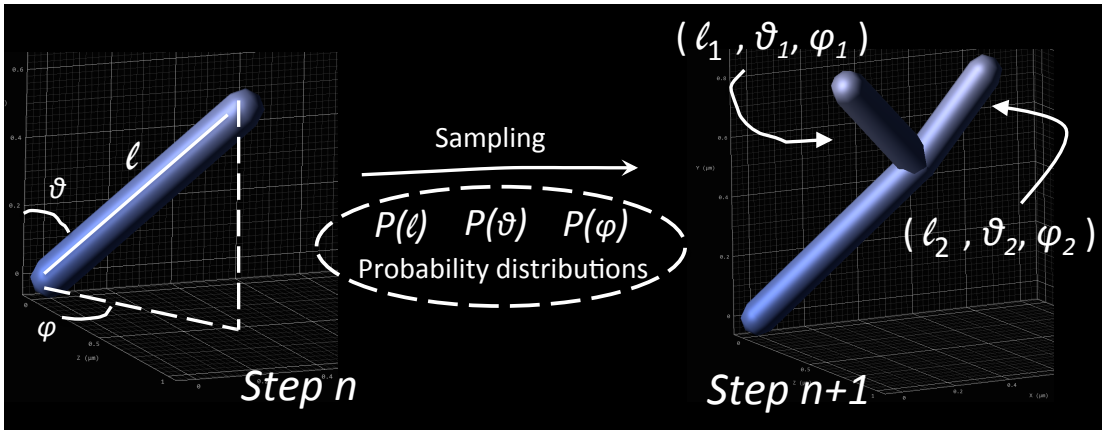

Fig. 5.2: Branching Random Walk: in each step two new scattering elements are added to the network. Direction and length are expressed in spherical coordinates. The radius of the rods is approximatly the average radius of the beetle filaments.

growth of the filaments in order to ensure the lack of correlations in the structure and satisfy the morphological condition to have juctions between the cylinders at their endpoints.

5.2.1 Random-walk algorithm for network structures

The single scatterer has been modeled as a rod of lenght l with space orientation described by a polar angle θ with respect to the z-axis, and an azimuthal angle φ in the xy-plane. The reference frame chosen to express the rod position in space is the same described in figure 4.1, where the z-axis represents the direction orthogonal to the scale surface, that lays in the xy-plane. In a single algorithm step, two new rods are attached to the endpoint of each rod of the previous step (Figure 5.2). The length and the orientation of the new rods are sampled according to a chosen probability distribution, describing a random walk grow of the filaments. The first step of the algorithm starts sampling a single point inside a volume, selected at the beginning of the algorithm. Periodic boundary conditions are applied along every direction. From this first point a sequence of step is performed where new rods appear as a bifurcation of those of the previous steps, as it is schematically depicted in Figure 5.3. The grow of the whole network stops when a chosed value of the filling fraction is reached. There is only one stop condition to the grow of a single filament. If the endpoint of the rod generated at step n is closer to the endpoint of another rod then a distance equal or lower than the diameter of the rod, no new rod is attached to this endpoint (Fig. 5.4). This condition prevents different filaments to grow too close to each other, avoiding the formation of clusters. This condition reduces the heterogeneity of the whole system and limits the generation of new rods in area with high density, that would result in optical crowding at lower filling fraction than the one of the beetle scale.

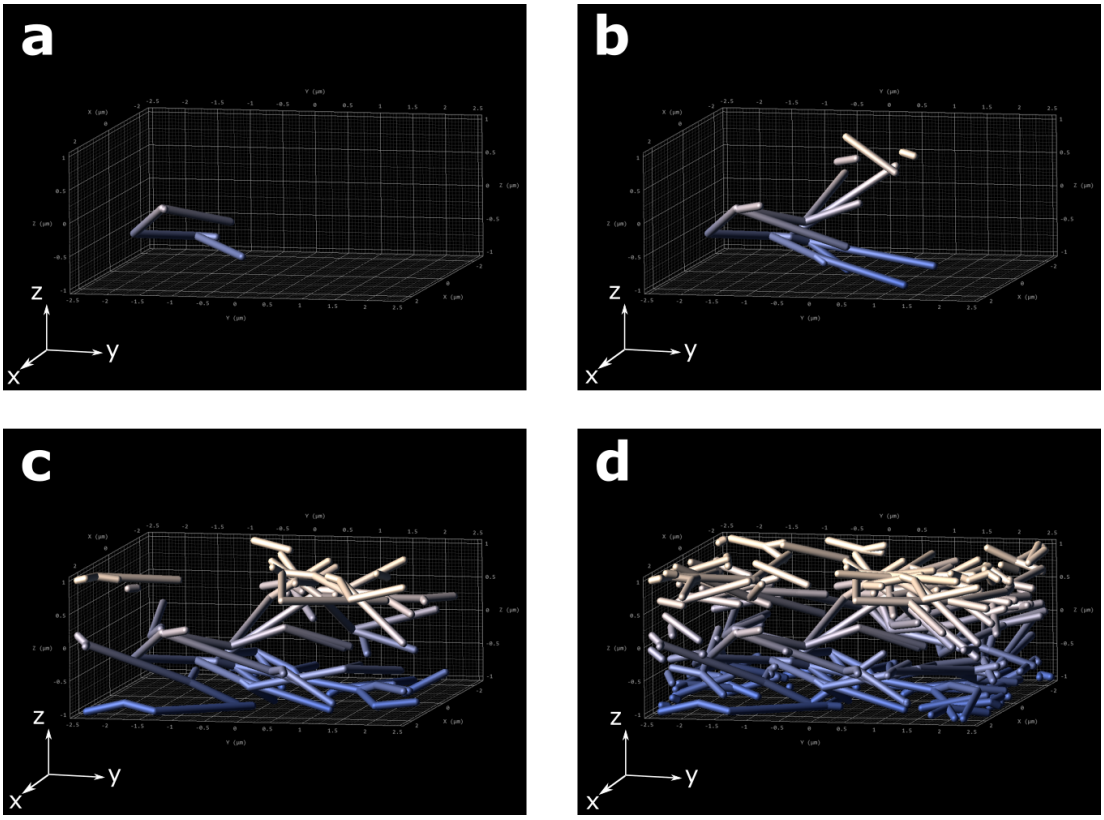

Fig. 5.3: Representation of different steps of a single branching random walk realization with $\sigma_\theta = 0.3$. *a*) Configuration after two steps. *b*)-*c*)*d*) Configurations at higher number steps, where the periodic boundary condition are applied.

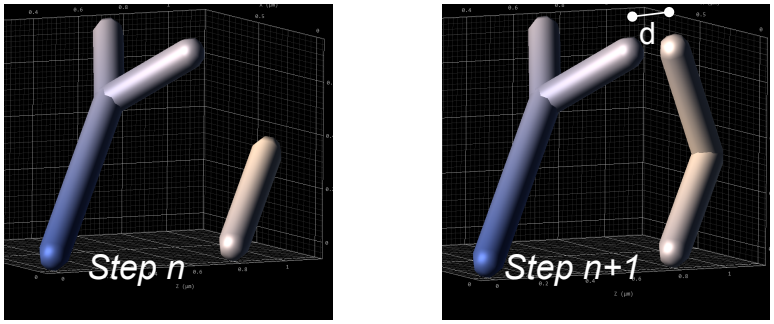

Fig. 5.4: Stop condition: in the step *n+1* a new rod is generated. Its endpoint is at a distance d from the endpoint of another rod equal to the rods diameter value. The stop condition is satisfied and in step *n+2* no rods will be attached to this rod.

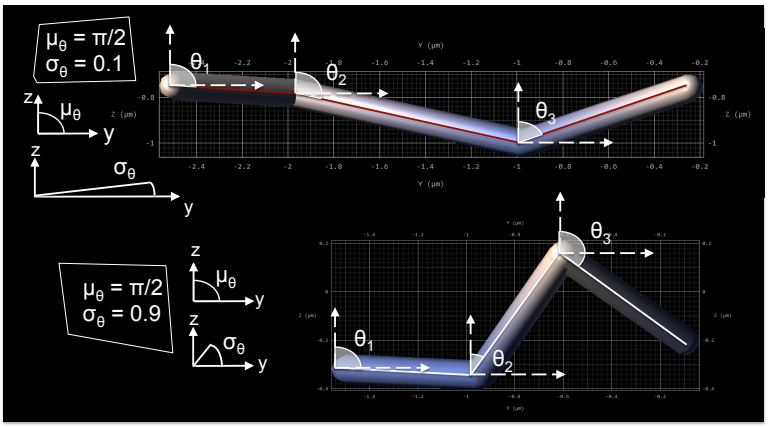

Fig. 5.5: Examples of rods generation. The first filament is the output of three sampling steps with θ normally distributed with $\mu_\theta = \pi/2$ and $\sigma_\theta = 0.1$ (approximatly 5.7°). The second one has been generated with the same structural parameters and a larger standard deviation $\sigma_\theta = 0.9$, corresponding to 51.7°. For the sake of clarity in each step only a single rod is attached to the previous step rod.

Algorithm parameters

A proper choice of the algorithm parameters is required to reproduce the key feature of the real chitin netowrk. The diameter of the rods section have been chosen equal for each rod, and it is set to $d = 250$ nm [15, 16]. As the direction of each rod is sampled according to a probability distribution it is possible to tune the degree of anisotropy of the network choosing the proper distributions for l, θ and ε and selecting specific values of their parameters. Moreover the thickness, that becomes fixed once the size of the growth volume is set, and the filling fraction, represent two other important parameters useful to emulate the chitin network behavior and to perform the study subject in this chapter. The length l of each rod is picked from a truncated normal distribution, with mean value $\bar{l} = 1$ µm and standard deviation $\sigma_l = 0.7$ µm. The distribution has been limited to the interval $[0,2\bar{l}]$, in order to avoid the generation of rods with length corresponding to the tails of the distribution. The average length, $\bar{l}$ = 1 µm, has been chosen slightly bigger than the actual length of the chitin rods. As it will be explained later, there are no constrains about rods intersection, unlike the intra-scale network where according to SEM image there is no rod overlap apart in the junctions. The crossing between different rods lead to a decrease of the effective length of the scatterer, reason that motivate a choice of $\bar{l}$. The rod azimuthal angle ε is sampled from a uniform distribution in the interval $[0,\pi]$. The distribution of the azimuthal angles sets the degree of anisotropy in the xy-plane, i.e. the one parallel to the scale surface. As we are interested on how the anisotropy affects the out-of-plane scattering and the results in the previous chapter (subsectioon 4.3.1) indicates close values of $l_{t,x}$ and $l_{t,y}$, the scatterers distribution in the model have been chosen isotropic for the xy-plane. This motivates the uniform distribution for the azimuthal angles. The polar angle θ is sampled from a normal distribution with mean value $\bar{\theta} = \pi/2$. This value imposes that the rods are in average aligned parallel to the x-y plane. The

standard deviation σ_θ of the polar angle distribution sets the degree of anisotropy of the system with respect to the z-axis, i.e. the degree of compression of the network along the direction perpendicular to the scale surface. The effect of this distribution on the rod generation in 3 consecutive steps (neglecting the branching in each step and considering only one of the two rods that are actually generated) is represented in Figure 5.5a, where the polar angles are picked from a normal distribution with $\theta^- = \pi/2$ and $\sigma_\theta = 0.2$ (~ 11.5 °), and 5.5b where the distribution has a larger standard deviation $\sigma_\theta = 0.9$ (~ 51.7 °), that lead to a more isotropic structure. Structures with different degree of anisotropy have been generated and studied. The stop conditions of the growth are set trough the last parameter described in this section, the filling fraction f, feature that strongly affects the scattering properties of a system [16, 17, 18, 19]. When a certain f is reached, the growth of the network stops. A similar analysis on the beetle filling fraction performed in [14] has been carried out in this work generating networks with the filling fraction of the *Cyphochilus* scales (f=0.6). Moreover also structures with different f have been generated and studied. Structures with different filling fraction differ from the total number of generated rods, while the rod section is kept fixed at d = 250 nm, together with the average rod length ($\bar{l} = 1$ µm).

Output structures

In Figure 5.6 two structures generated are presented. The standard deviations of the polar angle distribution are $\sigma_\theta = 0.1$ and $\sigma_\theta = 0.9$ and all the other algorithm parameters (cell size, filling fraction, mean values of the probability distribution, rods diameter) are the same for both the structures. Both the rendering and the cross sections show clearly how the structures exhibit different degree of anisotropy and how it can thus be fully controlled. To qualitatively evaluate the similarity of the generated network with the beetle SEM and TEM images are reported in (Fig. 5.7a and 5.7b) respectively. The TEM image represent a tomography along the plane xy of the scale interior, while the SEM image highlights the morphology of the network. Comparing them with the cross cut along the xy plane direction and the rendering of the simulated structures reported in 5.6, we can conclude that the generated rods orientation and distribution are comparable with the scale ones. Anyway, as mentioned before, the algorithm network presents differences from the beetle structure. The latter, as it can be observed in SEM images, exhibits a network morphology characterized by homogeneously distributed junctions connected by non intercepting rods (Fig. 5.7b). Furthermore the beetle filaments seem to avoid the formation of high density regions tending to grow along trajectories where no other rods are present. In the developed algorithm no constraints about interception are imposed and the rods are free to grow independently from the surrounding environment, apart for the stop condition (Figure 5.4). This feature could increase the optical crowding effect, as we will see in the next section.

5.3 FDTD calculations and results

The optical response structures generated by the algorithm have been investigated through the Finite Difference Time Domain method (FDTD) [20, 21], consisting in retrieving the field evolution in discrete time steps, solving numerically Maxwell equations.

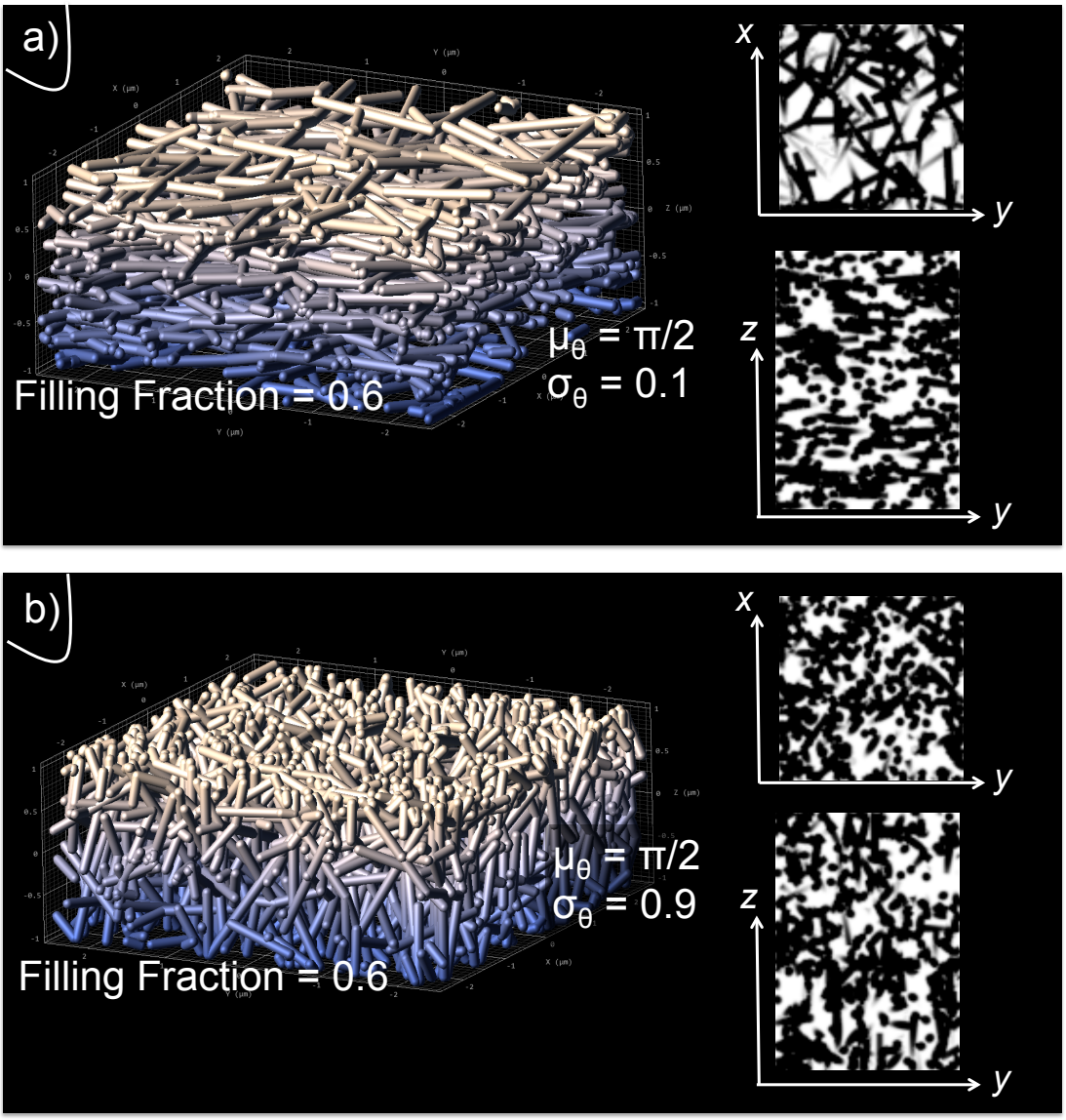

Fig. 5.6: Output structures of the Random Branching Algorithm are displayed. For each structure a rendering is displayed on the left, and two cross sections that describe the internal distribution of the index of refraction are shown on the right. The two cross sections correspond to internal planes tangent to the center of the structure and respectively parallel to xy and yz.

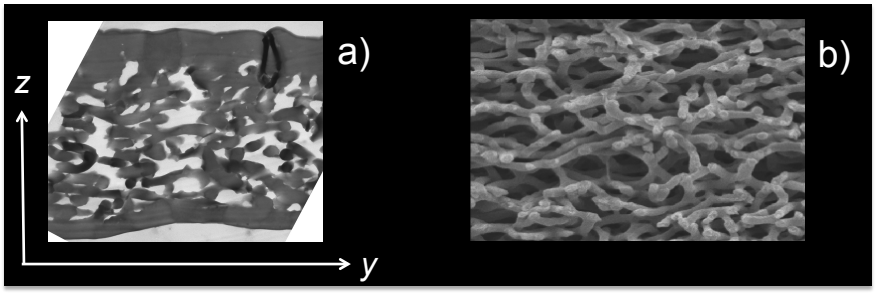

Fig. 5.7: a) TEM image of the internal structure of the white beetle scale. The image correspond to the rod distribution in a plane parallel to the z direction. b) SEM image that highlights the network morphology of the scale internal structure.

Structures with different degree of anisotropy and different filling fraction have been generated through the algorithm and their reflectance spectrum has been computed with the FDTD dedicated open source software MEEP [22]. We therefore obtained a detailed study of the dependence of the brightness by the network parameters that allowed to perform a comparison with the *Chyphochilus* experimental data.

Computational cell and simulation parameters

The structures investigated are all cubic volumes with size 7 μm and varying values of filling fraction and degree of anisotropy. The filling fraction has been set in the range from 0.1 to 0.7 while the degree of anisotropy, that as mention before is tuned through the standard deviation of the rods polar angle distribution σ_θ, has been set to 0.2, 0.5, 0.9 and 1.2 radiant (in degrees $\sigma_\theta = 11,5°$, $28,6°$, $51,6°$, $68,7°$). Together with anisotropic systems, the transport in isotropic networks (iso) have been simulated as well, sampling the rods polar angle not from a normal distribution but from a uniform distribution in the interval $[0, \pi]$. For all the couples (ff, σ_θ) ten structures have been generated and a mean value of the total reflectance has been computed to average out the disorder effects.
All the calculations performed are 3D. A representation of the computational cell is reported in Figure 5.8. The coordinates of the rod network are given as input to MEEP that reproduces the structure in between two plane detectors perpendicular to the z direction. The plane source in the calculation is also perpendicular to z and it emits a gaussian pulse with central normalized frequency $\nu_{cen} = 1.67$ and width $d\nu = 1$.[1] The size of the cell along the direction x and y is the same of the input network and, along these directions, periodic boundary condition are applied. The size of the cell along z has been set in order to place the detectors enough far from the sample to avoid near field effects. For this purpose value d has been defined as $d = 3\lambda_{max}$ where $\lambda_{max} = \lambda_{cen} + d\lambda$ (near field effects are considered negligible at a distance from the source equal to three times the wavelength). This value has been assigned respectively to the distance between the source and the reflectance detector, the reflectance detector

[1] The values are expressed in the adimensional MEEP units. The central wavelength of the pulse is $\lambda_{cen} = 0.6$, which in our simulations corresponds in SI units to $\lambda = 0.6\,\mu m$.

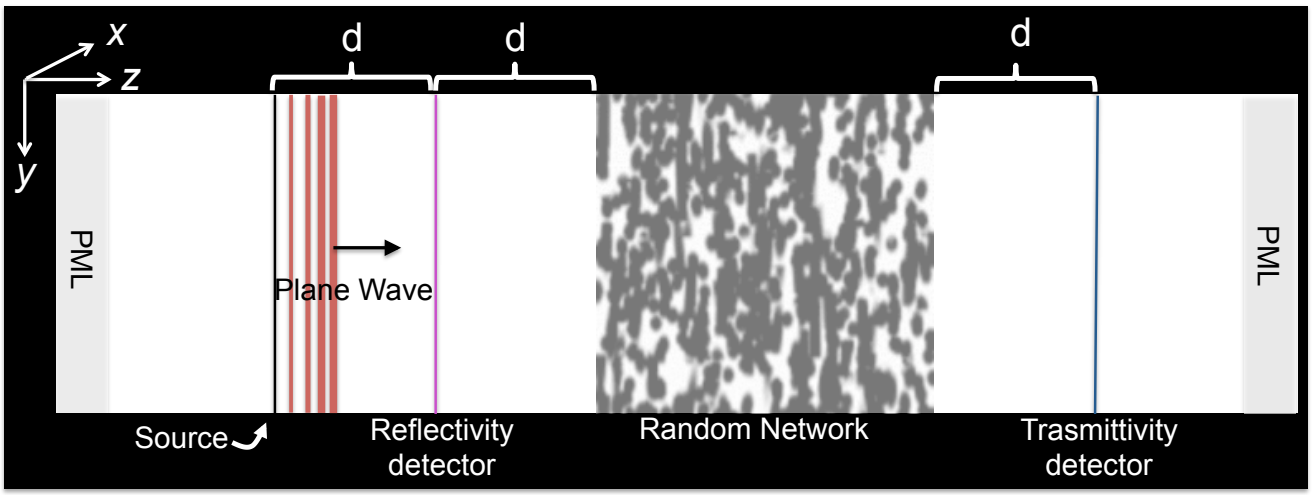

Fig. 5.8: Rappresentation of the computational cell in the plane zy.

and the random network, the random network and the trasmittance detector (Fig. 5.8). PML blocks of width $d_{pml} = 1$ have been positioned at the end of the cell along z. As a consequence the computational cell has size $7 \times 7 \times 21{,}85$ µm^3.
Simulations were executed with resolution 25 for 310 time periods, 10 time periods for source excitation and 300 periods with source off. Each spectrum has been computed for $n_{freq} = 300$ number of frequency equally spaced inside the interval $[\nu_{cen} - d\nu, \nu_{cen} + d\nu]$.

5.3.1 Results: anisotropy brigthness dependance

The reflectance spectra for different degree of anisotropy are shown in this section for $f = 0.6$ only, the value corresponding to the beetle scale reported in literature. The result are reported in Figure 5.9. An analogous behavior have been found for all the other filling fractions investigated. The blue line corresponds to an isotropic system, the green line to an arrangement of the rods with a normal distributed polar angle with $\sigma_\theta = 0.9$ (51.6°), and the red line have been generated with $\sigma_\theta = 0.2$ (11.5°). All the displayed spectra exhibit a flat response in the analyzed spectrum region, characteristic that proves the absence of correlation that would otherwise manifest in pronounced spectral features. Moreover they indicate that the random network brightness exhibit a dependence from the degree of anisotropy. Structures with the same value of f present reflectance that tends to increase with increasing degree of anisotropy. An important conclusion can be drew by this results. The compared structures present the same structural features, i.e. same volume and same amount of material, except for the degree of anisotropy. This means that a brightness increase is not only obtained by exploiting the scatterer asimmetry to reach higher scatterers density in a fixed volume but it is something that can be optimized tailoring exclusively the in-plane orientation of the rods.This result confirms the previous experimental interpretation on the bright white appearance in the beetle scale as optimized through anisotropy but at the same time it denotes that the lower scattering mean free path along the perpendicular direction is not the result of higher density along this axis but a merely topological effect.

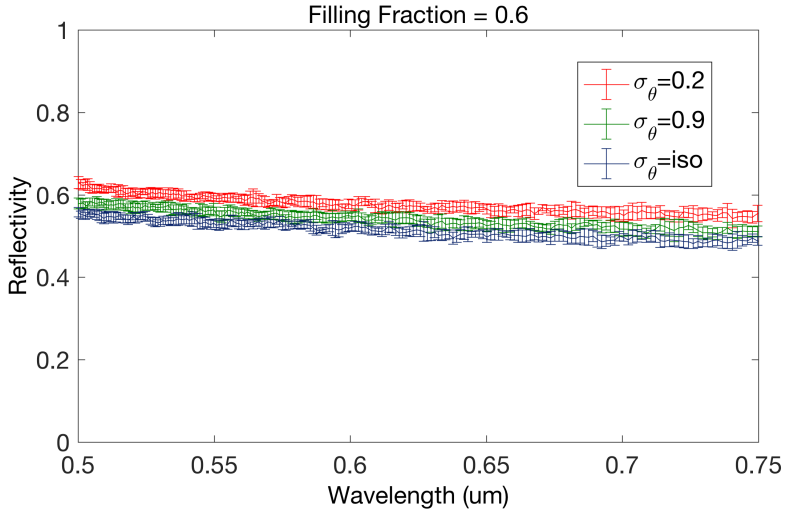

Fig. 5.9: Reflectance spectra of the random network generated through the Random branching algorithm with $f = 0.6$. The spectral corresponding to the values $\sigma_\theta = 0.5, 1.2$ have been omitted for the sake of clarity as, even following the trend, they overlap the spectra corresponding the close values of σ_θ. The error bars are the standard deviations of the average of the reflectance calculated for ten different structures with the same parameters.

5.3.2 Results: filling fraction brigthness dependance

In this section an analysis of the simulation output for structures with varying filling fraction is reported. The degree of anisotropy is here fixed to the value σ_θ=0.2 $(11, 5°)$. The choice of this value must be found in the similarity of the network so obtained with the beetle one, and, as displayed in Figure 5.9a, the one that guaranties one of the highest scattering strength. Anyway analogous results have been found also for all the other σ_θ analyzed. The comparison is shown in Figure 5.10. It is evident how, except for the lowest investigated value f=0.1, all the computed spectra exhibit a flat response in the wavelength interval analyzed, reproducing, especially at high wavelength, the whiteness of the beetle scale. The higher reflectance at low wavelengths for f=0.1 can be understood considering that at higher scatterers density, optical crowding effect leads to a decrease of the scattering strength in the all spectral range, while at lower densities high frequencies are more affected. It's possible to observe that the higher values of brightness correspond to low f. Starting from $f = 0.7$ and moving to lower values, the reflactance tends to increase till it reaches the same values within the error bars from $f = 0.5$ till $f = 0.3$, interval corresponding to the maximum brightness. Other useful quantitative information for the comparison can be retrieved from Figure **??**b that show the comparison between the total reflection of all the structures investigated, for a fixed wavelength ($\lambda = 550$nm) and same degree of anisotropy ($\sigma_{theta} = 0.2$). Again, moving from low to high filling fractions, the total amount of light reflected increases until it reaches a maximum (R ~ 0.65) for approximately $f \sim 0.3 \div 0.4$. Then it decreases. The reflectance in the maximum results $\sim 25\%$ higher than the reflection of the $f = 0.1$ structure and $\sim 18\%$ higher of the $f = 0.7$ structure. This trend can be interpreted

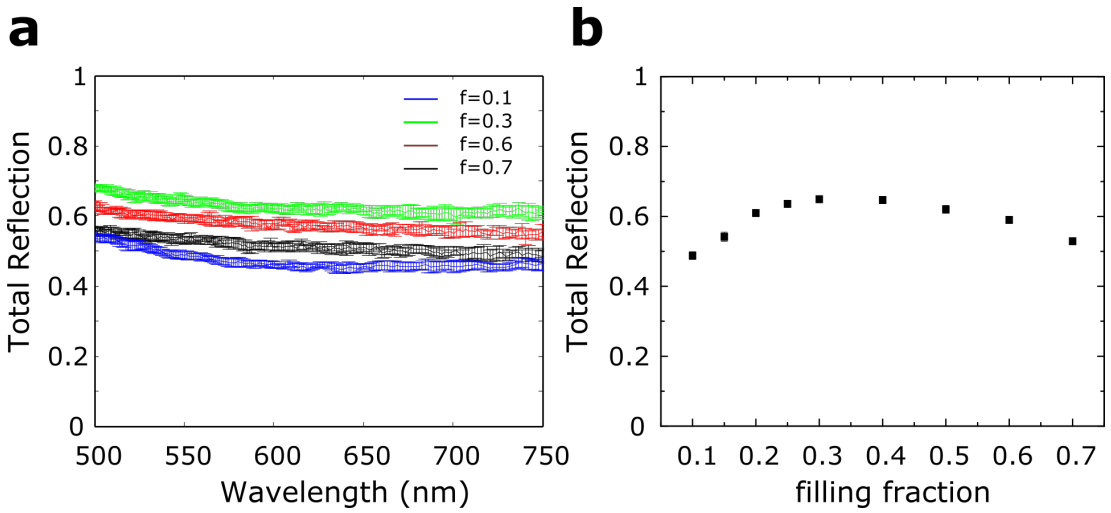

Fig. 5.10: Total reflection for structures with fixed anisotropy and varying filling fraction. a) Spectra related to four structures with $\sigma_\theta = 0.2$ and different filling fraction, f = 0.1 (blue line), f = 0.3 (green), f = 0.6 (red) and f = 0.7 (black). (b) Total reflection for a fixed wavelength ($\lambda = 550$ nm), fixed anisotropy $\sigma_\theta = 0.2$, and varying filling fraction. The data plotted are the average value of the reflection computed from 10 different structures with the same parameters. The error bars are given by the standard deviation.

considering again the optical crowding effect. Indeed, increasing the concentration of scatterers the overall scattering strength does not increase linearly and, after $f = 0.4$ is even reduced. Notably the filling fraction of Cyphochilus scales does not guarantee the highest value of reflectance. This can be directly linked with the morphological differences between the modeled network and the actual chitin one. These particular behavior can be interpreted as a propriety strictly connected to the morphology of the generated network. As no constraints about rods interception have been imposed, the rods are free to compenetrate and they can grow really close to each other, feature that is not present in the TEM and SEM images of the real beetle network, where the rods in between the junctions tend to be more far apart. As a consequence optical crowding show up in the networks at lower f than the beetle one. Anyway we can also consider that the filling fraction of the actual beetle scales could not represent the optimal value for the reflectance, but it is a trade-off which consider other important parameters, like for example the mechanical stability of the structure. This last hypothesis is corroborated by the simulations performed in [14] and gathered in Figure 5.1. The maximum brightness found by the authors, correspond to $f \sim 0.5$, very close to the values that gives maximum scattering strength in the networks designed in this chapter.

5.3.3 Results: in-plane and out-of-plane propagation

Finally we present a comparison between the reflectance spectra of the same structure but for two different orientations. One, like in the previous simulations, with light incident along the anisotropic direction and the other with the network rotated of π / 2 around

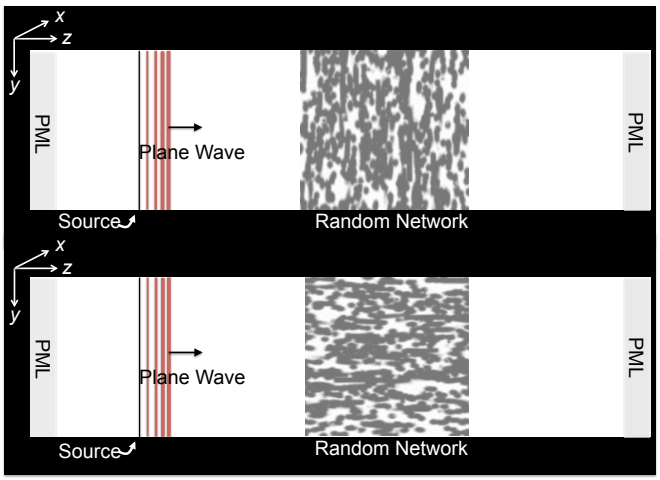

Fig. 5.11: Scheme of the FDTD simulation for two different orientations of the network. In the first one the plane wave propagates along the direction of compression of the filaments. In the second one the same structure is rotated of π / 2 around the x axis and information about the transport ain the isotropic plane can be retrieved.

the x axis, so to analyze also the case when light impinges in a direction perpendicular to the anisotropic axis (Fig. 5.11). The network parameters are chosen in order to perform the simulation on structures with anisotropy and f comparable with the white beetle ones, that is $f = 0.6$ and $\sigma_{theta} = 0.2$. Again the spectra are the results of the average of the reflectance for FDTD on 10 networks. As it was expected the computed brightness is higher in the case of light incident along the direction of compression of the filaments (Fig. 5.12). From these results we can estimate quantitatively the transport mean free path along the anisotropic direction $l_{t,\perp}$ and the one in the isotropic plane $l_{t,\parallel}$ and compare the obtained values with the transport mean free path of the beetle scale measured in Chapter 4 and reported also in [23]. As the experiment in this reference has been performed with monochromatic light with $\lambda = 550$ µm, we consider the values of the reflectance spectra for that specific wavelength.
The transport mean free path can be computed from the total trasmission using the Ohm's law for slab geometry system.

$$T = \frac{l_t + z_e}{L + 2z_e} \tag{5.1}$$

with L thickness and z_e extrapolation length. It is so possible to obtain $l_{t,\perp}$ and $l_{\parallel}$ inserting the values $T_\perp$ and $T_\parallel$ computed in the simulations with different network orientations. We thus get $l_{t,\perp} = 2,22 \pm 0,04\,\mu m$ and $l_{t,\parallel} = 2,89 \pm 0.06\,\mu m$ that correspond to the ratio $l_{t,\parallel}/l_{t,\perp} = 1,30 \pm 0.06$. This value is lower compared to the ratio measured in chapter 4 for the same wavelength, that is higher then 2. Again the lower value of the scattering strength could interpreted as due to the absence of constrain in the algorithm on rods interception, with a consequent tendency to generate regions with clusters of material, which result in a reduction of the effective anisotropy of the system.

To conclude, a detailed analysis of the structural anisotropy in the random network of

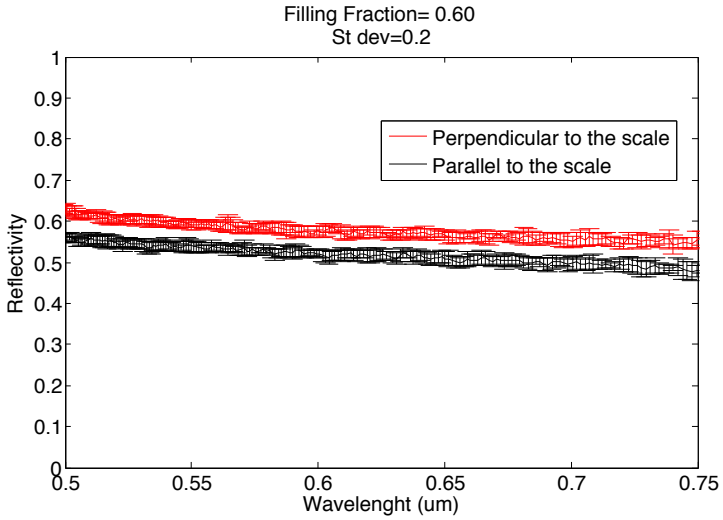

Fig. 5.12: Reflectance spectra for structures with $\sigma_\theta = 0.2$ and $f = 0.6$ and different orientation inside the computational cell. The red one corresponds to light incident along the direction of compression of the filaments (perpendicular to the scale) and the black one corresponds to light incident in the plane parallel to the scale surface.

the *Chyphochilus* scale has been performed. From the experimental results in chapter 4, proving that anisotropic light transport occurs inside the scale, a modeling of the system morphology has been done to attempt both to replicate the system scattering properties and to perform a study of the impact of the degree of anisotropy in disorder network in general. It has been shown how, with a random walk based simple algorithm, it is possible to obtain simulated network displaying brightness and whiteness comparable to the beetle one. Moreover, from light transport calculations on the network with tunable structural parameters, a clear dependence of the reflectivity by the scattering properties has been established, demonstrating how the degree of anisotropy, independently from the system filling fraction and the filament packing, produces an increase of the out-of-plane scattering strength.

References

[1] K. E. Evans and A. G. Gibson. "Prediction of the maximum packing fraction achievable in randomly oriented short-fibre composites." In: *Composites Science and Technology* 25.2 (1986), pp. 149–162.

[2] S. R. Williams and A. P. Philipse. "Random packings of spheres and spherocylinders simulated by mechanical contraction." In: *Physical Review E* 67.5 (2003), p. 051301.

[3] P. Bolhuis and D. Frenkel. "Tracing the phase boundaries of hard spherocylinders." In: *Journal of Chemical Physics* 106.2 (1997), pp. 666–687.

[4] S. Li et al. "Maximum packing densities of basic 3D objects." In: *Chinese Science Bulletin* 55.2 (2010), pp. 114–119.

[5] A. P. Philipse and A. M. Wierenga. "On the density and structure formation in gels and clusters of colloidal rods and fibers." In: *Langmuir* 14.1 (1998), pp. 49–54.

[6] S. Torquato and F. H. Stillinger. "Jammed hard-particle packings: From Kepler to Bernal and beyond." In: *Reviews of Modern Physics* 82.3 (2010), p. 2633.

[7] T. Schilling and D. Frenkel. "Self-poisoning of crystal nuclei in hard-rod liquids". In: *Journal of Physics: Condensed Matter* 16.19 (2004), S2029.

[8] A. Wouterse, S. Luding, and A. P. Philipse. "On contact numbers in random rod packings." In: *Granular Matter* 11.3 (2009), pp. 169–177.

[9] D. Liu and D. J. Broer. "Liquid crystal polymer networks: switchable surface topographies." In: *Liquid Crystals Reviews* 1.1 (2013), pp. 20–28.

[10] M. H. Kao et al. "Observation of light diffusion and correlation transport in nematic liquid crystals." In: *Physical Review Letter* 77.11 (1996), p. 2233.

[11] A. Kienle et al. "Light propagation in dentin: influence of microstructure on anisotropy." In: *Physics in Medicine and Biology* 48.2 (2003), N7.

[12] P. M. Johnson, S. Faez, and A. Lagendijk. "Full characterization of anisotropic diffuse light." In: *Optics Express* 16.10 (2008), pp. 7435–7446.

[13] D. S. Wiersma et al. "Time-resolved anisotropic multiple light scattering in nematic liquid crystals." In: *Physical Review Letters* 83.21 (1999), p. 4321.

[14] B. D. Wilts et al. "Evolutionary-Optimized Photonic Network Structure in White Beetle Wing Scales". In: *Advanced Optical Materials* 3 (2015), pp. 1337–1341.

[15] P. Vukusic, B. Hallam, and J. Noyes. "Brilliant whiteness in ultrathin beetle scales." In: *Science* 315.21 (2007), pp. 348–348.

[16] S. M. Luke, B. T. Hallam, and P. Vukusic. "Structural optimization for broadband scattering in several ultra-thin white beetle scales." In: *Applied Optics* 49.22 (2010), pp. 4246–4254.

[17] S. Fraden and G. Maret. "Multiple light scattering from concentrated, interacting suspensions." In: *Physical Review Letters* 65.4 (1990), p. 512.

[18] B. L. Drolen and C. L. Tien. "Independent and dependent scattering in packed-sphere systems." In: *Journal of Thermophysics and Heat Transfer* 1.1 (1987), pp. 63–68.

[19] G. M. Conley et al. “Light transport and localization in two-dimensional correlated disorder.” In: *Physical Review Letters* 112.14 (2014), p. 143901.

[20] A. Taflove. *Computational Electrodynamics: The Finite-Difference Time-Domain Method, Third Edition*. 2005.

[21] A. Taflove. “Application of the finite-difference time-domain method to sinusoidal steady-state electromagnetic-penetration problems.” In: *Electromagnetic Compatibility, IEEE Transactions on* 3 (1980), pp. 191–202.

[22] A. F. Oskooi et al. “MEEP: A flexible free-software package for electromagnetic simulations by the FDTD method”. In: *Computer Physics Communications* 181.3 (2010), pp. 687–702.

[23] L. Cortese et al. “Anisotropic Light Transport in White Beetle Scales”. In: *Advanced Optical Materials* 3 (2015), pp. 1337–1341.

CHAPTER 6

Conclusions

In this work we investigated light matter interaction in two systems presenting extremely peculiar structural properties, that strongly affect light propagation mechanism. Despite these systems belong to different classes of disordered optical media, the transport features that make them unique are, in both cases, due to the presence of spatial correlations in their scattering elements arrangement.
The first system under study is an open 2D fractal distribution of point-like strongly resonant scatterers with resonance frequency ω_0 and width Γ_0. The supported resonances have been studied analytically exploiting the Coupled Dipole method, that allows to model the scatterer distribution as an ensemble of electric dipoles whose optical response for an incident electric field can be then computed from Maxwell equations. In this formalism the solutions of Maxwell equations are the eigenvectors of the Green matrix and they represent the modes of the system with frequencies given by the associated eigenvalues. In the case of open media the natural resonances, called Quasinormal-modes (QNM), are affected by leakages and the Green matrix eigenvalues are complex values representing frequency and width of the corresponding resonances. Assuming a polarization of both the medium and the exciting field along the direction perpendicular to the dipoles plane, i.e. solving the scalar problem, the QNM have been computed. A statistical analysis of the degree of localization of the system resonances has been performed computing the QNM Inverse participation ratio (IPR) which inverse quantity, the Mode Spatial Extent, represents the number of scattering centers in the region occupied by the QNM electric field. This is a common analysis that has so far been exploited to characterize the resonances of deterministic aperiodic structures or homogeneous disordered systems, but has not been adopted to fully characterize the QNM of a general 2D fractal system. Extending the computation of the IPR in all space and not only to the dipoles coordinates, a detailed analysis on the mode size revealed an unexpected feature: the fractal system exhibits a coexistence of modes with all possible sizes. A comparison with the resonances (localized and delocalized modes) of homogeneous disordered and

heterogeneous disordered systems have been performed, observing that a configuration where modes sizes coexist can be find only for the fractal type. This results confirms how the self-similarity in fractal systems can generate exotic optical properties that go beyond those of merely heterogeneous scatterers distributions, introducing QNM size coexistence, feature that has not been reported so far for any other type of disordered system with no self-similarity.
The second system investigated is the scale of the white beetle *Chyphochilus*. The scale, only few micrometers thick, presents in its interior an anisotropic random network of chitin filaments, compressed along the direction perpendicular to the scale. The striking features of the network are the very high brightness and whiteness, reached despite the low value of the refractive index and the low scale thickness. Combining experimental measurements and numerical modeling of the structural properties we unveiled the mechanism behind the scattering strength optimization: the anisotropy. Imaging experiments allowed to determine the 2D intensity spatial profile of the light transmitted through the scale and total transmission measurements have been exploited to retrieve information on the scattering properties along the direction perpendicular to the scale plane. According to the high density and the arrangement of the embedded scattering rods, data have been interpreted with diffusion theory, justified by previous observation of multiple light scattering inside the system. It has been observed that the transmission measurements are nicely described by anisotropic diffusion theory while they exhibit discrepancy from isotropic theory. This confirms that the compression of the filaments along the direction perpendicular to the scale (angular correlation) provides anisotropic light transport, enhancing the scattering strength in the perpendicular direction and thus the brightness. A numerical study has then been performed with the goal of modeling the chitin network and determining how structural features, as degree of anisotropy and filling fraction, can affect the reflectivity of a beetle-like network. For this purpose a Monte Carlo based algorithm simulating a random growth of rods has been designed to generate numerical networks with tunable structural parameters. FDTD simulations have afterward been performed to calculate the reflectivity. The computed spectra prove that the algorithm is suitable to qualitatively model the brightness and the whiteness of the beetle. Moreover they showed that conserving the single scatterer shape, the system size and the density of the network an increase of the degree of anisotropy is followed by an increase of the reflectance. It indicates how the optimization through the anisotropy do not consist only in the higher degree of packing that can be reached aligning the rods, i.e. higher density, but it is also the overall rods orientation itself, with respect to the plane of the scale, that increases the system scattering strength. This knowledge, that is the considerable increase of the reflectance by an increase of the degree of anisotropy, can be applied to design and fabricate novel optical white materials for coatings with low thickness and high reflectivity.